Materials Science and Engineering R 72 (2011) 203–252

Contents lists available at ScienceDirect

Materials Science and Engineering R

journal homepage: www.elsevier.com/locate/mser

Nanostructured electrodes for lithium-ion and lithium-air batteries: the latest developments, challenges, and perspectives

Min-Kyu Song [a,1], Soojin Park [b,1], Faisal M. Alamgir [a], Jaephil Cho [b,*], Meilin Liu [a,**]

[a] School of Materials Science and Engineering, Center for Innovative Fuel Cell and Battery Technologies, Georgia Institute of Technology, 771 Ferst Drive, Atlanta, GA 30332-0245, USA
[b] Interdisciplinary School of Green Energy, Converging Research Center for Innovative Battery Technologies, Ulsan National Institute of Science & Technology (UNIST) 701-11,100 Banyeon-ri, Eonyang-eup, Ulju-gun, Ulsan 689-798, Republic of Korea

ARTICLE INFO

Article history:
Available online 20 July 2011

Keywords:
Nanostructured electrodes
Lithium-ion batteries
Lithium-air batteries
Metal-air batteries
Lithium batteries
In situ characterization

ABSTRACT

The urgency for clean and secure energy has stimulated a global resurgence in searching for advanced electrical energy storage systems. For now and the foreseeable future, batteries remain the most promising electrical energy storage systems for many applications, from portable electronics to emerging technologies such as electric vehicles and smart grids, by potentially offering significantly improved performance, energy efficiencies, reliability, and energy security while also permitting a drastic reduction in fuel consumption and emissions. The energy and power storage characteristics of batteries critically impact the commercial viability of these emerging technologies. For example, the realization of electric vehicles hinges on the availability of batteries with significantly improved energy and power density, durability, and reduced cost. Further, the design, performance, portability, and innovation of many portable electronics are limited severely by the size, power, and cycle life of the existing batteries. Creation of nanostructured electrode materials represents one of the most attractive strategies to dramatically enhance battery performance, including capacity, rate capability, cycling life, and safety. This review aims at providing the reader with an understanding of the critical scientific challenges facing the development of advanced batteries, various unique attributes of nanostructures or nano-architectures applicable to lithium-ion and lithium-air batteries, the latest developments in novel synthesis and fabrication procedures, the unique capabilities of some powerful, *in situ* characterization techniques vital to unraveling the mechanisms of charge and mass transport processes associated with battery performance, and the outlook for future-generation batteries that exploit nanoscale materials for significantly improved performance to meet the ever-increasing demands of emerging technologies.

Contents

1. Introduction . . . 204
2. Nanostructures to transcend challenges . . . 206
 2.1. Scientific and technical challenges facing the development of Li batteries . . . 206
  2.1.1. Challenges associated with Li-ion batteries . . . 206
  2.1.2. Challenges associated with Li-air batteries . . . 206
 2.2. Unique attributes of nanostructures and nano-architectures . . . 207
  2.2.1. Why do nanomaterials behave differently? . . . 207
  2.2.2. Unique advantages of nanostructured electrodes for Li batteries . . . 207
  2.2.3. Disadvantages of nanostructured electrodes . . . 209
  2.2.4. Novel strategy: bio-inspired nanostructures . . . 209
3. Anode materials for Li-ion batteries . . . 210
 3.1. Classification of anode materials . . . 210
  3.1.1. Lithium metal and carbonaceous materials . . . 210
  3.1.2. Lithium alloying compounds and intermetallic alloys . . . 210

* Corresponding author. Tel.: +82 52 217 2910; fax: +82 52 217 2968.
** Corresponding author. Tel.: +1 404 894 6114; fax: +1 404 894 9140.
E-mail addresses: jpcho@unist.ac.kr (J. Cho), meilin.liu@gatech.edu (M. Liu).
[1] These authors contributed equally.

0927-796X/$ – see front matter © 2011 Elsevier B.V. All rights reserved.
doi:10.1016/j.mser.2011.06.001

3.1.3. Transition metal compounds. . . . 211
3.2. Specific examples of recent developments 211
3.2.1. Nanostructured anode materials. . . . 211
3.2.2. Nanocomposites of anode materials 213
3.2.3. Surface modification of anode materials 215
3.2.4. Nano-architectured anode electrodes 217
3.3. Summary 218
3.4. Remaining challenges 219
3.5. Opportunities and new directions 219
4. Insertion compounds as cathodes for Li-ion batteries 219
4.1. Classification of cathode materials. . . . 219
4.1.1. Transition metal oxides and sulfides 219
4.1.2. Polyanion-based compounds. . . . 220
4.2. Specific examples of recent developments 220
4.2.1. Nanostructured cathode materials 221
4.2.2. Nanocomposites of cathode materials 222
4.2.3. Surface modification of cathode materials 223
4.2.4. Nano-architectured cathode electrodes 224
4.3. Summary 224
4.4. Remaining challenges 225
4.5. Opportunities and new directions 225
5. O_2-breathing cathodes for Li-air batteries 226
5.1. Different cell configurations and electrode reactions 226
5.2. Electrodes in a non-aqueous electrolyte 227
5.2.1. Porous carbon-based electrodes 227
5.2.2. Bifunctional catalysts for oxygen reduction and evolution 229
5.3. Electrodes in an aqueous electrolyte 232
5.3.1. Porous carbon-based electrodes 233
5.3.2. Bifunctional catalysts for oxygen reduction and evolution 233
5.4. Summary 236
5.5. Remaining challenges 236
5.6. Opportunities and new directions 237
6. *In situ* characterization of electrode materials 237
6.1. Synchrotron-based X-ray techniques 237
6.1.1. X-ray diffraction (XRD) 237
6.1.2. X-ray photoelectron spectroscopy (XPS) 238
6.2. *In situ* XAS experiments for the study of Li batteries 239
6.2.1. Soft X-ray XAS 239
6.2.2. Hard X-ray XAS 242
6.2.3. Reaction dynamics. . . . 242
6.3. Nuclear magnetic resonance (NMR). . . . 244
6.4. Raman spectroscopy 245
6.5. Comparison of information depths for different measurements. . . . 248
6.6. Future directions of *in situ* characterization of Li batteries. . . . 248
7. Conclusions and outlook 248
Acknowledgements 249
References 249

1. Introduction

The desire to develop a more sustainable transportation system, the necessity to lower our dependence on fossil fuel, and the demand for a clean and secure energy future are pushing the development of low or zero emission electric and hybrid electric cars powered by a new generation of electric energy storage (e.g., batteries and supercapacitors) and conversion (e.g., fuel cells) systems. Further, electric energy storage systems play an indispensible role in smart grids to manage the mismatch between electricity generation and demand, especially for electricity generation from renewable and sustainable sources (such as solar, wind, and geothermal) because of their intermittent and cyclic nature. Even for the conventional power plants, efficient load-leveling (by storing energy in batteries and chemical fuels and tapping such energy later) can dramatically improve energy efficiency, reliability, and energy security while reducing emissions of green house gas and air pollutants (e.g., CO_2, SO_2, and NO_x). Even in the sector of portable electronics such as hand-held communication devices, computers, and cordless tools, batteries often function as the primary power sources and thus greatly influence the performance, portability, and reliability of these devices.

Among all types of batteries, lithium batteries have attracted the most attention because the theoretical energy density (both gravimetric and volumetric) of lithium metal is the highest for all solid electrodes [1–3]. To date, unfortunately, it has been difficult to build a rechargeable battery based on metallic lithium anode with satisfactory cycling life, due primarily to lithium dendrite formation during charging, which can result eventually in shorting between the two electrodes, a catastrophic failure of battery [4]. When a lithium-insertion or alloying compound, rather than metallic lithium, is used as the negative electrode material, we have a lithium-ion battery, a family of rechargeable batteries widely used today. The use of lithium intercalation/alloying compounds for both anode and cathode has successfully enhanced not only the cycling life but also other desirable battery characteristics such as safety and rate capability. During discharge, lithium ions move spontaneously through the electrolyte from the negative to the positive electrode as electrons flow, through an

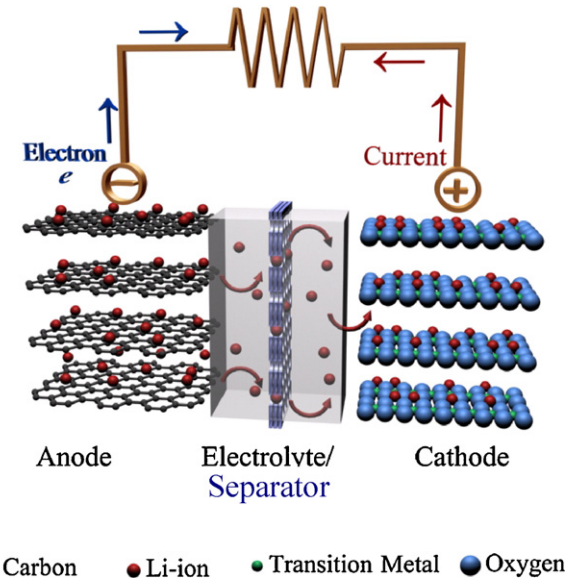

Fig. 1. Schematic illustration of a typical lithium-ion battery where graphite and $LiCoO_2$ are used as anode and cathode, respectively.

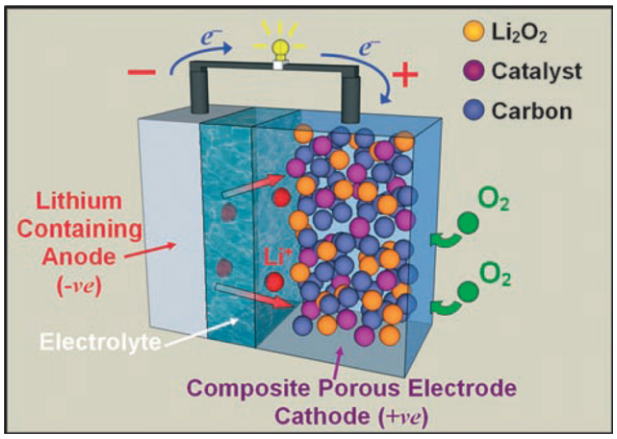

Fig. 2. Schematic illustration of a lithium-air battery where the lithium-containing anode is electrochemically coupled to atmospheric oxygen through a porous O_2-breathing cathode [11].

external circuit, from the negative to the positive electrode, generating electrical power. During re-charge, both lithium ions and electrons are driven back in the opposite direction by an applied external voltage, storing electrical energy as chemical energy in the battery. Schematically shown in Fig. 1 is a lithium-ion battery constructed from a carbon-based anode (e.g., Li_xC_6), an intercalation compound cathode (e.g., $LiCoO_2$), a liquid electrolyte (e.g., $LiPF_6$ dissolved in a mixed organic solvent of ethylene carbonate and dimethyl carbonate), and a separator. The current lithium-ion batteries represent the state-of-the-art battery technology and are widely used for many applications, notably for portable electronics. For now and in the foreseeable future, lithium-ion batteries are and will be the most practical solutions to a wide variety of electrical energy storage applications [5].

It is well known, however, that the energy densities of the current lithium-ion batteries are limited mainly by the inherent low energy density of the available cathode materials, the conventional intercalation compounds [6]. When the heavy cathode material in a lithium-ion battery is replaced by a light-weight, porous (usually carbon-based) O_2-breathing electrode, we have a lithium-O_2 or lithium-air (if the O_2 comes from ambient air) battery with dramatically higher theoretical energy density [7]. As schematically shown in Fig. 2, the lithium-containing anode (or metallic lithium) is electrochemically coupled to atmospheric O_2 through a porous O_2-breathing positive electrode. During charge and discharge, lithium ions and electrons will transport between the positive and the negative electrodes the same way as they do in a rechargeable lithium-ion battery, but the electrochemistry at the surface of an O_2-breathing cathode (positive electrode) is very different, as to be discussed later in detail. This lithium-air battery system is perceived to be the next generation of electrical energy storage system because it holds promise to offer much higher (>4 times when including the mass of O_2, ~10 times when excluding the mass of O_2) energy density than the state-of-the-art lithium-ion batteries (150–200 Wh/kg_{cell}) [5,8–10]. The projected obtainable or "practical" energy density of a Li-air battery approaches that of gasoline for automotive applications: ~1700 Wh/kg_{cell}, making it a very attractive power option for electric vehicles and many portable electronic devices [8]. While this projection is reasonable (considering that the theoretical energy density for Li-air battery is about ~11,000 Wh/kg), numerous scientific and technical challenges are yet to be overcome to produce a reversible and efficient O_2-breathing electrode in order to realize this potential. To date, in fact, the overall performances of any available Li-air battery are still far inferior to those of the best available Li-ion battery, implying that there is still a long way to go to develop a useful Li-air battery technology.

The practical energy and power density, cycling life, cost, and safety characteristics of both lithium-ion and lithium-air batteries are determined critically by the composition, morphology, and the microstructure of the electrode materials used. In order to achieve long cycling life, the desired characteristics of electrode materials include high specific charge density (available charge per unit mass and volume of the material), high cell voltage (difference between the redox potentials of the cathode and the anode materials), high reversibility of electrochemical reactions, with minimum change in the dimension, crystal structure, and morphology of the functional components during cycling. For high power density or rate capability, the electrode materials must also have proper architecture and nano-structure to facilitate fast charge transfer across interfaces and rapid transport of reactants to (and products away from) active sites for electrode reactions [12]. Thus, design of electrode materials with proper composition, morphology, microstructure, and architecture is vital to the creation of a new generation of batteries with performance far better than those of the existing ones [13].

In this review, we start with a brief assessment of the fundamental scientific challenges faced by battery development and why nanostructures and nano-architectures may help us to transcend these challenges, as discussed in Section 2. We then provide a comprehensive review on some recent advancement in design, synthesis, and fabrication of a variety of nanostructured electrode materials for lithium-ion and lithium-air batteries with enhanced energy and power density, energy efficiencies, reliability, and cycling life. In particular, several effective strategies used to enhance battery performance will be highlighted, including reduced dimensional nanostructuring, surface coating, nanocomposite, and nano-architecturing. Section 3 focuses on approaches to achieving high-performance anode materials, Section 4 summarizes recent progress in enhancing the performance of insertion compounds as cathodes for lithium-ion batteries, and Section 5 reviews new developments in exploring O_2-breathing cathodes for lithium-air batteries. These discussions represent the current understanding of the existing Li-ion and Li-air batteries. In many cases, however, mechanistic details of electrode processes are still missing although the battery performance characteristics may

have been dramatically enhanced by a particular effective approach (e.g., a nanostructure or a nano-architecture). To stimulate more interests in gaining fundamental understanding of mechanistic details, we also provide an overview on some powerful, *in situ* characterization techniques suitable for probing and mapping electrode properties, or for tracking structural evolution of electrode materials, with high sensitivity and spatial resolution under battery operating conditions. When coupled with electrochemical and other *in situ* measurements, they are capable of providing information vital to unraveling the mechanism of charge and mass transfer processes associated with battery cycling, as discussed in Section 6. A fundamental understanding of electrode reaction mechanisms and the detailed charge and mass transport processes is imperative to gaining some critical insights into rational design of better electrodes. Finally, the outlook and perspective for future generation of batteries with performance far exceeding the existing ones is outlined in Section 7.

2. Nanostructures to transcend challenges

2.1. Scientific and technical challenges facing the development of Li batteries

2.1.1. Challenges associated with Li-ion batteries

Some of the major challenges facing the advancement of the current Li-ion battery technology can be briefly described as follows:

- The obtainable or usable capacity is inadequate (and lower than the theoretical ones) and diminishes with the rate of cycling.
- The power density (or rate capability) is insufficient for the intended applications.
- The energy efficiency is too low due to large polarization losses for charge and discharge, more so at higher cycling rates.
- The cycling life is limited due to capacity fading with cycling.

Since many electrode materials have inadequate electronic conductivity (e.g., $LiFePO_4$ [14]), carbon black (or other highly conductive particles) are often added to the electrode for current collection. Usually, carbon and particles of active electrode materials are uniformly mixed and bound to a metal foam/mesh current collector using a binder such as polyvinylidene fluoride (PVDF). To make effective use of all active electrode materials, carbon and the particles of electrode materials must be in intimate contact. At the same time, all carbon particles must maintain connected to the metal foam/mesh to efficiently collect (or inject) electrons from (or to) active electrode materials during cycling. Worsening of electrode performance originates often from some unfavorable changes in electrode microstructure during cycling. For example, deterioration in connectivity between carbon particles or between carbon and the particles of active electrode materials may lead to capacity fading (due to electrical isolation of active electrode materials), increased electrode polarization (due to increased resistance to charge transport), and reduced rate of cycling.

In general, the performance of the existing Li-ion batteries is often limited by the deterioration in microstructure or architecture of the electrodes associated with volume expansion or contraction, phase transformation, and morphology change of the active electrode materials during cycling, as briefly described below.

(1) *Morphology and microstructure change*: Considerable change in the shape, size, distribution, and connectivity of each phase in a composite electrode during cycling may result in undesirable redistribution or segregation of phases, leading to electrical isolation of active electrode materials (thus capacity fading), weakening connectivity between carbon particles (thus increased resistance to current collection and charge transfer), and worsening transport of electro-active reactants to (or products from) active sites (increased resistance to mass transfer and reduced rate of charge and discharge). As an example of morphology change during charging, lithium dendrite formation may cause partial shorting of the two electrodes and eventually catastrophic failure of battery operation.

(2) *Volume change of active electrode materials*: The volume expansion (or contraction) of active electrode materials associated with lithium insertion/alloying (or extraction/de-alloying) may induce stress and strain in the electrodes, which result eventually in pulverization of active electrode materials or mechanical disintegration of the electrode. This in turn leads to gradual fading in obtainable capacity and rate of operation during cycling due to electrical isolation of more active particles/phases from current collectors, reduced connectivity between carbon particles, and increased resistance to the transport of electro-active species to or from active sites. Volume change is inevitable in all electrode materials during cycling, but especially severe in Li alloying compounds. For example, the molar volume of $Li_{4.4}Si$ is $\sim$4 times that of Si [15]. The large cyclic volume change upon alloying/de-alloying of Li in/from Si pulverizes the electrodes during cycling, resulting in loss of capacity and poor performance.

(3) *Structural change* (*or phase transformation*): In addition to changes in morphology, microstructure, and volume during cycling, the crystal structure of the active electrode materials may change as well, leading to new phases with poor electronic or ionic conductivity, degraded flexibility for the insertion or extraction of Li, and thus diminished capacity retention. For example, $LiMn_2O_4$ undergoes a phase transformation from the cubic structure to the tetragonal structure, leading to severe capacity fading, more so at a higher cycling rate. This structural change may be inherent to a particular composition under certain conditions; however, nanostructured electrodes are proven to be effective in improving the kinetics of phase transformation and minimizing undesirable consequences. For instance, when ultrathin $LiMn_2O_4$ nanowires with diameters less than 10 nm were used as cathodes, more facile structural transformation was observed in a large composition range with high reversibility and good capacity retention [16].

(4) *Formation of insulating phases*: In some battery systems (e.g., Li/S battery), insulating reaction products may coat on active electrode surfaces, blocking the transport of electro-active species to the active sites and diminish the activity of the covered surface [17].

2.1.2. Challenges associated with Li-air batteries

For a Li-air battery, additional difficulties include much lower practical energy density (than the theoretical one), much larger polarization resistance during both discharge and re-charge, and lower cycling rates (than the current Li-ion batteries). These problems are due primarily to the inefficiency of the O_2-breathing electrode, including transport of oxygen through the pores and, more importantly, the deposition of insulating products on active sites for oxygen reduction and evolution, as described below.

(1) *Oxygen transport*: Unlike the electrodes for Li-ion batteries, the O_2-breathing electrode for a Li-air battery must be porous with sufficient porosity and minimal tortuosity to facilitate O_2 transport to (or from) the active sites for electrode reactions on the interior surface of the porous electrode with minimum energy loss. It must also have adequate electrical conductivity to inject (collect) electrons to (from) these active sites for oxygen reduction (evolution). While the resistance to the

transport of O_2 and Li ions through the pores decreases with porosity, the resistance to electron transport (through the solid phase of the porous electrode) increases with porosity. Similarly, as the feature size of the porous electrode microstructure (e.g., pore size and grain size) is reduced, the resistances to charge transfer across the interface (electrode reaction) are reduced since the surface area and hence the number of active sites for electrode reaction may increase; however, the resistances to transport of O_2, Li ion, and electrons are increased because the increased tortuosity for fluid flow through the porous structure and for electron transport through the solid phase. Often, opposing or conflicting factors must be carefully compromised to optimize electrode performance.

(2) *Effective loading of catalysts*: Another complication associated with a Li-air battery is that catalysts (e.g., precious metal such as Au and Pt [18] or transition metal oxides such as α-MnO_2 [11]) may have to be introduced to the electrode surface in order to enhance the electrode kinetics and reduce the energy loss associated with the discharge–charge polarization. Proper loading and distribution of these catalysts can critically impact the performance. A simple approach is to mix carbon (the electrode) and catalyst particles uniformly and bound then to a metal mesh or foam current collector using a binder, similar to a composite electrode used for Li-ion batteries. A typical O_2-breathing electrode have a weight ratio of carbon: α-MnO_2:PVDF = 54:10:36 [8].

(3) *Deposition of insulating products*: Yet another difficult problem associated with the O_2-breathing electrodes in non-aqueous electrolytes is the deposition of insoluble reaction products Li_2O_2 (and some Li_2O under certain conditions) at the active sites for electrode reactions. Once a conformal dense product layer is formed on the entire active surface of the electrode, ionic/electronic transport through the product layer is required to sustain the electrode reaction. Because of the poor electronic conductivity of the product Li_2O_2, the discharge current density diminishes rapidly with the growth of the product layer on electrode surface due to worsening of electrical conduction through the product layer, leading eventually to termination of electrode reaction.

2.2. Unique attributes of nanostructures and nano-architectures

2.2.1. Why do nanomaterials behave differently?

Fast transport of mobile species: It is well known that when the dimension of materials, grains, or domains becomes comparable to (or less than) the characteristic length scale (such as the mean free path) of phonons, photons, electrons, ions, and molecules, many physical phenomena involving them are strongly influenced, often leading to new modes for the transport of charge, mass, and energy and for chemical and energy transformation processes. As shown in Table 1, the length scales of mobile species in batteries (electrons, ions, and molecules) fall generally in the order of 0.1–100 nm in typical electrochemical systems, suggesting that some unique physicochemical properties of materials and novel reaction pathways may become operative in the nanoscale regime. Thus, materials with proper nano-scale dimensions and architectures (with reduced length scale and characteristic time scale of physical phenomena) have the potential to dramatically enhance the transport of electrons, ions, and molecules associated with cycling of batteries, significantly accelerating the rate of chemical and energy transformation processes.

Enhanced surface reactivity: The ratio of the number of surface atoms to that of bulk atoms for a nanomaterial is far greater than that for a bulk material (>100 nm). Surface atoms have fewer neighbors than the atoms inside the bulk, leading to lower coordination numbers and more unsatisfied bonds. The large surface free energy, surface defects, and surface states may critically influence the chemical reactivity of materials [20]. For example, there could be higher density of corner or edge atoms, which have even lower coordination numbers and greater activity toward other atoms and molecules. Vacancies or other defects not seen in bulk materials may exist on the surface of nanostructures, which may greatly enhance the rate of electrochemical reactions.

Table 1
Characteristic length and time scales for electrons, molecules, and ions under ambient condition.

Energy carriers	Wavelength/nm	Mean free path/nm	Relaxation time/ns
Electrons			
In semiconductors/dielectrics	~1–50	~1–500	$\sim10^{-3}$ to 10^{-2}
In conductors/metals	~0.1–1	~1–10	$\sim10^{-5}$ to 10^{-4}
Molecules/ions			
In gas/plasma	$\sim10^{-2}$ to 1[a]	$\sim10^{3}$ to 10^{7}	~1–100
In liquid/electrolyte	–	~0.1–1	$\sim10^{-3}$
In solid/electrolyte	–	~0.1–1	$\sim10^{-3}$

Data taken from [19].

[a] Refers to de Broglie wavelength.

The large surface free energy and stress/strain of nanomaterials may fundamentally influence the phase stability and structural transformations, which in turn influence the electrochemical and catalytic activities. The surface free energy of nanomaterials can be estimated as,

$$\mu^{\circ}(r) = \mu^{\circ}(r=\infty) + 2\left(\frac{\gamma}{r}\right)V$$

Here $\mu^{\circ}(r)$ and $\mu^{\circ}(r=\infty)$ refer, respectively, to the chemical potential of nano and bulk materials, γ is the effective surface tension, r is the effective grain radius, and V is the partial molar volume. Clearly, the surface energy increases dramatically with decreasing particle size. As a result, phases that may not be stable in bulk materials can become stable in nanostructures and vice versa. This structural instability associated with size has been observed in many oxide systems such as TiO_2 [21,22] and Al_2O_3 [23]. Size-induced modification of lattice parameters has been observed in many oxide nanoparticles including Fe_2O_3 [24] and CeO_2 [25].

Mechanical robustness: Nanostructured materials are known to exhibit significantly enhanced mechanical strength, toughness, and structural integrity [26–29], although the underlying mechanisms are yet to be fully understood [27,28,30] and nanocrystalline materials with grain size less than 100 nm are still a subject of active research [29,31–34]. In particular, some naturally evolved nanostructures (e.g., diatom shells) are extremely resilient to mechanical stress and strain. Diatoms are single-celled microorganisms that form rigid shells (frustules) composed of amorphous silica (SiO_2) with unique nano-architectures. These remarkably strong frustules have evolved as mechanical protection for the cells; exceptional stresses and strains are required to break them, as illustrated in Fig. 3 [35–37].

2.2.2. Unique advantages of nanostructured electrodes for Li batteries

Materials with a wide variety of nanostructures or nano-architectures can help us to transcend the difficulties facing the development of electrodes for high-performance batteries. The benefits of electrode materials with nanostructures and nano-architectures are briefly summarized as follows.

(1) Large surface area (or surface to volume ratio) increases the contact area between electrode and electrolyte and hence the

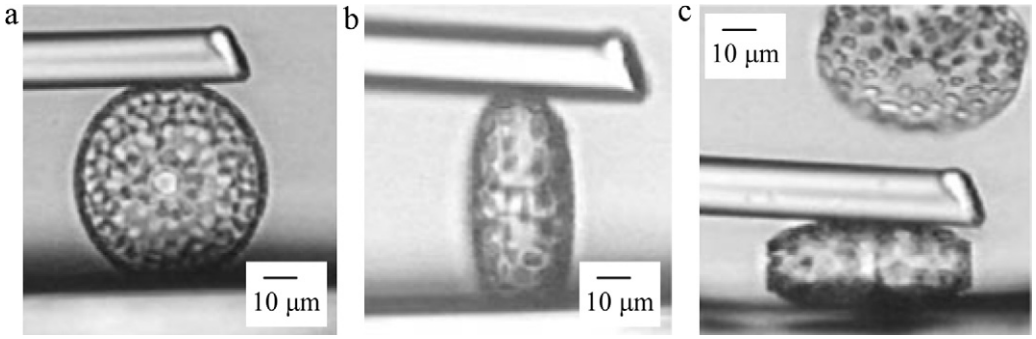

Fig. 3. Glass needle test conducted on live single diatom cells (Thalassiosira punctigera) to demonstrate that they can withstand extreme strains without fracture. Adapted by permission from Macmillan Publishers Ltd.: Nature [35], copyright 2003.

number of active sites for electrode reactions, which in turn reduces electrode polarization loss and improves power density (or rate capability), energy efficiency, and usable energy density (especially when the utilization of active electrode materials is increased). Further, it offers increased flexibility for surface modification to achieve multi-functionality: enhanced surface catalytic activity for intended electrode reactions, improved surface transport of electro-active species, as well as tailored surface passivity against undesired electrode–electrolyte reactions by the formation of desired solid–electrolyte interphase (SEI). This advantage is especially important for Li-air batteries, where catalytic activity for oxygen reduction (during discharge) and evolution (during recharge) is vital to reduce polarization losses, to enhance cycling rates, and to improve usable energy density. For electrode materials with very low electronic conductivity (e.g., LiS_x), large surface to volume ratio increases the contact area between electrode and distributed current collectors to make efficient use of the electrode materials, which in turn increases the usable energy density and reduces electrode polarization loss [38]. Similarly, for insoluble and insulating reaction products in a Li-air battery, nanostructures with large surface to volume ratio are vital to achieving high energy density, rate capability, and reasonable cycling life.

(2) Short diffusion length associated with the nano-sized dimensions of nanostructured electrodes effectively reduces the distance that Li ions and electrons must travel during cycling in the solid state through electrode materials. Often, electrode materials with other desirable characteristics may have limited ionic and/or electronic conductivity, which can limit the power density (or the rate of operation), the usable energy density (due to limited utilization of active electrode materials), and energy efficiency (due to mass transport limitation in the solid state). This can be effectively mitigated by the use of nanomaterials. For solid-state diffusion of Li in electrode materials, the characteristic time constant for diffusion (equilibration time), τ, is determined by the diffusion constant, D, and the diffusion length, L, according to:

$$\tau = \frac{L^2}{D}$$

The time for Li intercalation, τ, decreases with the square of the diffusion length, L, illustrating the remarkable effect of manipulating nanostructures: fast Li storage in nanomaterials and high rate capability (high power). For example, the diffusion length would be reduced to the diameter of nanowires, -tubes, and -rods and the thickness of thin films if they are properly dispersed in the electrolyte (ionic conductor) and the current collector (electronic conductor). Much unique architecture has also been incorporated in integration of low-dimension nanostructured components to achieve fast mass transport and high power density.

(3) Enhanced ionic and electronic conductivity can also be achieved by thin film deposition of an excellent electronic or ionic conductor, or by the formation of nano-composites, in which the surface of each phase or the interfaces between phases support fast transport of ionic and electronic species. Some of the enhanced ionic and electronic transport is still not fully understood. While electroneutrality should be obeyed in bulk of a homogeneous materials, a space-charge zone can be created at the interface of nanomaterials [39]. These narrowly charged interfaces can provide fast pathways for ionic and electronic species, leading to enhanced energy storage process. Furthermore, nanomaterials may have more ionic and electronic defects not only on the surface and interfaces but also in the bulk phase, which could change the ionic and electronic conductivity as well.

(4) Improved mechanical strength and structural integrity represent other unique properties of well-designed nanomaterials. It is well known that low-dimensional nanomaterials (e.g., nanowires, -tubes, -belts) have high mechanical strength, more resistance to mechanical damage, and can be engineered to allow volume change only in certain directions or dimensions. For example, the internal small pores in nano-porous composite electrodes can accommodate the large volume expansion and contraction associated with charge–discharge cycling without mechanical damage or deterioration in microstructure. This attribute ensures the structural integrity of the electrodes, minimizing or eliminating capacity fading due to electrical isolation of active electrode materials originated from pulverization of electrodes, as demonstrated in three-dimensional porous silicon particles [40]. Silicon nanowire electrodes also shows very promising performance with much improved cycling performance due to facile strain relaxation in the silicon nanowires [15] as illustrated in Fig. 4. As another example, while the bulk form of layered $LiMnO_2$ often suffers from capacity fading due to structural instability, nanocrystalline $LiMnO_2$ shows better accommodation of the lattice stress caused by Jahn-Teller distortion, displaying much higher and more stable performance [41]. In nanoparticles, the charge accommodation can occur mostly at/near the surface and greatly reduces the need for diffusion of Li ions through bulk materials [42]. This substantially reduces the volume changes and stresses associated with Li insertion and removal.

(5) Hierarchical architecture of nano-porous structures can improve electrocatalytic activity and stability because of enhanced transport of reactants to (or products away from) the nano-sized pore surfaces, the high surface areas for surface modifications to improve catalytic properties, and the robust structure for durability. Enhanced electrocatalytic activity is due to increased number of active reaction sites and facile

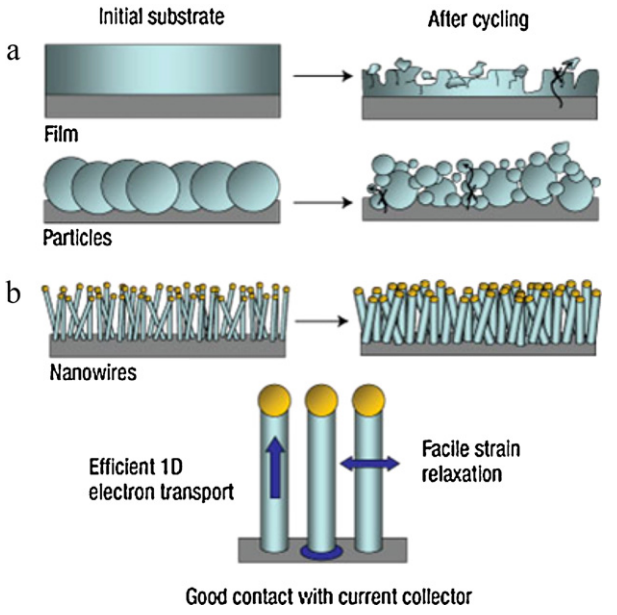

Fig. 4. Schematic illustration of morphological changes of different Si-based electrodes: (a) thin film and bulk powders, and (b) Si nanowires.
Adapted by permission from Macmillan Publishers Ltd.: Nat. Nanotechnol. [15], copyright 2008.

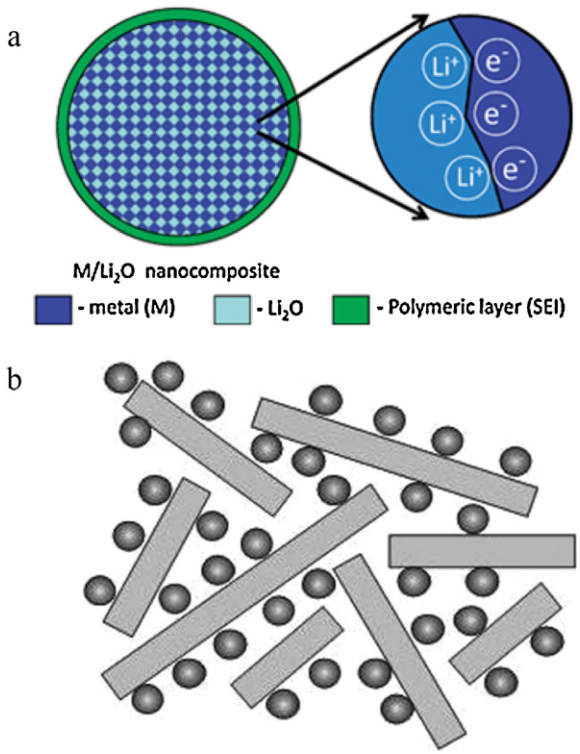

Fig. 5. Schematic illustration of interfacial storage mechanism in (a) transition metal oxides [45], reproduced by permission of the Royal Society of Chemistry, and (b) graphene sheets [47].
Copyright Wiley-VCH Verlag GmbH & Co. KGaA. Reproduced with permission.

transport of electro-active species to the reaction sites. The nanopores with higher surface area per unit mass allow for better dispersion of catalysts, whereas the large pores allow for infiltration and filling of ionomer (i.e., Li-ion conducting polymer) to maximize the three-phase boundaries (i.e., oxygen, electron, and Li^+), thus increasing the number of active sites and allowing for better utilization of all catalyst particles.

(6) Nanostructured materials can lead to new Li-storage mechanisms, enabling higher capacities than conventional intercalation mechanisms. Recent studies show that lithium ions can be stored on the surface [43], interface [39,44,45], and in nanopores [46,47] without causing any mechanical crumbling in the electrode, thus leading to excess lithium storage. In particular, surface/interfacial Li storage mechanisms will play more important roles in transition metal oxides and newly emerging graphene-based electrodes as shown in Fig. 5.

(7) It has been observed that electrode materials which are inactive toward Li insertion in bulk form become active on the nanoscale [12]. These findings have led to revisiting electrode materials thought to be non-promising in the past. Specific examples include nano-sized transition metal binary oxides with conversion reactions. Similarly, multielectron conversion reactions with metal oxyfluorides which showed poor performance in the bulk form become promising in the nanoscale regime [48].

(8) Further, the redox potentials of electrode materials can also be modified by nanostructures, resulting in a change of cell voltage or energy density [49]. Recently, Balaya et al. measured the excess cell voltage of 62 mV for TiO_2 nanoparticles compared to bulk TiO_2 [45]. It was also demonstrated that reducing the particle size of amorphous RuO_2 can significantly enhance the potential for Li insertion by 580 mV, compared to bulk crystalline RuO_2 as shown in Fig. 6 [50].

2.2.3. Disadvantages of nanostructured electrodes

It is noted, however, that nanomaterials may incur high fabrication cost due to complex synthetic processes, low volumetric energy density due to reduced packing density of nanoparticles, and undesired side reactions between the electrode and electrolyte due to large surface areas. Also, nanomaterials tend to form agglomerates during the electrode fabrication process, making it difficult to uniformly disperse them in the electrodes, and their nanoscale dimensions are rather difficult to control. For Li-air batteries, nanoparticulated catalysts can suffer from thermodynamic instability under electric field. This is often observed in polymer electrolyte membrane (PEM) fuel cells [51], critically affecting their long-term durability and preventing their commercialization. These shortcomings can be mitigated if the nanostructure and fabrication process are properly designed, offering significantly improved battery performance.

2.2.4. Novel strategy: bio-inspired nanostructures

When a conventional battery electrode, consisting of carbon and active electrode material powders bound with a binder, is replaced by a hierarchically structured 3D porous assembly, the mechanical integrity, robustness, and micro-structural stability can be dramatically enhanced. For example, nature-designed,

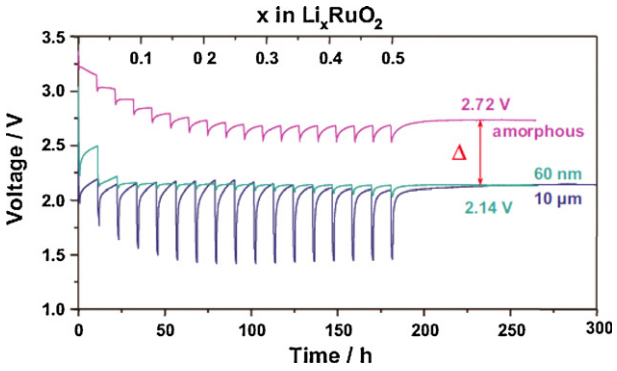

Fig. 6. Galvanostatic intermittent titration technique (GITT) measurement on RuO_2/Li cells with different particle size [50].
Copyright Wiley-VCH Verlag GmbH & Co. KGaA. Reproduced with permission.

hierarchically structured 3D porous assemblies may be used as a frame or scaffold for battery electrodes to dramatically enhance mechanical robustness, structural stability, and electrochemical catalytic activity by allowing for more accessible surfaces with shorter diffusion distances.

In recent years, attempts to learn from nature's assembly of high precision and robust materials have attracted much attention [52–54]. Shown in Fig. 7 are some inspiring examples of diatoms. As mentioned previously, diatoms form rigid cell walls (frustules) composed of amorphous silica (SiO_2). There are over 10,000 diatom species in nature, each of them forming a hierarchically structured frustule with a unique, genetically determined, 3D shape and pattern of nano-scale features.

These unique 3D porous structures have been successfully replicated by Sandhage et al. using a "shape preservation process" to produce porous materials with a wide variety of chemical compositions but nearly identical shapes and similar nanostructures [55,56]. In combination with a sol–gel and an atomic layer deposition (ALD) processes, both the structures and chemistries of the porous materials can be tailored over multiple length scales and over three dimensions [57]. The use of these unique porous structures can greatly enhance the performance of electrodes for batteries. In the next three sections, many other examples will demonstrate that a variety of nanostructured materials can indeed dramatically enhance the performance of Li-ion and Li-air batteries.

3. Anode materials for Li-ion batteries

3.1. Classification of anode materials

3.1.1. Lithium metal and carbonaceous materials

While metallic lithium has very high energy density (3860 mAh/g), the use of lithium metal as an anode material in rechargeable batteries was largely hindered by safety concerns related to its low melting point (~180 °C), dendrite growth during charging, and high reactivity toward electrolytes [58]. The use of lithium insertion compounds (e.g., carbonaceous materials) rather than metallic lithium resulted in the so-called "rocking chair" or lithium-ion battery. For example, carbon-based anode materials were commercialized by Sony in 1991. Since then, the performances of lithium insertion compounds have been significantly improved, including energy density, rate capability, and cost. Today, graphite-based anodes with a theoretical capacity of 372 mAh/g are still used in most conventional lithium-ion batteries [59,60].

3.1.2. Lithium alloying compounds and intermetallic alloys

Despite the significant advances in carbonaceous materials, new anode materials of higher energy density are needed. Since the 1970s, a wide variety of lithium alloying systems has been developed as an alternative anode material. Examples include metals that can store a large amount of lithium through the formation of alloys like $Li_{4.4}Si$, $Li_{4.4}Ge$, LiAl, $Li_{4.4}Sn$, and Li_3Sb [1]. The major problem with lithium alloys is their significant volume expansion and contraction, which takes place during the charging and discharging process. This may lead to pulverization of the electrode materials and poor cycling performance.

The displacement reaction of intermetallic materials with lithium is another approach. Much effort has been devoted to exploring intermetallic materials by embedding an electrochemically active metal such as Sn or Sb in an inactive matrix in an attempt to accommodate the large volume expansion that occurs during the lithiation process with pure metals [61,62]. Intermetallic electrodes of ternary systems exhibit good cycling properties, and a strong structural relationship exists between a parent binary intermetallic electrode AB and a lithiated Li_xAB product. For example, Cu_6Sn_5 [63], InSb [64], and Cu_2Sb [65] electrode materials have been reported as potential anode materials. Even though these materials have high volumetric energy density, their gravimetric energy density is relatively low, and capacity fading with cycling is significant.

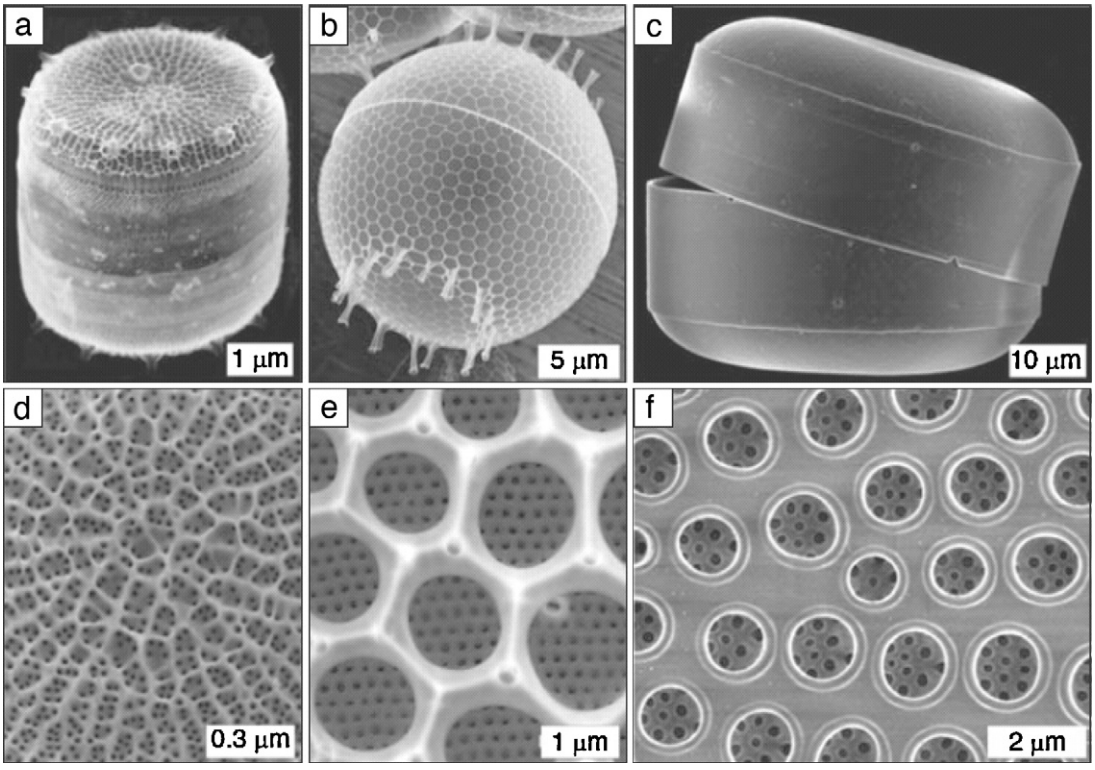

Fig. 7. SEM images of diatoms: (a, d) Thalassiosira pseudonana, (b, e) Stephanopyxis turris, and (c, f) Coscinodiscus granii [52].

3.1.3. Transition metal compounds

In addition to lithium alloys, conversion reactions have been used to produce nanocomposite electrode capable of storing lithium. In this process, a compound MX (where M represents a 3d transition metal and X represents O, F, N or S) is reduced by Li to the metal M and a corresponding lithium compound as follows [61,66–68]:

$$M_mX_n + 2nLi^+ + 2ne^- \leftrightarrow nLi_2X + mM$$

This conversion reaction may allow the storage of more than two lithium ions per molecule, potentially offering high capacity and good reversibility. For example, Poizot et al. reported that nano-sized binary transition metal oxides (e.g., CoO, NiO, CuO, and FeO) exhibited electrochemical capacities of 700 mAh/g, with 100% capacity retention up to 100 cycles [66]. The enhanced electrochemical reactivity of Li_2O is attributed to the unique nanostructure consisting of uniformly dispersed nano-sized (~5 nm) transition metal phase and lithium oxides. The outstanding reversible electrochemical properties can be explained by very short diffusion lengths and large contact areas. While nano-sized transition metal oxides exhibit excellent electrochemical performance, their application in practical Li-ion batteries is hindered by high synthesis cost, relatively poor rate capability (or power density), and low volumetric density.

Early transition metal oxide anodes have also been proposed for application in rechargeable lithium batteries; in particular, the use of lithium intercalated titanium oxide [69,70]. $Li_4Ti_5O_{12}$ is described as a zero-strain insertion anode due to the negligible volume change during the lithium insertion/extraction process. In addition, $Li_4Ti_5O_{12}$ is considered a safe anode since it does not react with organic electrolytes. The drawbacks of the lithiated titanium oxide, however, are its high redox potential (~1.5 V vs. Li/Li^+) and low capacity [71,72].

3.2. Specific examples of recent developments

Bulk anode materials used in commercially available batteries have relatively low power densities because of the slow charge/discharge rate. To improve the rate capability and durability of lithium-ion batteries, nanostructured anodes (e.g., Si- or Sn-based nanowires, nanotubes, and hollow spheres) and nanocomposite anodes (e.g., Si dispersed in carbon nanotube (CNT) matrix, TiO_2 functionalized graphene, and ternary metal oxide systems) have been developed in order to reduce the diffusion length and increase the tolerance to volume change. Surface coating or modification of anode materials has also been used to improve electrical conductivity and electrochemical performance, including carbon coatings by spray-pyrolysis, thermal decomposition, and carbonization of organic precursors. Other examples include synthesis of hybrid nanostructures consisting of Sn nanoclusters on SnO_2 nanowires, nitration-driven conductive $Li_4Ti_5O_{12}$, and coating of stabilizer (e.g., SiO_2, Al_2O_3, Nb_2O_5, or RuO_2) onto surface of TiO_2 nanotubes. Very recently, the nano-architectured anode electrodes (e.g., Fe_3O_4-based Cu nano-architectures, SnO_2 nanorod arrays onto flexible Fe–Co–Ni substrate) displayed outstanding capacity retention and rate capability.

Summarized in Table 2 are some typical performances of various nanostructured anode materials reported in the literature. More details of recent advancements in design, synthesis, and fabrication of a variety of nanostructured anode materials with enhanced performance are provided in the following sections, with an intention to highlight the important nanostructured features that offer significant potential to advance energy storage characteristics.

3.2.1. Nanostructured anode materials

3.2.1.1. Nanowires, nanorods, nanotubes, 3D porous particles. Lithium alloying compounds: As mentioned above, many materials (such as Si, Al, Sn, Sb, and Ge) are capable of accommodating Li by the formation of lithium alloys (Li_xM) and show Li storage capacities far higher than those of carbonaceous materials. However, many of these materials such as tin ($Li_{4.4}Sn$) and silicon ($Li_{4.4}Si$) exhibit significant volume changes (>300%) during Li alloying and dealloying, leading to cracking and crumbling of the electrode materials and the consequent loss of electrical contacts between particles, resulting in severe capacity loss [83–89]. To overcome this problem, one strategy is to use nanostructured materials like nanowires, nanotubes, and 3D porous particles, which can accommodate large strain with good electrical contact without pulverization during discharge/charge cycling.

Table 2
Electrochemical performance of nanostructured and bulk anode materials.

Anode materials	Capacity (mAh/g)		Current density	Voltage (V)	References
	Initial	After *n*th cycle			
Silicon bulk particles	~3260	~200 (10th)	100 mA/g	2.0–0.0	[73]
3D porous silicon	~3138	~2800 (100th)	400 mA/g	1.5–0.0	[40]
Silicon nanotubes	~3200	~3000 (80th)	3000 mA/g	1.5–0.0	[74]
Silicon nanowires	~4200	~3300 (10th)	210 mA/g	2.0–0.01	[15]
SiO_x/C coating on Si nanoparticles	~2200	~1100 (60th)	150 mA/g	1.0–0.05	[118]
Si/CNT composite film	~2400	~1600 (50th)	360 mA/g	1.0–0.01	[75]
Co_3O_4 bulk particles	~1200	~80 (20th)	111 mA/g	3.0–0.0	[76]
Co_3O_4 nanoparticles	~1230	~200 (60th)	100 mA/g	3.0–0.005	[77]
Co_3O_4 nanowires	~1300	~200 (60th)	100 mA/g	3.0–0.005	
Mesoporous Co_3O_4	~1330	~820 (60th)	100 mA/g	3.0–0.005	
Self-supported Co_3O_4 nanowires	~1124	~700 (20th)	111 mA/g	3.0–0.0	[76]
Non-supported Co_3O_4 nanowires	~1124	~350 (20th)	111 mA/g	3.0–0.0	
CuO particles (1 μm)	~400	~380 (70th)	0.2 C	3.0–0.02	[78]
CuO particles (0.15 μm)	~410	~100 (70th)	0.2 C	3.0–0.02	
CuO urchin structure	~800	~560 (50th)	150 mA/g	3.0–0.001	[79]
CuO hollow cubes	~967	~79 (50th)	150 mA/g	3.0–0.001	
CuO hollow spheres	~900	~91 (50th)	150 mA/g	3.0–0.001	
SnS_2 bulk particles	~401	~127 (30th)	50 mA/g	3.0–0.0	[80]
SnS_2 nanoplates	~1311	~583 (30th)	323 mA/g	1.1–0.001	[81]
SnS_2 nanoflowers	~1650	~502 (50th)	200 mA/g	1.2–0.05	[82]

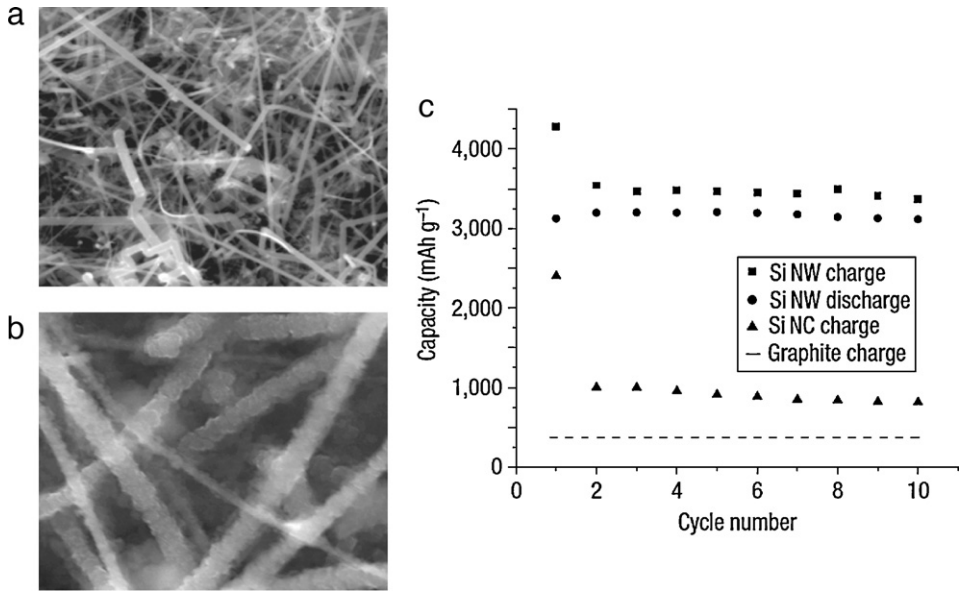

Fig. 8. SEM images of Si nanowires (a) before cycling and (b) after cycling at same magnification. (c) Capacity versus cycle number for Si nanowires at C/20 rate showing the charge (squares) and discharge capacity (circles).
Adapted by permission from Macmillan Publishers Ltd.: Nat. Nanotechnol. [15], copyright 2008.

Since silicon has a high theoretical capacity, it has been widely investigated as an alternative to graphite. Cho's group extensively studied silicon-based nanostructured anodes. For example, 3D porous Si particles were synthesized via a thermal annealing and wet etching process [40]. They found that porous silicon particles with a thin pore-wall thickness of ~40 nm could accommodate large strains without pulverization and reported excellent cycling performance (99% and 90% capacity retention after 100 cycles at a rate of 0.2 C and 1 C, respectively). These capacity retentions were far superior to previously reported nano-sized Si/carbon composites or Si nanoparticles. It was found that pores in Si particles could act as a "buffer layer" for alleviating the large volume changes during lithium insertion and extraction.

Cui's group reported the improved performance of silicon nanowires grown directly on a stainless steel current collector using a gold catalyzed vapor–liquid–solid (VLS) process [15]. This concept has several advantages. First, the small nanowires allow for better accommodation of the large volume variations induced by the lithium insertion/removal process. Second, each Si nanowire is directly grown on the current collector, such that all Si nanowires contribute to the capacity, and no binders or conducting additives are required. Third, one-dimensional Si nanowires allow for efficient charge transport. Due to these unique features, Si nanowires grown directly on the current collector have exhibited outstanding electrochemical performance. As shown in Fig. 8, the reported initial capacities were very high with a coulombic efficiency of ~73%. Both charge and discharge capacities were nearly constant with little degradation up to 10 cycles.

As described above, 3D porous silicon particles and silicon nanowires have shown good cycling performance as anode materials. However, they exhibit increased polarization at higher current rates and capacity fading during extended cycling, likely due to the limited surface area accessible to the electrolyte and the gradual growth of the SEI layer. The use of silicon nanotubes could be a good solution. Cho's group fabricated novel silicon nanotube structures by reductive decomposition of silicon precursor inside anodic alumina templates [74]. The use of silicon nanotubes increased the surface area accessible to the electrolyte, allowing lithium ions to intercalate from both the interior and the exterior of the nanotubes. Additionally, the surface of the Si nanotubes was coated with carbon, which stabilized the Si–electrolyte interface and promoted stable SEI formation during cycling. The nanotube electrodes demonstrated reversible charge capacities of ~3200 mAh/g with capacity retention of 89% after 200 cycles at a rate of 1 C in practical lithium ion cells with improved rate capability (Fig. 9).

Besides the silicon-based anode electrodes, Ge nanowire electrodes were also fabricated onto a metallic current collector using the VLS growth process [90]. The Ge nanowires showed an initial discharge capacity of 1141 mAh/g at C/20 rate over 20 cycles. High power rates were observed up to 2 C with a coulombic efficiency of above 99%.

Transition metal compounds: In addition to lithium alloying compounds, transition metal compounds with conversion reactions can also benefit from nanostructures. For instance, Li et al. synthesized mesoporous Co_3O_4 nanowires using a template-free method at mild conditions [76]. These Co_3O_4 nanowires of 500 nm in diameter and 15 μm in length were grown on Si, glass, Cu, or Ti foil. The Co_3O_4 nanowires underwent a conversion reaction, forming metallic Co nanodomains embedded in the Li_2O matrix. Despite the compositional transformation, the nanowire arrays maintained their structural integrity after many cycles. After the first cycle, the subsequent cycles exhibited high reversible capacity of 700 mAh/g after 20 cycles. In cases of non-supported nanowires and commercially available powders, however, poor electrochemical performance was observed, showing the advantages of the directly grown nanowire structure.

Also, α-Fe_2O_3 nanorods with diameters of 60–80 nm and lengths of 300–500 nm were synthesized using a hydrothermal method. Liu et al. reported significantly improved capacity and cycling stability (763 mAh/g capacity after 30 cycles), compared to microcrystalline α-Fe_2O_3 powders [91]. Electrochemical characterizations using cyclic voltammetry and electrochemical impedance spectroscopy also confirmed that α-Fe_2O_3 nanorods exhibited higher activity than the microcrystalline counterpart. The enhanced performance was attributed to the shorter Li^+ diffusion pathways through the one-dimensional nanostructured electrode.

3.2.1.2. Unique shape/morphology. Designing the unique shape or morphology of electrode materials is also important to enhance

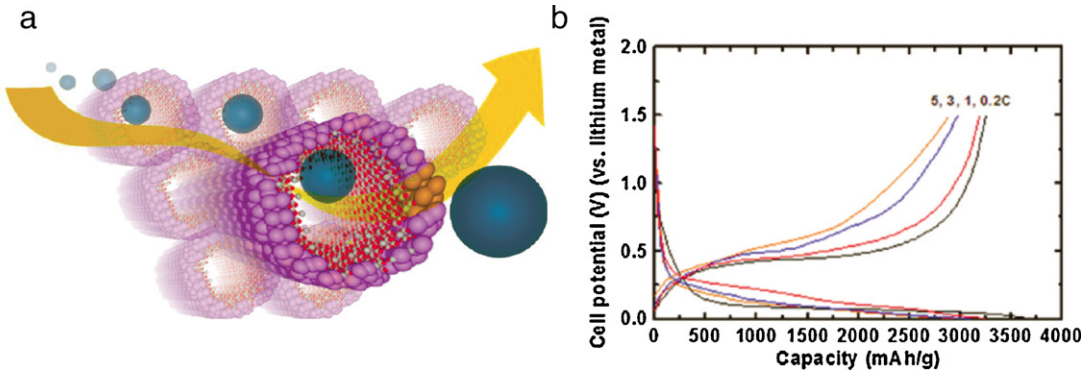

Fig. 9. (a) Schematic diagram of Li-ion pathways in Si nanotubes, (b) rate capability of Si nanotube anodes cycled between 0 and 1.5 V. Reprinted with permission from [74]. Copyright 2009 American Chemical Society.

electrochemical performance. Yu et al. prepared a novel nanostructured carbon-free Li_2O–CuO–SnO_2 anode material consisting of hollow porous spheres with a mean diameter of 5 μm using the electrostatic spray deposition [92]. The porous spheres consist of the multideck-cage structure, where the thickness of the backbone ranges from 60 to 100 nm and the pore diameters range from 200 nm to 1 μm (Fig. 10). The Li_2O–CuO–SnO_2 (Li/Cu/Sn = 1:1:1) thin film electrode shows a high reversible capacity of ~1190 mAh/g and nearly 100% capacity retention after 100 cycles at 0.5 C in the voltage range of 0.01–3 V. Even at a high rate of 8 C, excellent rate capability was seen with a capacity of 525 mAh/g. Its outstanding electrochemical performance is ascribed to several reasons: (i) the unique porous structure increases electrode–electrolyte contact area; (ii) the multideck-cage structure accommodates the volume change during the charge/discharge process; and (iii) Li_2O can suppress the aggregation of the Li–Sn alloy.

Urchin-like structures are also attractive in that the surface area of the active materials can be increased, and its volume expansion during the lithiation/delithiation process can be alleviated, compared to normal spherical electrode materials. Recently, Zhang et al. fabricated urchin-like carbon materials composed of carbon nanofibers grown on the surface of natural graphite spheres using a metal catalyzed CVD process [93]. The urchin-like carbon electrodes showed remarkably improved cycling performance and better rate capability compared to the pristine graphite materials.

Park et al. developed an approach for gram-scale synthesis of Cu_2O nanocubes using a one-pot polyol process [79]. As-synthesized Cu_2O nanocubes were converted into CuO hollow cubes, hollow spheres, and urchin-like particles by controlling the amount of aqueous ammonia solutions added in air. Among CuO materials, the urchin-like electrodes retained high capacities of above 560 mAh/g up to 50 cycles. The good cycling performance of urchin-like particles might be attributed to the structural robustness and the stability of the large single-crystalline domains.

In addition to urchin-like structures, meshed plate structures composed of SnO nano-sized ribbons can also be used as an anode material. Uchlyama et al. prepared single-crystalline SnO meshed plates through $Sn_6O_4(OH)_4$ as the intermediate state using an aqueous solution process [94]. The SnO meshed plates exhibited good cycling performance with a reversible capacity of 320 mAh/g after 20 cycles, while SnO flat plates had a lower capacity of 250 mAh/g. This indicates that the meshed electrodes with a specific skeletal framework offer a sufficient buffer to accommodate large volume expansion during the lithiation/delithiation process; thus, the nanostructured mesh plates showed improved cycling performance. Various morphologies of anode materials have also shown improved electrochemical properties, including SnS_2 nanoparticles [95], SnS_2 nanoplates [81], SnS_2 flower-like structures [82], and SnO_2 nanosheets [96].

3.2.2. Nanocomposites of anode materials

Nanostructured anode materials (e.g., Si or Sn-based materials) exhibiting high capacity are considered one of the best alternatives for carbon anodes. To preserve the unique nanostructures, however, nanostructured anode materials are often dispersed in a carbon-based matrix. Carbon is not only electronically conductive but also

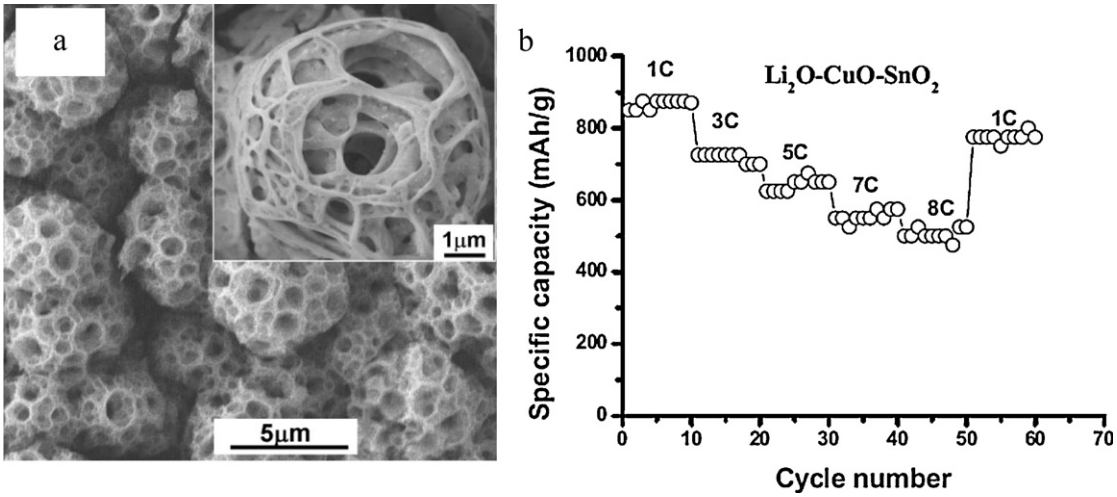

Fig. 10. (a) SEM image of porous, multideck-cage morphology of Li_2O–CuO–SnO_2. (b) Cycling performance and rate capability of a Li_2O–CuO–SnO_2 thin film [92]. Copyright Wiley-VCH Verlag GmbH & Co. KGaA. Reproduced with permission.

contributes to the capacity. Several composites consisting of nanostructured anode materials and carbon have shown good electrochemical performance, including higher capacity and excellent cycling retention compared to the pristine nanostructured anode or bare carbonaceous material.

Si-based anodes: In particular, many research efforts have been devoted to combining the advantages of carbon and silicon in order to improve electrochemical properties. Recently, Hu et al. proposed a new strategy to synthesize meso- and macroporous carbon using phase separation between mesophase-pitch and polystyrene homopolymers [97]. Silicon nanoparticles of 20–100 nm in size were dispersed in the porous carbon materials, which showed a very stable reversible capacity of 450 mAh/g during lithiation/delithiation process up to 50 cycles.

Cui's group used the supercritical fluid–liquid–solid (SFLS) process to make silicon nanowires, which were mixed with amorphous carbon or multiwalled-CNTs (MW-CNTs) as anodes for lithium ion batteries [98]. They found that carbon-coated silicon nanowires mixed with MW-CNTs exhibited a capacity of 1500 mAh/g during the first 30 cycles, while those mixed with amorphous carbon blacks showed a capacity of just 500 mAh/g. This improvement was attributed to the high conductivity and good connectivity of the network between silicon nanowires and MW-CNTs.

As a more efficient strategy, Cui's group also prepared free-standing CNT–silicon film composites by integrating a conductive network of CNTs into the silicon film [75]. First, CNTs dispersed in water were spread out onto stainless steel mesh plates; then, silicon thin films were deposited onto the CNT networks by a CVD process using silicon precursors. The CNT acts as both mechanical support and electrical conductor, while Si thin films act as high capacity active materials for lithium ion batteries. The CNT–Si nanocomposites showed a high charge storage capacity of ~2000 mAh/g with good cycling retention (80% capacity retention after 50 cycles at a rate of C/15), much better than for sputtered-on silicon films (Fig. 11).

Sn-based anodes: Similarly, Sn–C nanostructured composites also showed excellent electrochemical performance [99–101]. For example, Scrosati's group reported Sn–C nanostructured composites prepared by the infiltration of tin precursor into a resorcinol–formaldehyde gel, followed by subsequent calcination in an inert gas [101]. The as-prepared tin nanoparticles of 10–50 nm in size were uniformly dispersed in supporting carbon matrix (Fig. 12). The Sn–C composite materials exhibited a specific capacity of 500 mAh/g for 200 cycles and were cycled at a rate of 5 C, recovering 40% of the total capacity, thus demonstrating significantly enhanced electrochemical performance of the novel, unique design of the Sn–C nanocomposites.

The composite of CNTs and Sn-based materials is another interesting example [102–104]. Kumar et al. reported Sn-filled

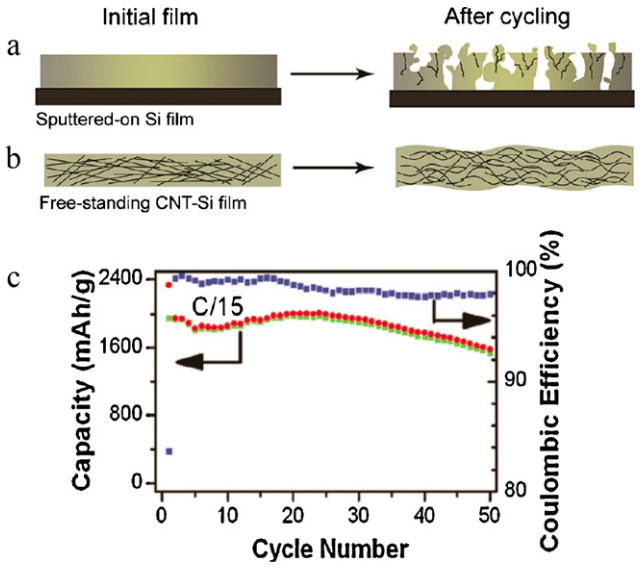

Fig. 11. Schematic illustration of (a) pulverization of sputtered-on Si film after cycling and (b) better accommodation of large strain by CNT-Si films. (c) Charge (red circle) and discharge (green square) capacity and corresponding coulombic efficiency (blue square) of CNT-Si film as the working electrode cycled between 1 and 0.01 V. (For interpretation of the references to color in this figure legend, the reader is referred to the web version of the article.)
Reprinted with permission from [75]. Copyright 2010 American Chemical Society.

CNTs using a hydrothermal reduction process [104]. The CNTs synthesized by catalytic decomposition were oxidatively opened and filled with a tin precursor by capillary force. Subsequent $NaBH_4$-reduction or hydrothermal process led to the reduction of tin precursor to tin metal. These nanocomposite electrode materials showed a high capacity of ~1080 mAh/g for the hydrothermal product and ~1600 mAh/g for the $NaBH_4$ product at a rate of 0.1 C. Both capacity and cycling retention were significantly improved compared to the unsupported Sn and CNTs.

Recently, Ortiz et al. proposed a novel route for fabricating SnO nanowires inside TiO_2 nanotubes which can be used as high power density lithium ion microbatteries [105]. Initially, titania nanotubes were prepared by the anodization of titanium foil; subsequently, tin and tin oxide nanowires were grown inside titania nanotubes by electrodeposition. The nanocomposite comprising SnO of 2 μm in length and 20 nm in diameter showed a reversible capacity of ~140 μAh/cm^2, ~85% of which was maintained over 50 cycles because the titania nanotubes allowed for volume variation associated with the lithiation/delithiation process, thus enhancing electrochemical performance. In addition, SnO_2 nanoparticles encapsulated in crystalline carbon hollow spheres [106], SnO_2/CNTs nanocomposites synthesized in supercritical fluids [107],

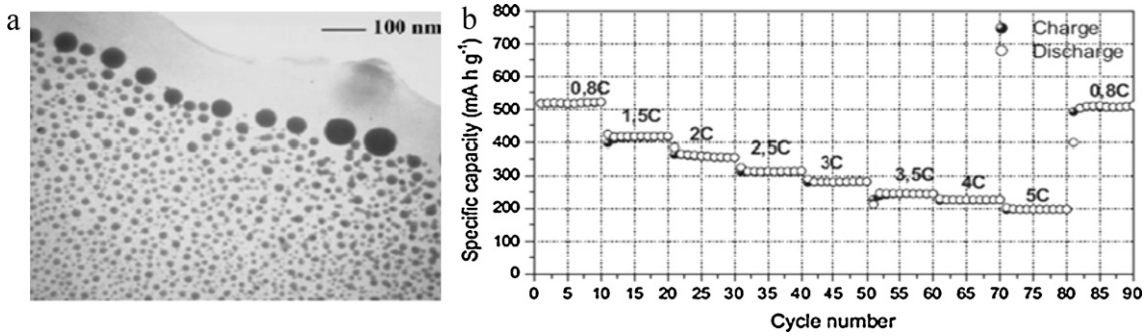

Fig. 12. (a) TEM image of Sn–C composite material. (b) Cycling performance at various rates [101].
Copyright Wiley-VCH Verlag GmbH & Co. KGaA. Reproduced with permission.

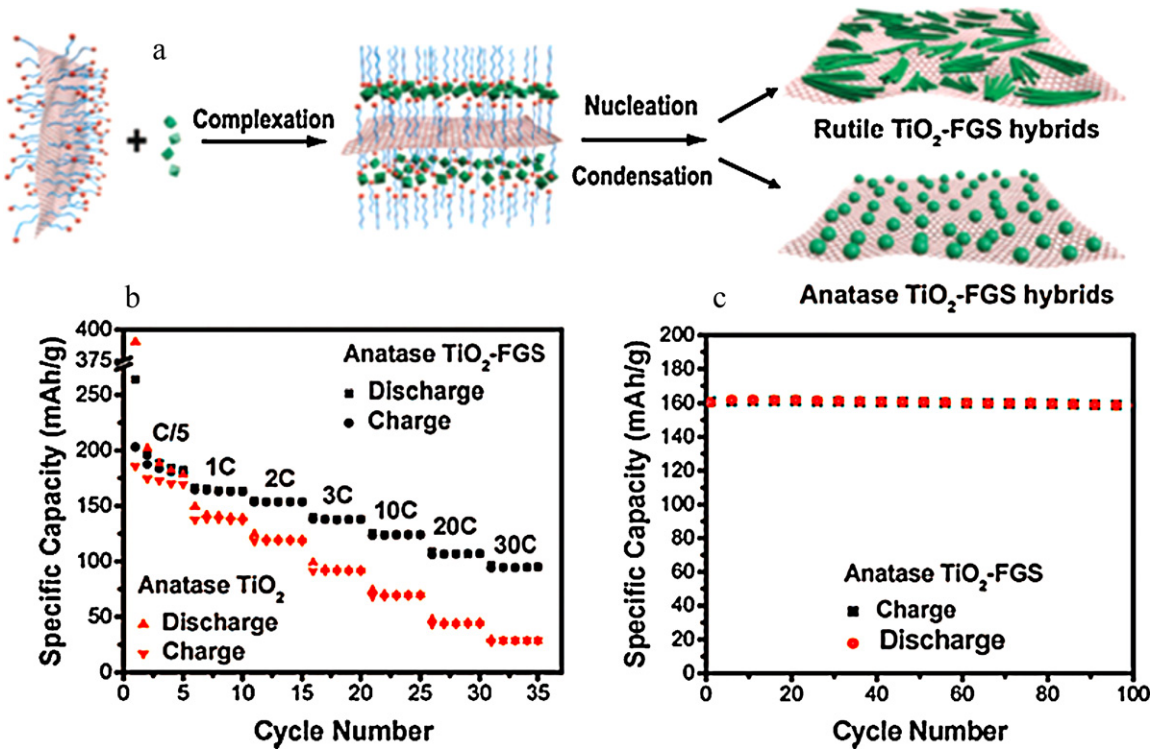

Fig. 13. (a) Synthesis of self-assembled TiO_2-functionalized graphene sheets (FGS) hybrid nanostructures. (b) Comparison of specific capacity of anatase TiO_2 and the anatase TiO_2-FGS hybrids at different charge/discharge rates. (c) Cycling performance of the anatase TiO_2-FGS up to 100 cycles at 1 C charge/discharge rates. Reprinted with permission from [111]. Copyright 2009 American Chemical Society.

hollow sphere shaped SnO_2/C composite [108], and SnO_2 nanotubes and CNTs composites prepared by the layer-by-layer deposition technique [109] and ordered, nanostructured SnO_2/carbon composites [110] also exhibited good electrochemical performance.

Transition metal compounds: Graphene-based nanocomposite electrodes are also attractive for improving electrochemical properties. Recently, Wang et al. prepared self-assembled TiO_2–graphene hybrid nanostructured materials using highly dispersed functionalized graphene sheets (FGS) [111]. The novel strategy was to disperse graphene sheets uniformly with an anionic sulfate surfactant and then proceed with self-assembly of the surfactant with the titanium precursor to generate the desired TiO_2 morphology (Fig. 13). The specific capacity of the anatase TiO_2–FGS hybrid composite was superior to that of rutile TiO_2–FGS and pure TiO_2. The hybrid nanocomposite electrodes also showed excellent cycling performance over 100 cycles.

Kim et al. proposed a ternary metal oxide system ($Ca_3Co_4O_9$) as a novel anode material for lithium ion batteries due to its high electrical conductivity, high thermal stability, oxidation resistance, and reduced toxicity [112]. By Li-driven conversion process, which led to the formation of Co nanoclusters embedded in an amorphous Li_2O–CaO matrix, this nanocomposite electrode showed improved cycling performance and better rate capability. The electrical conductivity of the sintered $Ca_3Co_4O_9$ (34 S/cm) is much higher than that of typical spinel-type Co_3O_4 samples (1.96×10^{-5} S/cm) at room temperature [113]. The calculated theoretical capacity of $Ca_3Co_4O_9$ after the first cycle is 571.8 mAh/g. For comparison, the electrochemical performance of nano-sized $Ca_3Co_4O_9$, nano-sized Co_3O_4, commercial Co_3O_4 were also investigated (Fig. 14). The capacity retention of the nano-sized $Ca_3Co_4O_9$ electrode was better than for other particles. It should be noted that CaO, which only acts as an inactive matrix in the lithium batteries, may alleviate the mechanical stress induced by large volume change in the active materials and may prevent the aggregation of the Co nanodomains on cycling.

3.2.3. Surface modification of anode materials

The surface of an electrode material can greatly influence the electrochemical performance of the electrode. For example, a uniform and compact SEI film on the electrode surface may enhance the efficiency and capacity retention of the electrode. Therefore, coating or modifying the electrode surface allow for controlling the SEI layer as well as charge and mass transfer across the interface.

Carbonaceous materials: Pan et al. proposed the surface modification of natural graphite via molecular design [114]. Aromatic multi-layers of lithium benzoate were covalently

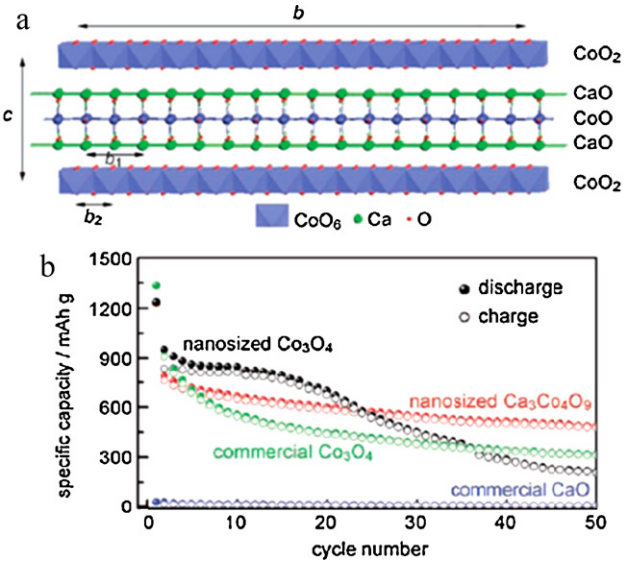

Fig. 14. (a) Proposed structural model for $Ca_3Co_4O_9$. (b) Discharge–charge capacity versus the cycle number for the nano-sized $Ca_3Co_4O_9$ and Co_3O_4 powders [112]. Copyright Wiley-VCH Verlag GmbH & Co. KGaA. Reproduced with permission.

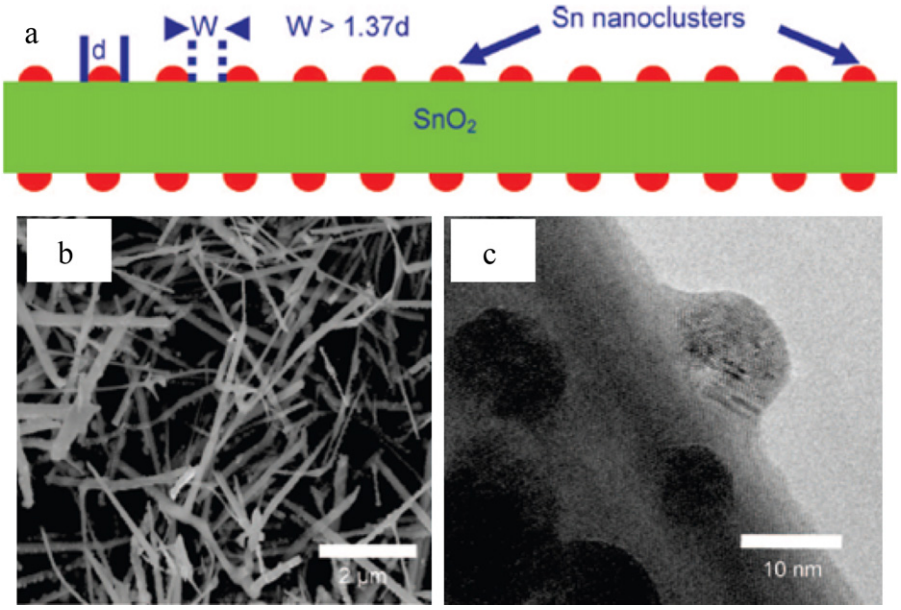

Fig. 15. (a) Schematic illustration showing evenly dispersed Sn nanoclusters on a SnO_2 nanowire surface with spacing controlled by the droplet diameter. (b) SEM image showing a network of Sn-nanocluster-covered SnO_2 nanowires. (c) HR-TEM image showing well-spaced crystalline Sn nanoculusters on the nanowire surface. Reprinted with permission from [119]. Copyright 2009 American Chemical Society.

attached to the surface of graphite using diazonium chemistry. The surface modified graphite electrode showed better electrochemical performance than pristine graphite. This is attributed to the formation of a stable and compact SEI layer that can accommodate the volume change associated with cycling.

Si-based anodes: The development of nanoscale coating on silicon-based structures is an effective approach to overcome the issues associated with the large volume changes. Ng et al. prepared Si/C nanocomposite materials using a spray-pyrolysis technique [99]. The specific capacity of spray-pyrolyzed carbon coated Si nanocomposites was 1489 mAh/g after 20 cycles; this result shows the beneficial effect of the pyrolyzed carbon coating on Si particles. Similarly, carboxyphenyl-group attached silicon anode materials [115] and phenol-functionalized silicon nanoparticles [116] also improved cycling performance by controlling the SEI layer.

Cui's group prepared a core–shell design of silicon nanowires for high power and long cycling life of lithium batteries [117]. In this strategy, they used an amorphous silicon shell as an electrochemically active material, while a crystalline silicon core was used as a support for amorphous silicon shell. The charge storage capacity was 1000 mAh/g with good capacity retention (90% over 100 cycles), and excellent rate capability was observed at a high charging and discharging rate of 6.8 A/g [117].

As another strategy, active silicon nanoparticles can be coated with inactive silica materials and conductive carbon together. Here, inactive materials play a key role in minimizing the mechanical stress induced by huge volume change in active silicon and thus prevents deterioration in electrochemical performance. Maier's group synthesized Si@SiO_x/C anode materials in a one-step procedure with a thin layer of SiO_x and carbon by a hydrothermal process and subsequent carbonization of glucose [118]. This Si@SiO_x/C structure, which has passivated SiO_x and conductive nanoscale coating of carbon, showed remarkably improved lithium-storage performance (~1100 mAh/g at 150 mA/g after 50 cycles).

Sn-based anodes: Recently, Meduri et al. presented a simple design of hybrid nanostructures involving Sn nanoclusters covered on SnO_2 nanowires as exceptionally stable anode materials with high reversible capacity [119]. The SnO_2 nanowires were synthesized by reacting Sn metal powders directly in the gas phase with oxygen containing plasma. Pure SnO_2 nanowires were exposed to H_2 plasma in a microwave CVD reactor to synthesize the Sn-nanocluster-covered SnO_2 nanowires (Fig. 15). A novel Sn/SnO_2 hybrid structure exhibited a reversible storage capacity of more than 800 mAh/g over 100 cycles. The capacity drop after the first few cycles was less than 1% per cycle.

Wang et al. proposed a new concept for the fabrication of porous SnO_2 nanotubes with coaxially grown CNTs [120]. The core–shell type SnO_2/C composite of ~73 wt.% SnO_2 and ~4 nm CNT thickness was synthesized by a vacuum infiltration of SnO_2 nanoparticles and CVD process. The SnO_2/CNT nanocomposite showed highly reversible capacity (540–600 mAh/g) and outstanding cycling retention (0.0375% capacity loss per cycle). The improved electrochemical performance is attributed to the tubular structure of SnO_2, better accommodation of volume expansion from CNT shell, the increased electrical contact areas from core–shell structures, and the enhanced lithium-ion transport.

Although hollow or nanotube-shaped particles have some advantages (e.g., alleviation of volume expansion, short diffusion length for lithium ions, and effective contact between electrode and electrolyte), the relatively low density of these materials results in low volumetric density of the electrode. To overcome this problem, Deng et al. synthesized mesoporous core/shell SnO_2 particles using a solvothermal method and subsequent calcination [121]. This material showed very high capacity for the first charge and discharge cycle of 2358 mAh/g and 1303 mAh/g, respectively, at a current density of 50 mA/g. This significantly enhanced first-cycle charge capacity might be attributed to SEI formation and the reduction of SnO_2 to Sn during lithiation. However, the capacity retention was not very good due to the thick shell layer and micrometer-sized particles (Fig. 16).

Transition metal compounds: As another strategy for improving electrochemical performance, surface conductivity of active materials can be improved by introducing a thin layer. Park et al. proposed a novel method for fabrication of nitration-driven conductive $Li_4Ti_5O_{12}$ for lithium ion batteries [122]. After thermal nitridation in an NH_3 atmosphere at 700 °C for 10 min, a thin layer of TiN was generated on the surface of $Li_4Ti_5O_{12}$ without changing the crystal structure of the pristine $Li_4Ti_5O_{12}$. The electrochemical performances of the pristine and the nitridated $Li_4Ti_5O_{12}$ electrode materials were compared at a rate of C/2 (Fig. 17). The pristine

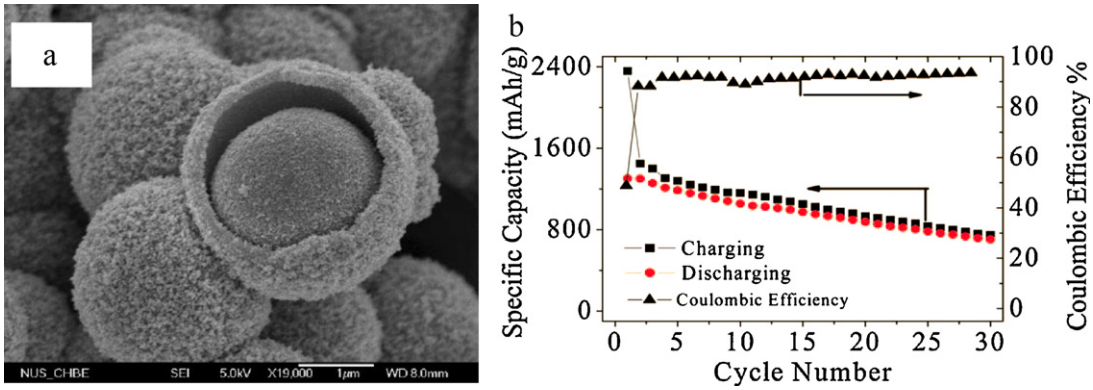

Fig. 16. (a) SEM image of SnO_2 hollow core–shell structure. (b) Specific capacity of hollow core–shell mesospheres of crystalline SnO_2 nanoparticle aggregates. Reprinted with permission from [121]. Copyright 2008 American Chemical Society.

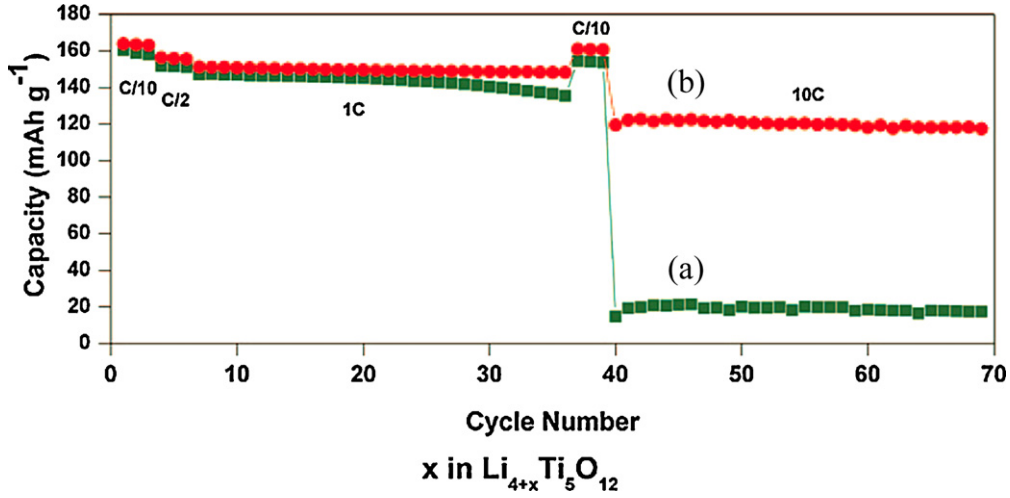

Fig. 17. Lithium insertion voltage curves of (a) pristine $Li_4Ti_5O_{12}$ and the nitration-driven conductive $Li_4Ti_5O_{12}$. Reprinted with permission from [122]. Copyright 2008 American Chemical Society.

$Li_4Ti_5O_{12}$ exhibited a specific capacity of 162 mAh/g; however, the capacity decreased with cycling. After nitridation, the $Li_4Ti_5O_{12}$ showed better performance at higher cycling rates. At a high cycling rate of 10 C, the nitridated $Li_4Ti_5O_{12}$ showed a capacity of ~120 mAh/g, about 6 times that for pristine $Li_4Ti_5O_{12}$. This is attributed to the surface coating of thin TiN layer and the mixed-valent intermediate phase, $Li_{4+\delta}Ti_5O_{12}$.

Even though a wide variety of nanostructured materials may be prepared under certain conditions, agglomeration or pulverization of nanoparticles may take place during heating or a cycling process. The problem of agglomeration can be avoided by introducing a thin wall and/or coating of carbon. However, the increase in carbon content may reduce the energy density, impede mass transport, and lower the rate of charge. Jamnik et al. developed a new strategy for stabilizing the size and morphology of active materials by coating a stabilizer onto an active particle surface [123]. When ceramic precursors of silica (SiO_2), alumina (Al_2O_3), and niobia (Nb_2O_5) were coated onto TiO_2 nanotubes, and then thermally treated at 480 °C, these coatings prevented particle growth and preserved the non-agglomerated form of the initial particulate materials. In contrast, without surface coating of these ceramic precursors, severe agglomeration took place upon heating. Moreover, TiO_2 stabilized with silica exhibited an excellent high-rate performance and showed a stable reversible capacity of 120 mAh/g at a very high rate of 20 C.

Guo et al. proposed the optimized nanostructure designs of electrode materials for high power and high energy density batteries by introducing highly lithium-permeable materials [124]. They designed the optimized nanostructure by preparing mesoporous anatase TiO_2 with a pore size of ~7 nm and by sequentially coating the pore channels with crystalline RuO_2, which acts as the electronic conductor and contributes to quick lithium permeation (Fig. 18). Moreover, the wetting characteristic of RuO_2 onto TiO_2 is very beneficial, since the low wetting angle of electrolyte on TiO_2 is helpful to better access of liquid electrolyte. The specific charge capacity of TiO_2/RuO_2 composite with a novel design was as high as 214 mAh/g at C/5 after 20 cycles. Even at a high rate of 30 C, the specific charge capacity reached 91 mAh/g, which is much better than that of pristine anatase TiO_2 (48 mAh/g).

3.2.4. Nano-architectured anode electrodes

Although nanomaterials generally exhibit better electrochemical performance than bulk materials, there are still considerable rooms for further improvement in the optimization of electrode design. For example, an efficient way to improve electrochemical properties is to optimize their architectures, such as particle size, shape, and space between particles.

For instance, Green et al. fabricated silicon pillar arrays that were separated to create free space in order to accommodate large volume expansion during the lithiation/delithiation process [125]. Using a similar approach, Taberna et al. fabricated Fe_3O_4-based Cu nano-architectured electrodes for lithium ion battery applications [126]. A 3D array of Cu nanorods was produced by electrodeposition onto Cu foil through a porous anodic alumina membrane that

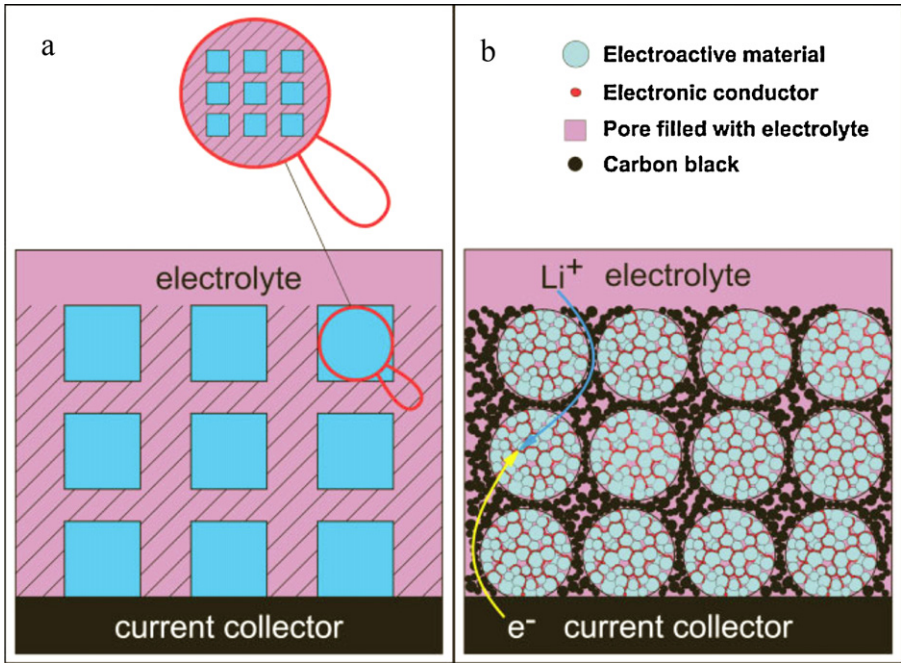

Fig. 18. Schematic illustration of (a) the desired design concept comprising a self-similar structure with efficient mixed conducting parts (shaded areas), and (b) a realistic composite electrode meeting this concept [124].

was subsequently dissolved. In a final step, Fe_3O_4 was electroplated onto Cu nanorods by cathodic reduction of an iron precursor in an alkaline solution (Fig. 19). Upon cycling, the self-supported Fe_3O_4/Cu nano-architectured electrodes exhibited outstanding capacity retention.

Scrosati's group also reported a new type of nano-architectured electrode configuration based on a template synthesis [127]. Initially, nano-architectured Cu nanorods with diameters of ~200 nm were fabricated from an electrodeposition process through an AAO membrane onto Cu sheets. Subsequently, Ni_3Sn_3 particles were coated onto nano-architectured Cu electrodes by electrodeposition with tin and nickel precursor solutions. The nanostructured Ni_3Sn_4 electrode materials showed a capacity of 500 mAh/g with the minimal decay over 200 cycles. The volume expansion upon lithiation was effectively buffered by the large empty space between the nanorods, resulting in excellent capacity retention at a high rate (10 C).

Grugeon et al. used a metallurgical oxidation method to prepare a nanostructured, electrochemically active chromium-rich oxide surface layer on a stainless steel current collector [128]. With chemical etching prior to high-temperature annealing, Cr-based oxide electrodes exhibited reversible capacities as high as 750 mAh/g for 800 cycles. Their modeling study suggested that self-supported structure of oxides with various porosities directly grown on current collector could improve the capacity beyond that of carbon-based electrodes, implying the importance of the unique architecture in achieving good adhesion between active materials and current collectors and ensuring an efficient pathway for electron transport.

3.3. Summary

While graphite is still the most commonly used anode material in current Li-ion batteries, the formation of a complex SEI layer on the surface of graphite raises safety concerns, especially in large batteries like those for use in electric vehicles. Additionally, the

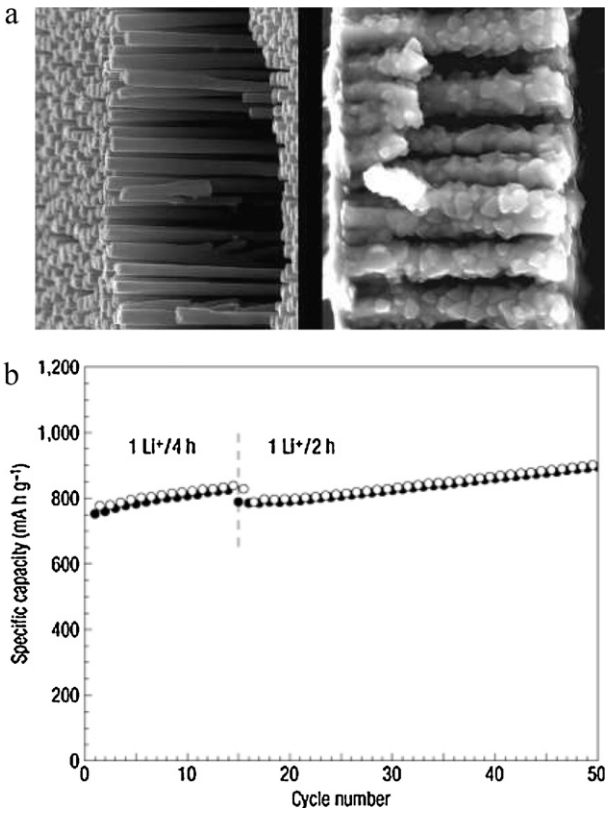

Fig. 19. (a) SEM images of cross-section of Cu nano-architectured current collector before (left) and after (right) Fe_3O_4 depositions. (b) Capacity retention of Fe_3O_4-based Cu nano-architectured electrode.
Adapted by permission from Macmillan Publishers Ltd.: Nat. Mater. [126], copyright 2006.

energy density of graphite is yet to be further improved to meet the stringent requirements of emerging applications.

To move beyond graphite anodes, enormous efforts have been devoted to the development of Li-alloy anodes, such as Li–Si and Li–Sn anodes, because their theoretical capacities greatly exceed that of graphite. However, their large volume change during cycling severely hinders their use in the market. Several unique nanostructures have been proposed and investigated in an effort to mitigate the problem. Among these, nanowires, 3D porous particles, and nanotubes have demonstrated excellent electrochemical performance due largely to their unique tolerance to large stress/strain induced during cycling. Nanoscale carbon coating also appears to be a very promising strategy, especially for Si-based anodes, which have low intrinsic electronic conductivity and large capacity loss in the early cycles due to the formation of an irreversible SEI layer.

Transition metal oxides with conversion reactions also display higher capacities than graphite. Although it has yet to be satisfactorily demonstrated, the reduction in particle size could improve the reversibility of Li_2O formation. Carbon coating could also enhance the rate capabilities and cycling performances of transition metal oxides by significantly improving their electrical conductivities.

Another promising candidate is spinel $Li_4Ti_5O_{12}$, which is very appealing as a safe anode material due to the excellent chemical stability of the Ti^{3+}/Ti^{4+} redox couple. It has been demonstrated that nitration-driven conductive $Li_4Ti_5O_{12}$ can show much improved performance at a high rate of lithium insertion without encountering any safety problems with the electrolyte.

3.4. Remaining challenges

As reviewed above, several nanostructured anode materials have been developed that have desirable electrochemical properties for overcoming some critical problems. However, a number of challenges still remain in the development of anode materials for a new generation of lithium batteries. Some of the major remaining challenges associated with the existing anode materials are briefly described below.

(1) Although lithium metal has very high theoretical energy density, lithium dendrite formation during charging can cause partial shorting of the two electrodes and may lead to eventual catastrophic failure of battery. Surface modification of lithium metal electrodes to minimize or eliminate dendrite formation represents a grand challenge to utilization of lithium metal electrodes.
(2) The obtainable capacities are often lower than theoretical capacities due to the low intrinsic electrical conductivity of active electrode materials, which decreases further with the rate of cycling.
(3) For transition metal oxides with conversion reactions, the rate capability (or power density) is still a concern, in addition to their relatively high potential (or low cell voltage) and limited lifetime due to capacity fading with cycling.
(4) For $Li_4Ti_5O_{12}$, improved safety is obtained at the expense of energy density, in addition to its high operating voltage vs Li/Li^+ ($\sim$1.5 V) or low cell voltage.
(5) Most anode materials undergo volume changes associated with lithium insertion/extraction (or alloying/de-alloying), which lead to pulverization of active electrode materials or mechanical disintegration of the electrode.
(6) Although Si-based anodes have shown very promising performance with the aid of various nanostructures (i.e., nanowires, 3D porous particles, and nanotubes), the complex synthesis processes may hinder the application to commercial batteries.

3.5. Opportunities and new directions

From a scientific point of view, more fundamental studies are needed to unravel the mechanism of electrochemical performance enhancement by nanostructures with different microscopic features (such as dimension, morphology, pore size and distribution). To date, little is known about the mechanism and sequence of elementary steps associated with charge and mass transport in the confined pores and channels. More sophisticated *in situ* characterization techniques for probing and mapping electrode surfaces and multi-scale modeling and simulations are needed to gain critical insights into nanoscale phenomena at electrode surfaces during cycling of batteries.

In addition, more extensive studies of novel architectures of anode materials are required. For example, arrays of vertically aligned carbon nanotubes are likely to be very promising when combined with high-capacity anode materials. Another strategy is to create 3D, nano-architectured structures in which pillared anodes and cathodes can be interdigitated. Additionally, combining microscale and nanoscale materials is another way to maximize the advantages and minimize the disadvantages of materials at the two different scales. Carefully designed and controlled architectures may lead to higher energy and power densities, significantly enhancing battery performance.

From a practical point of view, availability and cost of materials, potential for cost-effective synthesis and processing, improved safety, and minimal environmental impacts are equally important as performance. For example, nanostructured (nanowires, 3D porous particles, and nanotubes) Si-based anodes with carbon coatings have thus far shown very promising performance. However, the synthesis processes usually involve low yield, complex procedures and high cost, toxic precursors; thus, they are applicable only to limited applications. The development of large-scale, low-cost fabrication strategies for nanomaterials with desirable performance is an important challenge in the fabrication of battery materials for commercial applications.

4. Insertion compounds as cathodes for Li-ion batteries

4.1. Classification of cathode materials

4.1.1. Transition metal oxides and sulfides

Since the early 1970s, a variety of lithium intercalation compounds have been studied as the cathode for Li-ion batteries. The earliest lithium battery systems used metallic lithium (or Li–Al alloys) as the anode and various chalcogenides (TiS_2, MoS_2, etc.) as the cathode [6,129]. Of all layered dichalcogenides, titanium disulfide was widely studied since it has the highest gravimetric energy density. Cells consisting of lithium and titanium disulfide allowed deep cycling for close to 1000 cycles with minimal capacity loss. Cells with LiAl anodes and TiS_2 cathodes were commercialized from 1977 to 1979 by Exxon for small devices such as watches [130].

Surprisingly, layered oxide compounds with the same structures as the dichalcogenides were not studied in depth during that period of time, likely because their magnetic properties were of greater interest. Later, a number of groups studied oxides of manganese, cobalt, chromium, and other transition metals; however, lithium insertion into these compounds was not studied in detail. Goodenough's group found that $LiCoO_2$ had a similar structure as the layered dichalcogenides and showed that lithium could be extracted electrochemically [131]. Since then, $LiCoO_2$ cathode has dominated the lithium battery market. Cathode materials for current Li-ion batteries include mainly lithiated transition metal oxides like $LiCoO_2$ and $LiNiO_2$. In recent years, layered $LiMnO_2$, $LiNi_{1/2}Mn_{1/2}O_2$, and $LiNi_{1/3}Mn_{1/3}Co_{1/3}O_2$ have shown promise for higher capacity and energy density.

In addition to these layered structures, spinel cathode, $LiMn_2O_4$, which was originally proposed by Tackeray's group, has been extensively investigated by several groups because it is abundant, less expensive, and environmentally benign [132,133]. Currently, $LiMn_2O_4$ is one of the most important intercalation cathode materials for electric vehicle applications [134]. The disadvantage of this electrode, however, lies in its slow dissolution of manganese ions in the electrolyte during cycling [132,135].

4.1.2. Polyanion-based compounds

Transition metal oxides are widely used as cathode materials in lithium ion batteries; however, other new electrode materials have been developed for better safety and low cost. Examples include polyanion-based compounds obtained by introducing large polyanions of the form $(XO_4)^{y-}$ (X = S, P, Si, As, Mo, W) into the lattice. An inductive effect from $(PO_4)^{3-}$ and $(SO_4)^{2-}$ ions increases redox potential (compared to those in oxides) and stabilizes the structure [136]. Most metal phosphate and sulfate compounds have potentials in the range of 2.8–3.5 (versus Li/Li^+) [137]. These compounds usually have the advantages of better safety and lower cost, compared with the previous group. Until now, these materials have been widely studied as high performance cathode materials that can exhibit high capacity, high rate capability, and long cycling life.

Fluorophosphates are another class of cathode materials that serve as potential battery electrodes. These compounds exhibit high electrochemical cell potential due to the inductive effect of the $(PO_4)^{3-}$ group and the electron withdrawing property of the F^- ion. The first fluorophosphate material was $LiVPO_4F$, which is an iso-structure of minerals, tavorite ($LiFePO_4OH$) [138] and amblygonite ($LiAlPO_4F$) [139], as reported by Barker et al. [140]. Lithium extraction and insertion is accompanied by the reversible V^{3+}/V^{4+} redox reaction during electrochemical cycling, demonstrating an average discharge voltage of 4.06 V with a capacity of 123 mAh/g and good cycling performance of up to 300 cycles [141].

4.2. Specific examples of recent developments

Many cathode materials with layered, spinel, and olivine structures have low lithium diffusion coefficient and poor electrical conductivity. To overcome these limitations, several strategies have been explored to create unique nanostructured electrodes, including crystalline $LiMn_2O_4$ nanowires prepared using $Na_{0.44}MnO_2$ nanowires as a self-template, $LiMn_2O_4$ nanorods from chemical conversion of single crystalline β-MnO_2 nanorods, highly ordered mesoporous β-MnO_2, and olivine ($LiMPO_4$, M = Fe, Mn, Co) nanowires synthesized by microwave assisted solvothermal process.

Another strategy to overcome low intrinsic electronic conductivity of cathode materials is the use of a highly conductive network. Examples include (i) V_2O_5 aerogels with single-wall CNTs derived from a sol–gel process, (ii) composites of $LiFePO_4$ and multi-wall CNTs via hydrothermal, ball-milling, or a reaction process, (iii) Ni-V_2O_5 core–shell nanocable structures by an electrochemical deposition, (iv) Ag-$LiMn_2O_4$ and Ag-$LiCoO_2$ composite systems, and (v) composites of transition metal oxides and a conductive polymer (polyacetylene, polyaniline, or polypyrrole). These unique nanocomposite structures significantly improved cycling stability and rate capability.

Moreover, surface coating or modification of cathode materials also showed improved electrochemical performance. For example, carbon coatings on $LiCoO_2$ or $LiFePO_4$ improved capacity by reducing charge transfer resistance and facilitating lithium ion diffusion. Metal phosphate (e.g., $AlPO_4$ or $FePO_4$) coatings and metal oxide (e.g., ZrO_2, Al_2O_3, SnO_2, MgO, or ZnO) coatings on $LiCoO_2$ have also been used to suppress cobalt dissolution and improve uniform stress/strain distribution.

Summarized in Table 3 are some typical performances of various nanostructured cathode materials reported in the literature. More details of recent advancements in design, synthesis, and fabrication of a variety of nanostructured cathode materials with enhanced performance are presented in the following sections, with an intention to highlight the important nanostructured features.

Table 3
Electrochemical performance of nanostructured and bulk cathode materials.

Cathode materials	Capacity (mAh/g)		Current density	Voltage	References
	Initial	After *n*th cycle		(V)	
$LiCoO_2$ bulk particles	~60	~10 (14th)	1000 mA/g	4.5–2.5	[142]
$LiCoO_2$ desert rose	~155	~115 (14th)	1000 mA/g	4.5–2.5	
$LiCoO_2$ nanotubes	~185	~170 (100th)	10 mA/g	4.3–3.0	[143]
Mesoporous $LiCoO_2$	~98	~58 (50th)	30 mA/g	4.2–3.0	[144]
$LiCoO_2$ nanowires	~78	~38 (50th)	30 mA/g	4.2–3.0	
$LiMn_2O_4$ bulk particles	~40	~25 (100th)	5000 mA/g	4.5–3.1	[145]
$LiMn_2O_4$ nanowires	~108	~100 (100th)	5000 mA/g	4.5–3.1	
$LiMn_2O_4$ nanotubes	~138	~100 (100th)	10 mA/g	4.3–3.0	[143]
$LiMn_2O_4$ nanorods	~103	~85 (100th)	148 mA/g	4.3–3.5	[146]
$Li_{1.12}Mn_{1.88}O_4$ bulk particles	~215	~120 (10th)	30 mA/g	4.5–2.0	[147]
$Li_{1.05}Mn_{1.95}O_4$ bulk particles	~225	~160 (10th)	30 mA/g	4.5–2.0	
Mesoporous $Li_{1.12}Mn_{1.88}O_4$	~240	~225 (10th)	30 mA/g	4.5–2.0	
VOOH bulk particles	~102	~65 (50th)	20 mA/g	3.6–1.5	[148]
VOOH hollow dandelion	~140	~125 (50th)	20 mA/g	3.6–1.5	
$LiFePO_4$ nanoparticles	~111	~96 (30th)	42.5 mA/g	4.3–2.0	[149]
$LiFePO_4$-CNT composite	~115	~115 (30th)	42.5 mA/g	4.3–2.0	
C-coated $LiFePO_4$	~168	~165 (1100th)	100 mA/g	4.3–2.0	[150]
Polyacene-coated $LiFePO_4$	~133	~130 (250th)	170 mA/g	4.2–2.8	[151]
$LiFePO_4$ nanorods	~135	~90 (50th)	11.3 mA/g	4.3–2.0	[152]
$LiFePO_4$ nanorods/PEDOT	~166	~162 (50th)	11.3 mA/g	4.3–2.0	

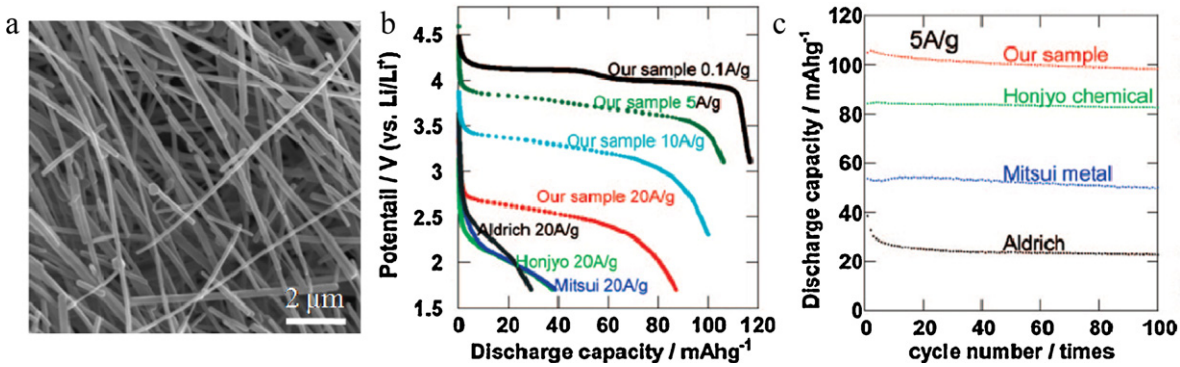

Fig. 20. (a) SEM image of single crystalline spinel $LiMn_2O_4$ nanowires. (b) The discharge curves of single crystalline spinel $LiMn_2O_4$ nanowires and commercial $LiMn_2O_4$ at various rates of 0.1, 5, 10, and 20 A/g. (c) Cycle performance of single crystalline spinel $LiMn_2O_4$ nanowires and commercial $LiMn_2O_4$ at a high rate of 5 A/g. Reprinted with permission from [145]. Copyright 2009 American Chemical Society.

4.2.1. Nanostructured cathode materials

4.2.1.1. Nanowires, nanorods, nanotubes, porous particles. Transition metal oxides: $LiMn_2O_4$ is one of the most popular cathode materials for lithium ion batteries used in electric vehicle applications. Compared to $LiCoO_2$, $LiMn_2O_4$ has several advantages: less toxicity, excellent thermal stability, abundance, and low cost. Recently, Hosono et al. synthesized novel single crystalline spinel $LiMn_2O_4$ nanowires using $Na_{0.44}MnO_2$ nanowires as a self-template [145]. As shown in Fig. 20, the as-prepared single crystalline $LiMn_2O_4$ nanowires have a diameter of 50–100 nm. The $LiMn_2O_4$ nanowires exhibited specific capacity of 118, 108, 102, and 88 mAh/g at a rate of 0.1, 5, 10, and 20 A/g, respectively, and demonstrated good cycling performance up to 100 cycles at a high rate of 5 A/g. The unique morphology and the high quality single crystalline structure of $LiMn_2O_4$ nanowires effectively reduced lithium ion diffusion length and improved the electronic transport, demonstrating large capacities at higher cycling rates.

Besides the nanowire structure, $LiMn_2O_4$ nanorods were also synthesized via chemical conversion of single-crystalline β-MnO_2 nanorods using a simple solid-state reaction [146]. The $LiMn_2O_4$ nanorods with an average diameter of 130 nm and length of 1.2 μm exhibited high charge storage capacity (~148 mAh/g) at high rates compared to commercially available bulk particles (~50 mAh/g), indicating that large surface-to-volume ratio of the nanorods can significantly enhance the kinetics of the $LiMn_2O_4$ electrodes. It also showed very good capacity retention, more than 85% after 100 cycles.

In comparison with the bulk phase, $LiMn_2O_4$ nanoparticles showed improved capacity and cycling stability in the 3 V discharge range [153]. However, due to high surface area of nanoparticles, the dissolution of manganese from the spinel lattice into the electrolyte was observed, leading to severe capacity fading during cycling, particularly at elevated temperatures. To solve this problem, Bruce's group synthesized an ordered mesoporous $Li_{1.12}Mn_{1.88}O_4$ spinel with a modified composition of manganese and compared it to corresponding bulk particles with the same composition [147]. They demonstrated that nanostructured $Li_{1.12}Mn_{1.88}O_4$ exhibited 50% higher specific capacity at a high rate of 30 C at room temperature. Furthermore, the nanostructured $Li_{1.12}Mn_{1.88}O_4$ materials exhibited improved capacity retention compared to the bulk spinel.

Bruce's group also synthesized mesoporous β-MnO_2 having a porous structure and highly crystalline walls as cathode materials [154]. While bulk β-MnO_2 particles led to unfavorable electrochemical performance, mesoporous β-MnO_2 offered a significantly high lithium intercalation capacity of 284 mAh/g with a composition of $Li_{0.92}MnO_2$. Fig. 21 shows typical TEM images of mesoporous β-MnO_2, clearly demonstrating the highly ordered pore structure with a wall thickness of 7.5 nm. Both the β-MnO_2 crystal structure and the mesoporous structure were preserved upon cycling. The unique structure of mesoporous β-MnO_2 allowed volume changes during lithium intercalation/deintercalation, and 81% capacity was retained after 50 cycles.

$LiMn_2O_4$ nanotubes were also derived from thermal decomposition of sol–gel precursors using porous anodic aluminum oxides

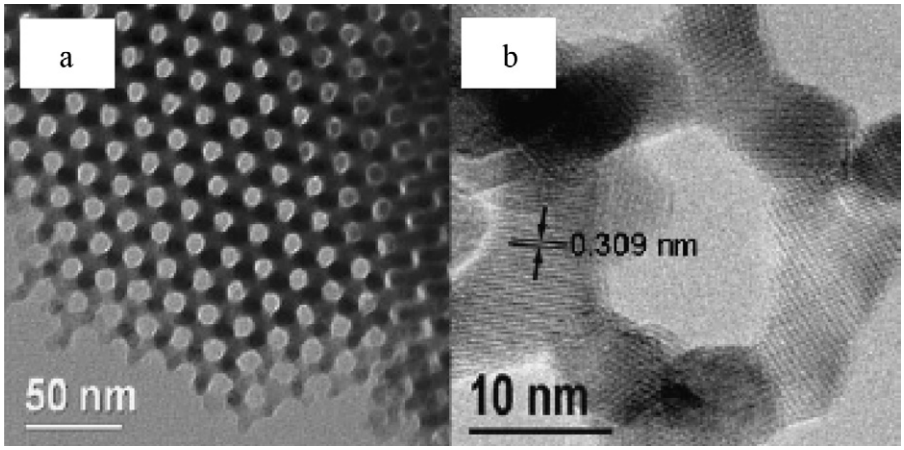

Fig. 21. (a) TEM image of mesoporous β-MnO_2. (b) High-resolution TEM image of mesoporous β-MnO_2 [154]. Copyright Wiley-VCH Verlag GmbH & Co. KGaA. Reproduced with permission.

as templates [143]. The as-synthesized nanotubes were open-ended with uniform shape and size. It was reported that the nanotube-based electrodes showed better reversibility, larger capacity, and higher rate capability than those based on nanocrystalline counterparts. The enhanced electrochemical performance of nanotube-based electrodes was attributed to their relatively high specific surface areas of the hollow tubular structure and much shorter Li^+ diffusion lengths through the thin tube walls (20–30 nm), which are much smaller than the diameters of the commercial or nanocrystalline powders.

Similarly, $LiCoO_2$ and $LiNi_{0.8}Co_{0.2}O_2$ nanotubes were also synthesized and reported to show good promise as cathode materials for lithium-ion batteries [143]. It was claimed that intercalation/deintercalation of Li^+ could be more efficiently accomplished with nanotubes than other nanocrystalline structures or morphologies.

Polyanion-based compounds: One major drawback of Co and Ni-based cathode materials is the chemical instability at deep charge and the associated safety problems. As previously mentioned, concerns over safety and cost have prompted research into new electrode materials. Oxide compounds that contain the polyanion $(XO_4)^{y-}$ (X = S, P, As, Mo, W) have been explored as lithium insertion/extraction hosts since the late 1980s [136]. An inductive effect from $(PO_4)^{3-}$ and $(SO_4)^{2-}$ enhances redox energies compared to those in oxides and stabilizes the structure [155].

One fascinating example, $LiFePO_4$ has an olivine structure and offers a flat discharge profile around 3.4 V with a theoretical capacity of 170 mAh/g. The major drawback of $LiFePO_4$, however, is poor lithium ion conductivity and poor electronic conductivity. When the particle size is reduced, the lithium ion diffusion length in the olivine structure can be effectively reduced [155].

Manthiram's group recently developed a novel microwave assisted solvothermal (MW-ST) process to obtain olivine $LiMPO_4$ (M = Mn, Fe, Co, Ni) with nanorod morphologies within a short reaction time of 5–15 min at 300 °C [152,156]. A reaction of the metal acetates with H_3PO_4 and LiOH under MW-ST conditions produces highly crystalline $LiMPO_4$ nanorods. SEM and TEM images of the $LiFePO_4$ nanorods with controlled particle size are shown in Fig. 22. These morphologies are particularly attractive to achieve fast lithium diffusion and high rate capability. $LiMnPO_4$, $LiCoPO_4$, and $LiNiPO_4$ exhibit higher voltages (4.1, 4.8, and 5.2 V versus Li/Li^+, respectively), which are helpful to increase the energy density. However, the very low electronic conductivity and the Jahn-Teller distortion associated with $LiMnPO_4$ result in poor electrochemical performance. In the cases of $LiCoPO_4$ and $LiNiPO_4$ electrode materials, there are few stable electrolytes that can operate at high voltage. Although $LiFePO_4$ exhibits lower discharge voltage (3.4 V versus Li/Li^+), it is still attractive for both high energy density and power application.

4.2.1.2. Unique shape/morphology. Wu et al. synthesized nanostructured VOOH hollow dandelions by employing a simple hydrothermal process to organize as-synthesized flakes into VOOH hollow-curved architecture via an aggregation-then-growth process (Fig. 23) [148]. The hollow-dandelion electrode retained 120.6 mAh/g at 100 mA/g, corresponding to about 86.7% of the electrode capacity at 20 mA/g. In the case of microparticle electrode material, it exhibits 79.2 mAh/g, corresponding to about 77.7% of the electrode capacity at 20 mA/g. The hollow VOOH electrode materials showed improved high-rate discharge ability due to the reduced diffusion length compared to microparticles and, furthermore, exhibited a high-power output even at low temperatures (−15 to 0 °C). Similarly, V_2O_5 hollow microspheres [157] and nanorolls [158] have also exhibited improved electrochemical performance compared to bulk counterparts.

4.2.2. Nanocomposites of cathode materials

Most cathode materials with good electrochemical properties have low electronic conductivity ranging from 10^{-9} S/cm to 10^{-3} S/cm, as seen for $LiCoO_2$ and $LiFePO_4$ [14]. To enhance the electronic conductivity and hence the electrochemical kinetics, cathode materials are often embedded within a highly conducting network, like carbon or metal. Such a composite structure has been effective in enhancing electronic conductivity and performance. In particular, carbon-based composites have been the most effective approach.

Transition metal oxides: Dunn's group combined V_2O_5 aerogels with single-wall CNTs using a sol–gel method, in which V_2O_5 nanoribbons were well mixed with CNTs due to their similar morphology and similar dimensions [159]. The porous CNT structure and V_2O_5 aerogel also allow better accessibility of electrolyte. As a result, such nanocomposites showed high capacities (more than 400 mAh/g) at high rates. Similarly, composite electrodes of V_2O_5 sol and carbon prepared from surfactant were also reported to have good electrochemical performance at a high discharge rate (30 A/g) [160].

A composite consisting of metal and cathode materials is another strategy to achieve good electrochemical performance. Takahashi et al. prepared Ni–$V_2O_5{\cdot}nH_2O$ core–shell nanocable structures by a template-based electrochemical deposition [161]. When compared with single-crystalline V_2O_5, and V_2O_5 film from sol–gel process, Ni–$V_2O_5{\cdot}nH_2O$ core–shell nanocables arrays

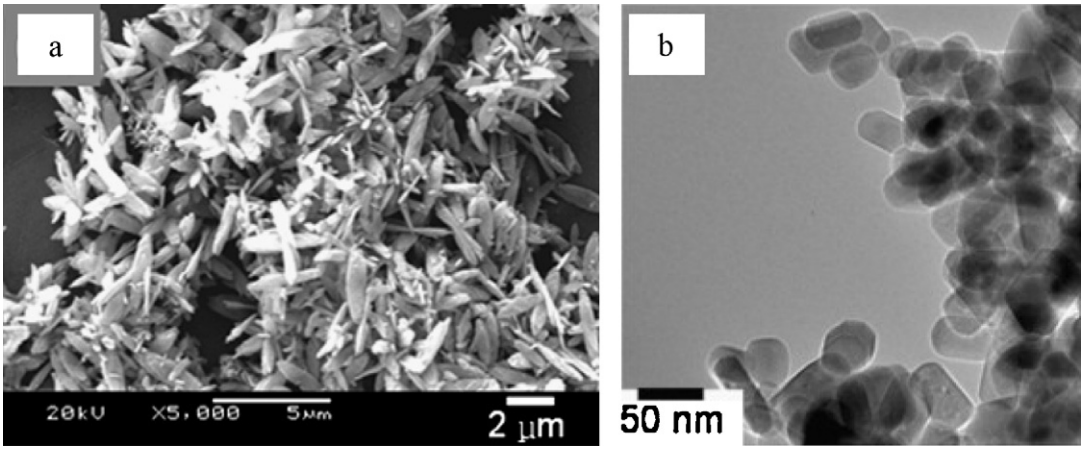

Fig. 22. (a) SEM and (b) TEM images of $LiFePO_4$ nanorods prepared by the microwave assisted solvothermal process method within 5–15 min at 300 °C [152]. Copyright 2008, with permission from Elsevier.

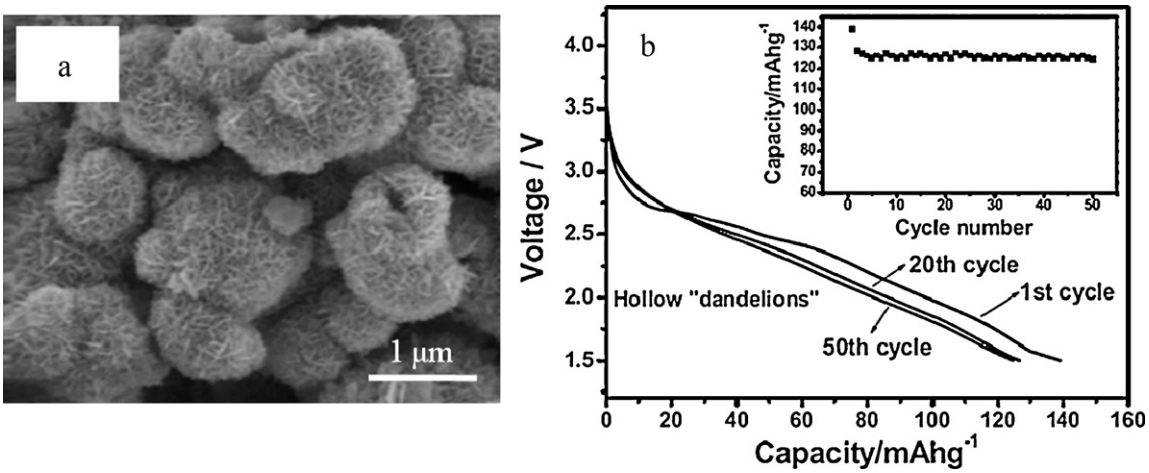

Fig. 23. (a) SEM image of VOOH hollow-dandelions. (b) Voltage versus discharge capacity curves for VOOH hollow-dandelion electrodes cycled between 3.6 and 1.5 V. The inset shows excellent cycling performance [148].

showed significantly improved capacity and rate capability due to the enhanced surface area and the reduced internal resistance. The core–shell arrays have remarkably higher energy and power density than those of single-crystalline V_2O_5 and sol–gel film by at least one order of magnitude.

Ag–$Ag_{0.08}$ $V_2O_5{\cdot}nH_2O$ [162], Ag–$LiCoO_2$ [163], and Ag–$Li[Ni_{1/3}Co_{1/3}Mn_{1/3}]O_2$ [164] composites were also reported. The Ag phase not only enhances electrical conductivity but also protects the SEI layers. In case of Ag–$LiMn_2O_4$ composite system, Ag improved the cycling stability and high-rate discharge capacity of the $LiMn_2O_4$ electrode [165]. Composite materials of transition metal oxide and conductive polymer (like polyacetylene, polyaniline, and polypyrrole) have also been studied over the past two decades. Conductive polymers enhance electrochemical performance by increasing the number of electrochemically active sites and aiding lithium diffusion [166–168].

Polyanion-based compounds: The composite of $LiFePO_4$ and multi-walled CNTs were prepared by a combination of hydrothermal process, ball-milling, and heating reaction by Jin et al. [149]. The electronic conductivity significantly improved from 10^{-9} S/cm for the pure $LiFePO_4$ particles to 1.08×10^{-1} S/cm for the composite. As another example, the relatively unexplored $Li_3V_2(PO_4)_3$ exhibited relatively high operating voltage (4.0 V) and capacity (197 mAh/g) [169]. This material, however, also has low electronic conductivity (similar to $LiFePO_4$). To overcome this problem, $Li_3V_2(PO_4)_3$ were embedded in a conductive carbon to form the nanocomposite, which exhibits 95% theoretical capacity at a high rate of 5 C.

4.2.3. Surface modification of cathode materials

Transition metal oxides: Carbon coating has been widely used because of its convenience and simplicity of preparation. Various methods have been developed including a thermal decomposition of pyrene [170], a hydrothermal decomposition of ascorbic acid [171], a mechanical activation of acetylene black [172], and a spray pyrolysis [173]. For example, carbon coated $LiCoO_2$ showed increased structural stability and electrical conductivity [174]. Especially, nano-sized carbon coating on $LiCoO_2$ from sucrose showed a higher capacity than pristine $LiCoO_2$ due to the reduced charge transfer resistance and faster lithium ion diffusion.

In addition to carbon coating, various metal phosphate coatings have been studied. For example, Kim et al. investigated the effect of the metal phosphate coatings on $LiCoO_2$ cathode material [175]. The $LiCoO_2$ completely coated by $AlPO_4$ or $FePO_4$ exhibited the highest intercalation capacity (~230 mAh/g) in a voltage range of 4.8 and 3 V at a rate of 0.1 C. The improvement in the electrochemical properties of the metal phosphate coated cathode materials is attributed to the suppression of cobalt dissolution and the non-uniform distribution of local strain by the coating material.

Further, metal oxides coating such as ZrO_2 [176], Al_2O_3 [177], SnO_2 [178], MgO [179], ZnO [180], or $3LaAlO_3{:}Al_2O_3$ [181] on $LiCoO_2$ have also been widely investigated. In a similar manner, metal oxide coating on $LiMn_2O_4$ improved its cycling performance. The electrochemical characteristics of nano-sized ZnO-coated $LiMn_2O_4$ was investigated at 55 °C [182]. After 50 cycles, the coated $LiMn_2O_4$ exhibited capacity retention of 97%, higher than that of the pristine $LiMn_2O_4$ electrode material. ZnO coating mainly collects HF from the electrolyte and thus decreases the Mn dissolution in the electrolyte; consequently, it reduces interfacial resistance. For a similar reason, ZnO coating on $Li_{1.05}Al_{0.1}Mn_{1.85}O_{3.95}F_{0.05}$ cathode materials significantly improved cycling performance (98.5% capacity retention after 50 cycles) of the cathode at 55 °C [183]. The $Li_4Ti_5O_{12}$ coated $LiMn_2O_4$ cathode electrode materials showed the improved electrochemical performance, because $Li_4Ti_5O_{12}$ has a high chemical diffusion coefficient (10^{-6} cm^2/s) [184] and the same spinel structure and zero-strain property as $LiMn_2O_4$. Also, since $Li_4Ti_5O_{12}$ thin layer is inactive to the electrolyte and there is no volume expansion during cycling, the decomposition of $LiMn_2O_4$ is blocked, and the cycling stability is significantly enhanced [185].

Polyanion-based compounds: Wang et al. synthesized a $LiFePO_4$/carbon composite consisting of a highly crystalline $LiFePO_4$ core (20–40 nm in size) and a highly graphitic carbon shell (1–2 in thickness) via *in situ* polymerization [150]. As shown in Fig. 24, the complete coating of carbon layer ensures that electrons pass through the surface of each $LiFePO_4$ particle, effectively shortening the path length for electronic transport. Moreover, lithium ions can easily intercalate into the $LiFePO_4$ through the graphitic carbon coating layer. As-prepared $LiFePO_4$/carbon composite exhibits a high rate performance. The discharge capacity is 168 mAh/g at a rate of 0.6 C and 90 mAh/g at a very high rate of 60 C.

ZnO-coated $LiFePO_4$ shows better cycling performance than pristine $LiFePO_4$, because the ZnO coating layer improves the chemical stability of $LiFePO_4$ by blocking the iron dissolution. In a similar process, Rho et al. reported improved rate capability and cycling performance by coating Fe_2P on the surface of $LiFePO_4$ [186]. This cathode material exhibited a high capacity of 105 mAh/g at a very high rate of 14.8 C.

Another strategy to improve electrode performance is to combine carbon coating and electronically conducting oxides such

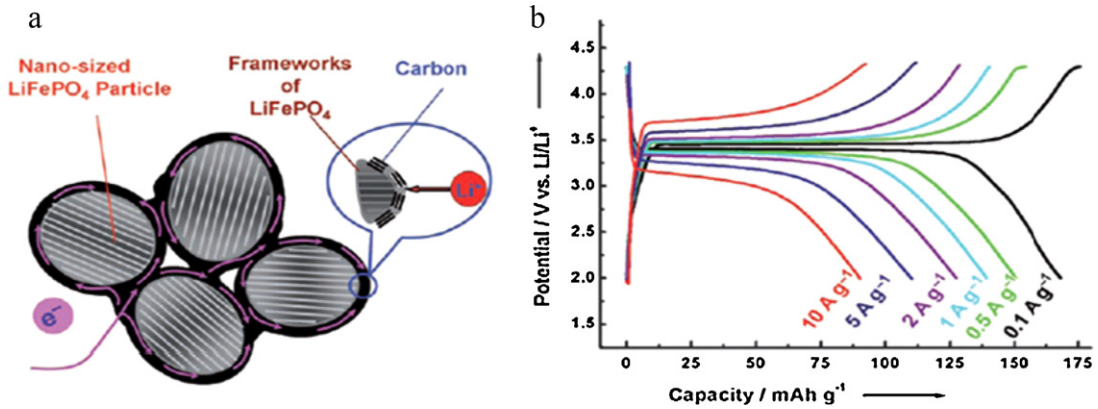

Fig. 24. (a) Schematic illustration of proposed structure for $LiFePO_4$ particles with nanoscale carbon coating. (b) Charge–discharge curves of $LiFePO_4$/carbon composite cycled in the potential range of 2.0–4.3 V (vs. Li/Li^+) at different current densities [150].

as RuO_2 with $LiFePO_4$ [187]. RuO_2 with a particle size of ~5 nm, prepared by cryogenic decomposition of RuO_4 at low temperature, can be deposited on a carbon-coated $LiFePO_4$. During RuO_2 deposition, the original morphology was maintained and in good contact with carbon layer. Co-existing carbon and RuO_2 layers improve the kinetics and rate capability of the composite. Carbon-coated $LiFePO_4$ electrode deteriorates the performance at a high rate, while carbon-$LiFePO_4$/RuO_2 showed improved electrochemical performance at high rates.

Manthiram's group have encapsulated $LiFePO_4$ nanorods prepared by the MW-ST process within a mixed ionic-electronic conducting p-toluene sulfonic acid (p-TSA) doped poly(3,4-ethylenedioxy thiophene) (PEDOT) [152]. Fig. 25 shows TEM images of highly crystalline $LiFePO_4$ (dark region) wrapped with transparent polymer (light regions). The composite nanorod sample exhibits high capacity (166 mAh/g) and excellent cycling performance after coating due to the enhancement in electronic conductivity and the additional effect provided by ion-conducting doped PEDOT.

4.2.4. Nano-architectured cathode electrodes

Recently, Ajayan's group fabricated hybrid coaxial nanotubes of MnO_2 and carbon nanotubes (CNTs) for high performance electrodes in lithium batteries [188]. These coaxial nanotube structures were prepared by a combination of simple vacuum infiltration and chemical vapor deposition techniques through an anodic aluminum oxide (AAO) template approach (Fig. 26). High reversible capacity was observed for MnO_2/CNT hybrid coaxial nanotubes compared to MnO_2 nanotubes. This result indicates the reduced structural changes during cycling. Voltage versus specific capacity curves were obtained by cycling the cell at a constant rate of 50 mA/g between 3.2 and 0.02 V (versus Li/Li^+). The first discharge capacity of 2170 mAh/g and a reversible capacity of ~500 mAh/g after 15 cycles were observed for MnO_2/CNT hybrid coaxial nanotubes. The nano-sized and porous structure of the MnO_2 allows fast ion diffusion, while the CNT facilitates electron transport to the MnO_2. In addition, CNTs act as additional lithium storage sites, which lead to an improved reversible capacity.

4.3. Summary

While $LiCoO_2$ is still widely used as the cathode material in current Li-ion batteries, its stability at deep charge limits the practical capacity to only about half of its theoretical capacity. $LiNiO_2$ has higher energy density, but the stability is even more susceptible. Nanoscale surface modification of $LiCoO_2$ has been investigated to improve stability and to allow its use at higher voltages, but $LiCoO_2$ still appears not to be appropriate for electric vehicle applications because of the relatively low rate capability and high cost.

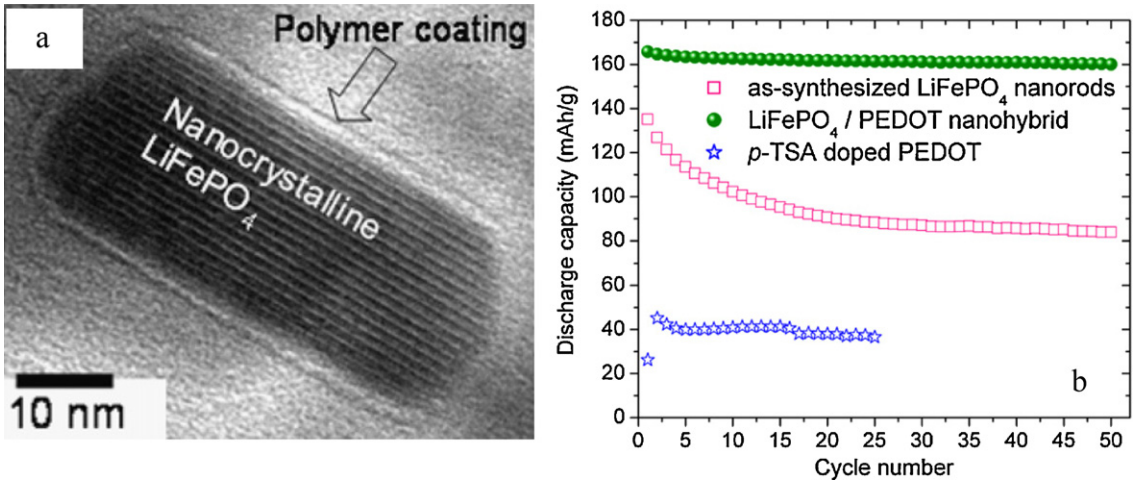

Fig. 25. (a) High resolution TEM image of $LiFePO_4$ nanorod with thin p-TSA doped PEDOT coating. (b) Cycling performance of $LiFePO_4$, p-TSA doped PEDOT, and $LiFePO_4$ nanorods with p-TSA doped PEDOT coating [152].

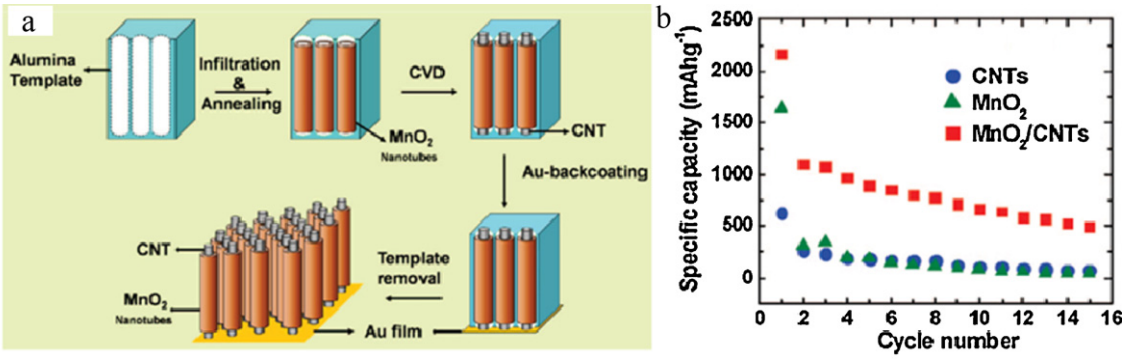

Fig. 26. (a) Schematic illustration showing the fabrication of MnO_2/CNT hybrid coaxial nanotube arrays inside AAO template using a simple vacuum infiltration and chemical vapor deposition techniques. (b) Cycling performance of MnO_2/CNT coaxial nanotube arrays, MnO_2 nanotubes, and carbon nanotubes.
Reprinted with permission from [188]. Copyright 2009 American Chemical Society.

Spinel $LiMn_2O_4$ and its substituted derivatives have gained much attention as alternatives to $LiCoO_2$ in Li-ion batteries for electric vehicle applications because they are less expensive and environmentally benign. A thin-film oxide coating on $LiMn_2O_4$ and doping of metal ions into $LiMn_2O_4$ (e.g., $Li_{1.1}Mn_{1.9}Al_{0.1}O_4$) effectively suppresses Mn dissolution and improves cycling stability at elevated temperatures.

Because of the concerns about safety and high cost of $LiCoO_2$, polyanion-based compounds have recently gained significant attention. Iron-containing metal phosphates and sulfates have been widely studied as promising cathode materials of high rate capability and long cycling life. In particular, olivine $LiFePO_4$ has emerged as an attractive alternative cathode material since it offers good energy density and environmental friendliness at low cost. In addition, the improved chemical stability of the Fe^{2+}/Fe^{3+} redox couple, combined with the covalently bonded PO_4 groups, could prevent dissolution issues. However, bulk $LiFePO_4$ has poor kinetic for lithium insertion/extraction due to its poor electronic conductivity. Reducing the particle size of $LiFePO_4$ to a nanometer scale (below 30 nm) could help overcome the poor lithium ion transport that is associated with the two-phase ($LiFePO_4$/$FePO_4$) boundary with a miscibility gap, improving capacity and capacity retention upon cycling.

A thin-film carbon coating on $LiFePO_4$ is proven to be effective in enhancing its electronic conductivity and enabling high rate capability and excellent cycling performance. A surface modification of $LiFePO_4$ with a thin-film mixed ionic–electronic conducting polymers also showed promise by improving the electronic and lithium ion conduction.

4.4. Remaining challenges

We have learned how nanostructured cathode materials have been developed and how they have significantly improved the performance of lithium ion batteries. However, some new challenges still remain. For example, a large surface area can increase the solubility of electrode materials in the electrolyte solution; this is a serious side effect of the increased chemical activities. $LiCoO_2$, $LiNiO_2$ and $LiMn_2O_4$ all have dissolution issues, so it is necessary to coat them with a thin film (a few nanometers thick) of various materials (e.g., carbon, metal oxides, and phosphates) in order to suppress metal dissolution and increase the electronic conductivity of active electrode materials. With a nanoscale coating, cathode materials can avoid direct contact with electrolytes, thus improving structural stability and increasing the lifetime of Li-ion batteries. Other remaining challenges associated with current cathode materials are briefly summarized as follows.

(1) The high reactivity of the redox couples Co^{3+}/Co^{4+} and Ni^{3+}/Ni^{4+} with the electrolyte prohibits the use of the advantageous nanostructured forms of layered $LiCoO_2$ and $LiNiO_2$ in practical batteries.
(2) The dissolution of manganese ions during the charge/discharge process must be further minimized.
(3) The rate-capability (power density) of current cathode materials should be further improved. For example, the time required for charging is still unsatisfactory for electric vehicle and hybrid electric vehicle applications.
(4) Although unique nanostructured cathodes (e.g., $LiMn_2O_4$ nanorods) performed better than bulk counterparts, fundamental understanding of the mechanism of enhancement is still lacking and it is still not clear how to rationally design better cathode materials.
(5) Although nanoscale surface modifications and coatings effectively suppressed the dissolution issues, full understanding on the details of surface/interface reactions requires more systematic *in situ* studies.
(6) Most importantly, the obtainable energy densities of the current cathode materials remain insufficient to meet the ever-increasing requirements of the rapidly progressing emerging technologies.

4.5. Opportunities and new directions

While Li-ion batteries still represent the state-of-the-art among all existing batteries, it is unlikely that they will be able to meet the increasing demands of emerging technologies, primarily limited by the energy densities of the existing cathode materials.

Since energy density increases with the square of cell voltage ($E = 1/2CV^2$), one effective way to improve energy density is to use cathode materials of high discharge voltage. Many phosphates (e.g., $LiNiPO_4$ and $LiCoPO_4$) have shown promise as high-voltage cathode materials. However, new electrolytes of wider potential ranges should be developed in order to realize the potential of these promising cathodes in practical cells. Ionic liquids are expected to play an important role in these high-voltage battery systems.

Creating desired interface/surface of nanostructured electrodes is essential to effective enhancement of charge and mass transfer processes and to achieving high energy and power densities. However, fundamental understanding of the surface and interfacial processes that accompany the charge–discharge operation of a battery is still lacking. Better insights into the electrochemical reactions and the roles of point defects in the nanoscale regime are required in order to achieve rational design of more effective

surface modifications (or coatings) for high capacity and rate capability. Novel architectures deserve more attention because the same materials/compositions with different geometry can display dramatically different behavior.

Most importantly, successful explorations of new materials and chemistries are needed to go beyond incremental improvements in energy densities of existing materials. Recently, new materials (e.g., nanostructured sulfur and mesoporous carbon [38]) have emerged as promising cathode materials. A lithium–sulfur battery has theoretical specific energy and energy density of 2500 Wh/kg and 2800 Wh/L, respectively, which are far greater than those of conventional lithium-ion batteries. Transforming the potential of these novel materials and chemistries into a reality remains a grand challenge. Another promising candidate for dramatic improvement in energy density, O_2-breathing electrodes, is discussed in the next section.

5. O_2-breathing cathodes for Li-air batteries

Li-air batteries are receiving wide attentions for applications in electric vehicles and many other advanced electronic devices due to their high theoretical energy density, which is reported to be comparable with that of gasoline [7,8,189]. The theoretical specific energy density of a Li-air battery is often quoted to be over 5000 Wh/kg for LiOH formation and 11,000 Wh/kg for Li_2O_2 formation [8,190], as estimated from the difference in Gibbs free energy of the products and the reactants of the battery reactions using thermodynamic data without including the mass of O_2. These energy densities are comparable to that of a fuel cell and much higher than that of a current Li-ion battery (~150–200 Wh/kg_{cell}) [5,8,9]. To make a fair comparison with the specific cathode capacities and energy densities of Li-ion batteries, however, the capacity and energy density for a Li-air battery should be normalized by the lithiated cathode mass (i.e., including O_2 mass or Li_2O_x). Recently, Lu et al. showed that Li-air batteries (non-aqueous type) can have more than 5 times higher cathode capacities and 4 times higher energy density than those of a state-of-the-art Li-ion battery utilizing $LiCoO_2$ as the cathode [10]. They assumed carbon packing density of 0.36 g/cm^3 with about 15% carbon volume fraction, 25% electrolyte volume fraction, and complete filling of the remaining 60% volume fraction with Li_2O_x electrode material. These assumptions are reasonable since capacities (thus energy densities) of a Li-air battery can be limited by the pore volume and the porosity of the electrodes, which provide the space for solid Li_2O_x products and effective O_2 diffusion. Under these assumptions, the energy density of a Li-air battery (non-aqueous type) is ~1000 Wh/kg_{cell}, which is still significantly larger than those of current Li-ion batteries (150–200 Wh/kg_{cell}). It is also possible to develop a power device that can couple a lithium metal together with dissolved oxygen in seawater for submarine applications.

5.1. Different cell configurations and electrode reactions

To date, four different architectures of Li-air batteries have been investigated [8], depending on the types of electrolytes used, as schematically shown in Fig. 27. In addition to the all-solid-state system with a solid electrolyte, other three cell configurations involve liquid electrolytes: an aqueous electrolyte throughout the system, a non-aqueous organic electrolyte throughout the system, and a mixed system with an aqueous electrolyte in the air electrode compartment and a non-aqueous organic electrolyte in the lithium-electrode compartment. In the last case, a stable solid electrolyte membrane must be used to physically separate the aqueous electrolyte on one side from the non-aqueous electrolyte on the other side.

Lithium metal is often used as the negative electrode (or anode) in Li-air batteries for high energy density; however, lithium-

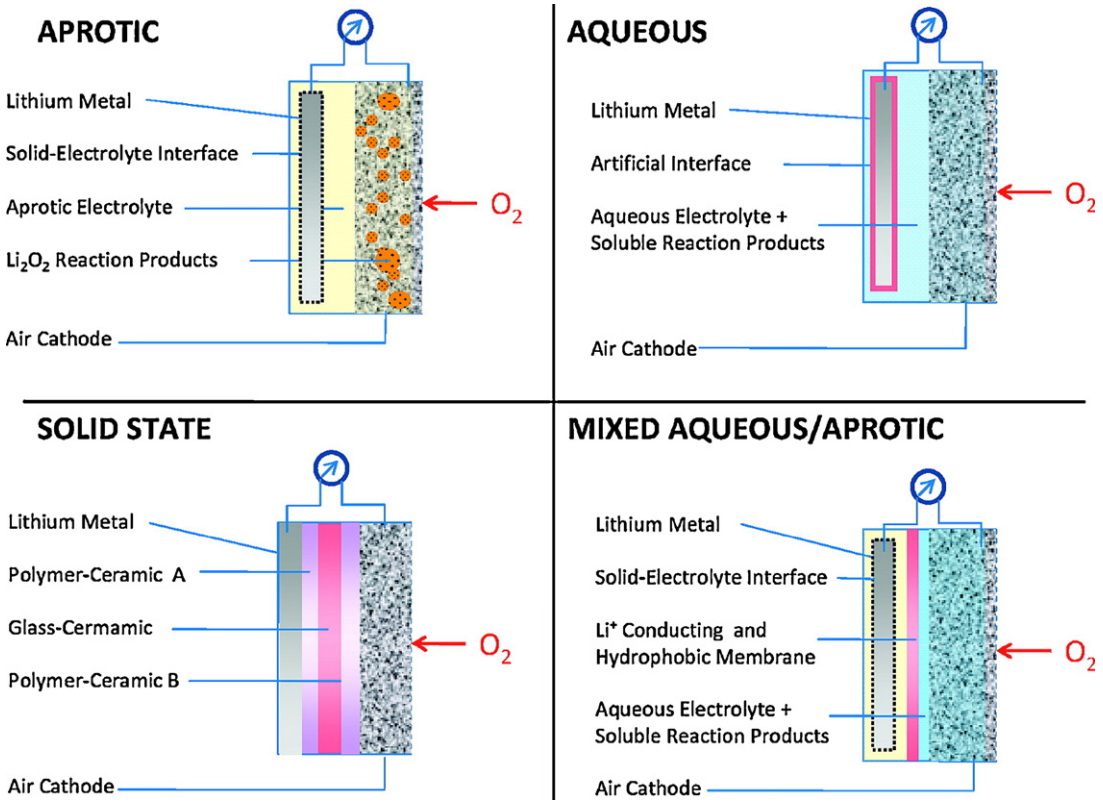

Fig. 27. Four different configurations of Li-air batteries based on the types of electrolytes.
Reprinted with permission from [8]. Copyright 2010 American Chemical Society.

containing anodes (negative electrode) developed for Li-ion batteries (e.g., $Li_4Ti_5O_{12}$ and Li alloys) can be used for better safety and reliability. Thus, lithiated nanostructured negative electrodes discussed in Section 3 for Li-ion batteries are applicable to Li-air batteries as well.

The positive electrode for Li-air battery, however, is very different from those for Li-ion batteries as discussed in Section 4, since the electrode reactions are quite different. Further, the oxygen reduction reaction (ORR) and oxygen evolution reaction (OER) at the air-breathing positive electrode in a Li-air battery depends also on the electrolyte used.

In a non-aqueous organic (or aprotic) electrolyte, the electrochemical reaction can be described as

$$2Li + O_2 \underset{\text{Charge}}{\overset{\text{Discharge}}{\rightleftharpoons}} Li_2O_2 \quad E^\circ = 2.96\,V \text{ vs. } Li/Li^+ \text{(for } Li_2O_2 \text{ formation)}$$

when Li_2O_2 is formed at the cathode during discharge, and as

$$4Li + O_2 \underset{\text{Charge}}{\overset{\text{Discharge}}{\rightleftharpoons}} 2Li_2O \quad E^\circ = 2.91\,V \text{ vs. } Li/Li^+ \text{(for } Li_2O_2 \text{ formation)}$$

when Li_2O is formed at the cathode, which is also reported under certain conditions [191–193]. The reaction for all-solid Li-air batteries should be the same as those for the one based on non-aqueous electrolyte.

In an aqueous electrolyte, the electrochemical reaction and the corresponding cell voltage depend on the pH of the aqueous electrolyte in the air electrode compartment as follows.

$$4Li + O_2 + 2H_2O \underset{\text{Charge}}{\overset{\text{Discharge}}{\rightleftharpoons}} 4LiOH$$

$$E^\circ = 3.45\,V \text{ vs. } Li/Li^+ \text{(Alkaline media)}$$

$$4Li + O_2 + 4H^+ \underset{\text{Charge}}{\overset{\text{Discharge}}{\rightleftharpoons}} 4Li^+ + 2H_2O$$

$$E^\circ = 4.27\,V \text{ vs. } Li/Li^+ \text{(Acidic media)}$$

In the sections below, we will discuss how nanostructures influence the functioning of an air-breathing positive electrode. In addition, concerns associated with O_2-breathing cathodes in a non-aqueous electrolyte and in an aqueous electrolyte will be discussed. Opportunities and new directions will also be highlighted.

5.2. Electrodes in a non-aqueous electrolyte

In a non-aqueous organic (or aprotic) electrolyte, the reversible oxygen electrode reactions can be described as,

$$2Li^+ + O_2 + 2e' \underset{\text{Charge}}{\overset{\text{Discharge}}{\rightleftharpoons}} Li_2O_2 \quad \text{or}$$

$$O_2 + 2e' \underset{\text{Charge}}{\overset{\text{Discharge}}{\rightleftharpoons}} O_2^{2-} \quad \text{(for } Li_2O_2 \text{ formation)}$$

$$4Li^+ + O_2 + 4e' \underset{\text{Charge}}{\overset{\text{Discharge}}{\rightleftharpoons}} 2Li_2O \quad \text{or}$$

$$O_2 + 4e' \underset{\text{Charge}}{\overset{\text{Discharge}}{\rightleftharpoons}} 2O^{2-} \quad \text{(for } Li_2O_2 \text{ formation)}$$

To facilitate these electrode reactions and accommodate the solid products, porous carbon with high surface area (e.g., Super P from TIMCAL Graphite & Carbon) is used as the positive electrode. To enhance the electrode kinetics, improve the cyclability, and reduce the energy loss associated with the discharge–charge overpotentials, nanostructured catalysts (e.g., Au nanoparticles or α-MnO_2 nanowires) are often introduced to the electrodes. It is believed that both porous carbon and catalysts are important to achieve high energy and power density with reasonable life time, as discussed in detail in the following sections. The solubility and transport properties (including diffusion coefficient and electrolyte viscosity) of O_2 in the electrolyte can also significantly influence the discharge capacity and rate capability of Li-air batteries. For instance, Read et al. reported an increase in discharge capacity with the increase in O_2 concentration [194]. Also, by decreasing electrolyte viscosity, they found an increase in discharge capacity. It implies the importance of optimization of electrolyte for high-performance Li-air batteries. For more detailed data (O_2 solubility, viscosity, and conductivity of different organic electrolytes), readers are referred to the work of Read et al. [194] and the relevant references cited.

5.2.1. Porous carbon-based electrodes

Since pore volumes are gradually filled with insoluble products (i.e., Li_2O_2) during the course of discharge, the reactions will cease when all possible spaces are used up. Therefore, highly porous carbons with large pore volume are being investigated as electrodes to achieve high energy density. In practice, however, the demonstrated energy density of Li-air batteries to date is much lower than the theoretical value. This is mainly because the discharge reaction is finished well before all pores are filled with solid products. It was suspected that the formation of the insulating products on the carbon surface greatly increases the resistance for the reactants (oxygen, electron, and Li^+) to transport to the active sites, leading to the termination of discharge reactions, although more pore volume still remains unfilled. Indeed, experimental results show that pores of air electrodes are far from being fully loaded with lithium oxides at the end of discharge [191,195].

There have been many experimental and computational studies directed at understanding the relationship between the physical parameters of carbons (surface area, pore size, distribution, connectivity, etc.) and the capacity of Li-air batteries. However, it is very difficult to determine the most important factor affecting the cell performance. Indeed, there are some conflicting reports on the effect of carbon surface area. Hayashi et al. reported a proportional relationship between surface area and discharge capacities [196], while Yang et al. demonstrated that there is no proportional relationship between the surface area of commercial carbons and discharge capacity and claimed that pore size should be considered together with surface area [193]. They synthesized mesocellular carbons having large pore volume and mesoporous structures and demonstrated high capacity (2500 mAh/g), about 40% higher than commercial carbon black, Super P. It was also reported that larger numbers of mesopores led to larger capacities.

Shown in Fig. 28, Tran et al. reported a near-linear relationship between discharge capacity and average pore diameter of carbon [197]. In this study, authors claimed that carbons with large pores should be selected to ensure effective three phase (oxygen, electron, and Li^+) boundaries. Mirzaeian and Hall also reported a combined effect of pore volume, size and surface area of carbon on the discharge capacity [198]. Using porosity-controlled carbon aerogels as electrodes, they showed carbons with larger pore volume and diameter displayed higher discharge capacity.

However, we believe that a more important factor in achieving high performance is the ability to make effective use of pores, not

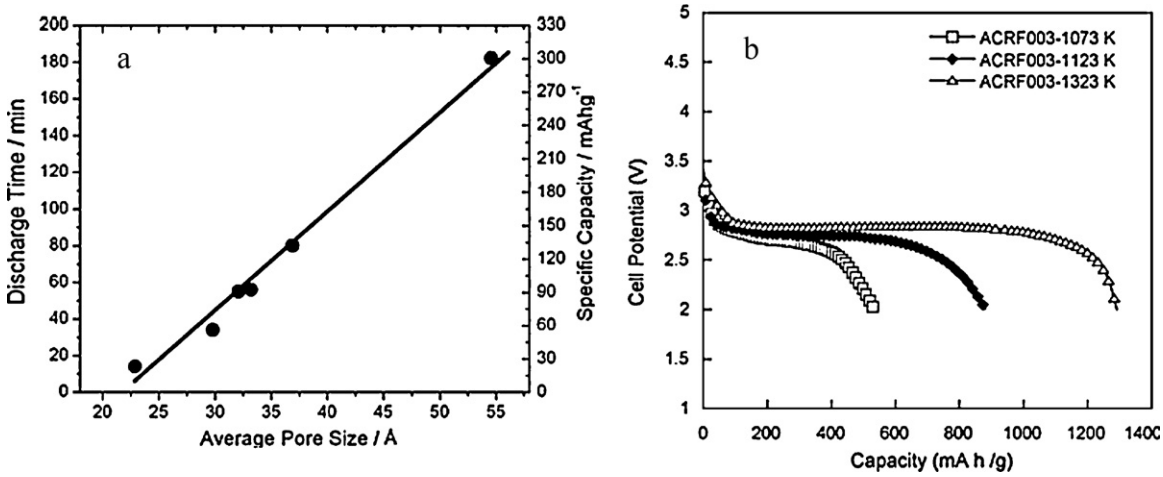

Fig. 28. (a) Discharge time and specific capacitance of gas diffusion electrodes as a function of pore size [197]. (b) Discharge capacities of air electrodes made with carbon aerogels showing larger pore volume led to higher capacity [198].
(a) Copyright 2010, with permission from Elsevier. (b) Copyright 2009, with permission from Elsevier.

the size or total volume of pores. Therefore, strong efforts should be directed at optimizing the pore structure of carbons to accommodate a large amount of lithium oxides without hindering the transport of reactants (i.e., oxygen, electron, and Li^+) to active sites. Based on numerical simulations, it was suggested that a well-interconnected dual pore system (layered or well-mixed configuration of a catalyzed and non-catalyzed carbon) would ensure effective transport of oxygen into the inner regions of the air electrode throughout the discharge process, thus accommodating more solid products without clogging the pores [199].

In addition to the microstructure optimization of porous carbon, the architecture and overall dimension of cathodes may also influence the performance. Zhang et al. examined single-wall carbon nanotube (SWNT) and carbon nanofiber (CNF) composite as air electrodes, demonstrating that the discharge capacity decreases with the thickness of the air electrode [195], as shown in Fig. 29. A discharge capacity of ~2500 mAh/g was achieved with a thin (~20 μm) air electrode, but it dropped down to only ~400 mAh/g when a thicker electrode (~220 μm) was used. The SEM images showed that discharge product was deposited mostly near the air side, while large pore volumes still remain unfilled near the electrolyte. Based on this observation, it was suggested that functionally graded-porous electrode structures (with large pores outside) may improve the capacity of Li-air batteries. A similar observation was reported in literature where gravimetric capacity (mAh/g) decreased with the amount of carbon loading [200].

It was also suggested that the limitation of electron transport through insulating Li_2O_2 deposits is another important factor affecting capacity [201]. As Li_2O_2 and Li_2O are both insulators, the formation of a dense layer will significantly increase the resistance to electron transport across the layer, dramatically increasing electrode polarization, as confirmed by electrochemical impedance spectroscopy [195]. Therefore, minimizing difficulties associated with electron transport during the growth of the insulating layer is very important. It should be noted that Li_2O_2 formation on the surface of the insulating Li_2O_2 deposit will be quite different from that on the surface of carbon.

Therefore, in designing porous carbon, we should pay more attention to the dimension and morphology of the solid products since nanostructures can alter physicochemical properties. At the end of the discharge reaction, it was found that mesoscale particles (~100 nm) of Li_2O_2 are formed on the carbon cathode, as seen under an SEM [11,191]. With flat glassy carbon electrodes, ~40 nm thick deposits electrically passivated the electrodes [8]. While Li_2O_2 itself is an insulator, density functional theory (DFT) calculations predicted that existing neutral Li vacancies on the surface will generate some electrical conductivity [201], as shown in Fig. 30 (a).

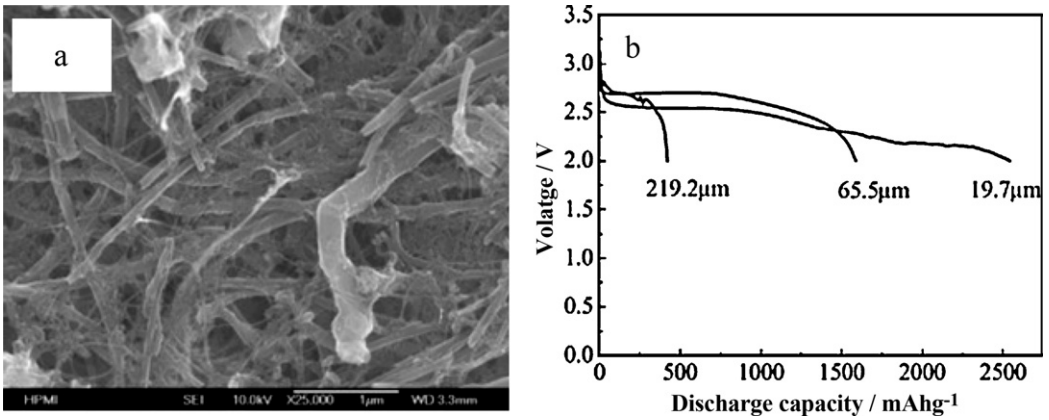

Fig. 29. (a) SEM image of a surface of air electrode made with single-wall carbon nanotube (SWNT) and carbon nanofiber (CNF). (b) Discharge curves with different thickness under a constant current density of 0.1 mA/cm^2 [195].
Reproduced by permission of The Electrochemical Society.

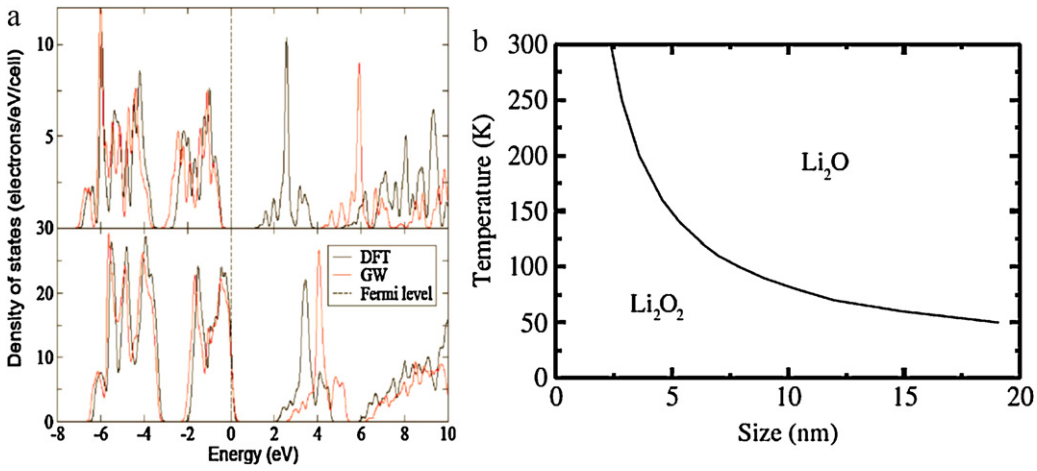

Fig. 30. (a) Density of states for pure Li_2O_2 (upper) and Li_2O_2 with a concentration of 1/16 Li vacancies (down). (b) Size-dependent phase diagram of lithium oxides. (a) Reprinted with permission from [201]. Copyright 2010, American Institute of Physics. (b) Reproduced with permission from [202].

There are conflicting reports on the composition of products, depending on the electrolyte and current density used. It would be very possible to have a Li_2O/Li_2O_2 mixture since their corresponding potentials are very close. Since their reversibility may be quite different, however, the Li_2O_2/Li_2O ratio may greatly affect the cyclability. It would be reasonable to expect that different catalysts may lead to different products. A recent study showed that morphology and size can influence the stability of phase for lithium oxides [202]. In Fig. 30 (b), it was shown that Li_2O_2 is the stable phase of lithium oxide, if the size is less than 2.5 nm at room temperature.

In summary, we should identify and design the optimized porous carbon which will lead to the optimal thickness of lithium oxide deposits, ensuring both high capacity and surface conductivity. One possibility is to design a high surface area electrode and limit the discharge potential to form a thin coating of Li_2O_2 (up to ~40 nm thick) which would still be functional. The question remains if that will give sufficient energy density (both gravimetric and volumetric) and, at the same time, leave adequate pores for electrolyte and gas transport through the electrode during cycling.

5.2.2. Bifunctional catalysts for oxygen reduction and evolution

The first successful operation of a rechargeable non-aqueous Li-air battery was demonstrated up to 3 cycles by Abraham and Jiang in 1996 using cobalt phthalocyanine-based catalysts [203]. More sustainable charge/discharge cyclability was demonstrated later by Ogasawara et al. using electrolytic manganese dioxide as catalysts for up to 50 cycles with 60% capacity retention [204,205]. Recently, 100 cycles of Li-air battery were demonstrated with capacity retention of over 60% by Toyota [206].

It is known that electrocatalysts can reduce overpotentials of charge/discharge reactions, thus increasing round trip efficiency and improving cycling performance. In general, the discharge potential is approximately 2.5–2.7 V regardless of catalysts [205]. During constant-current charging of the cell, however, the voltage increases to approximately 4.5–4.8 V without catalysts while the charge potential can be lowered down to 3.5 V depending on the choice of catalysts [10,11,18,204,205]. Two types of catalysts have shown good promise: oxide-based catalysts and noble metal catalysts.

5.2.2.1. Oxide-based catalysts. Debart et al. examined different forms of manganese oxides [11] as catalysts and demonstrated that α-MnO_2 has higher capacity (reaching 3000 mAh/g) and better capacity retention than other MnO_2 polymorphs (β, γ, λ), Mn_2O_3 and Mn_3O_4, implying the crystal structure is one of the key factors affecting the performance. They also compared the performance of α-MnO_2 in bulk and nanowire form. As shown in Fig. 31, the α-MnO_2 nanowires were very effective in forming and decomposing Li_2O_2 and exhibited higher capacity than the bulk material, demonstrating the enhanced catalytic activities of nanostructures. It was suggested that the enhanced performance of the α-MnO_2 nanowire was due to higher surface area rather than morphology effect. It was also demonstrated that excellent capacity retention can be achieved if deep discharge is avoided by limiting the discharge capacity. However, other possible differences in microscopic features (e.g., pore volume, particle size, and BET surface area) were not sufficiently investigated, making it difficult to compare the intrinsic catalytic activities of different crystal structures and dimension. It would be very useful if one can perform more detailed studies to separate the intrinsic catalytic activity from other factors.

Debart et al. also conducted a preliminary study to screen a number of different catalysts. They found other transition metal oxides such as Fe_3O_4 and Co_3O_4 can also show good performance as catalysts [205]. In particular, Co_3O_4 exhibited the best performance through a combination of high initial discharge capacity and capacity retention upon cycling. Debart et al. also examined two classic electrocatalysts currently used in the cathode of fuel cell technology: platinum and lanthanum manganate, $La_{0.8}Sr_{0.2}MnO_3$. They showed low initial discharge capacity and significant capacity loss upon cycling, but others reported conflict with these results. Minowa et al. reported improved cycle performance with another manganate, $La_{0.65}Sr_{0.4}Fe_{0.6}Mn_{0.4}O_3$ as an electrocatalyst [207]. Also, Lu et al. showed very high activities of platinum toward oxygen evolution although its activity toward oxygen reduction in aprotic electrolyte was low [10,18,208]. With all different catalysts, it was clearly seen that catalysts have little effect on the discharge voltage, but can lower the charge potential and thus improve capacity retention. This implies the charging mechanism depends on the nature of catalysts.

Giordani et al. suggested that H_2O_2 decomposition would be a reliable and fast screening tool for catalysts that promote the decomposition of Li_2O_2 during charging [209]. Using the discharged state of air electrodes (containing Li_2O_2 from the beginning), they could successfully avoid side reactions between carbonate-based electrolyte and reduced O_2 species, and found an inverse relationship between the rate constant for H_2O_2 decomposition and the charge voltage of Li–O_2 cells using same catalysts. As shown in Fig. 32, they confirmed α-MnO_2 nanowires showed

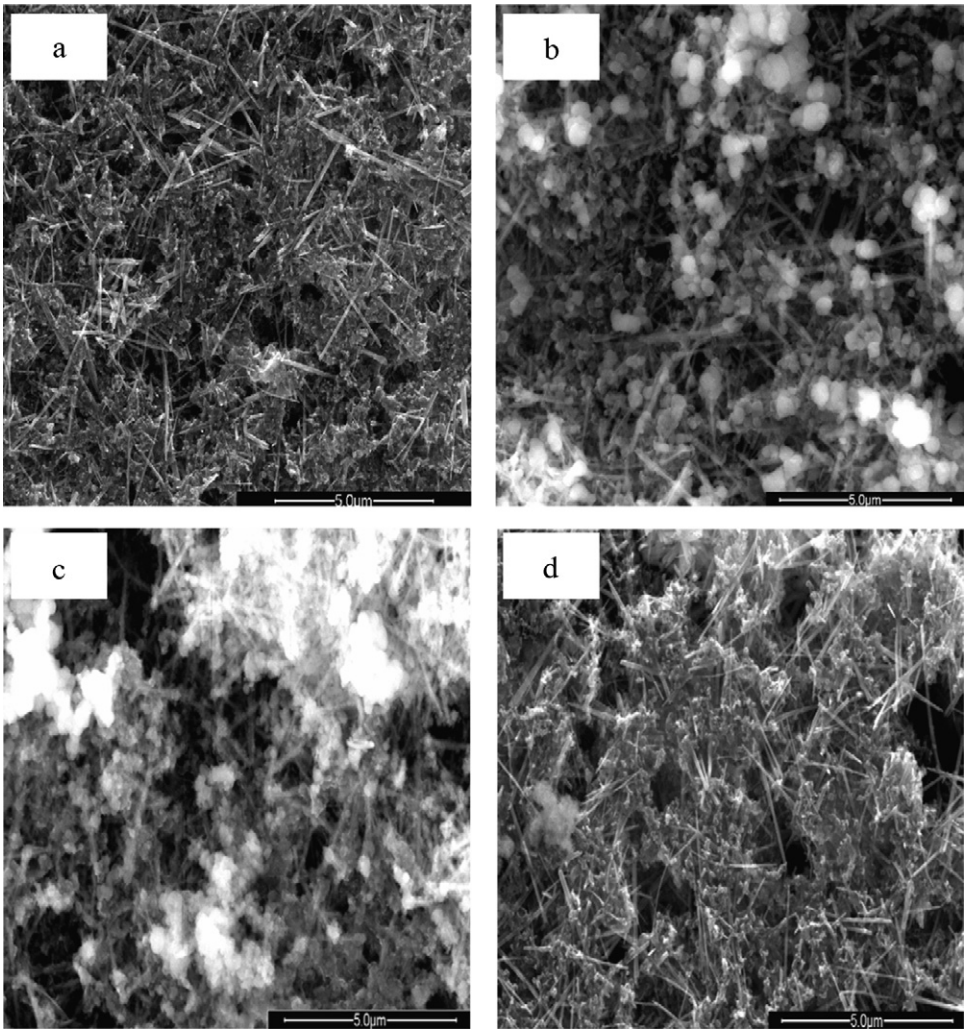

Fig. 31. SEM images of air electrode containing α-MnO_2 nanowires as catalysts at different states: (a) as-prepared, (b) partially discharged, (c) fully discharged, and (d) fully re-charged electrode. White deposits show the formation of Li_2O_2. From the supporting information of [11].

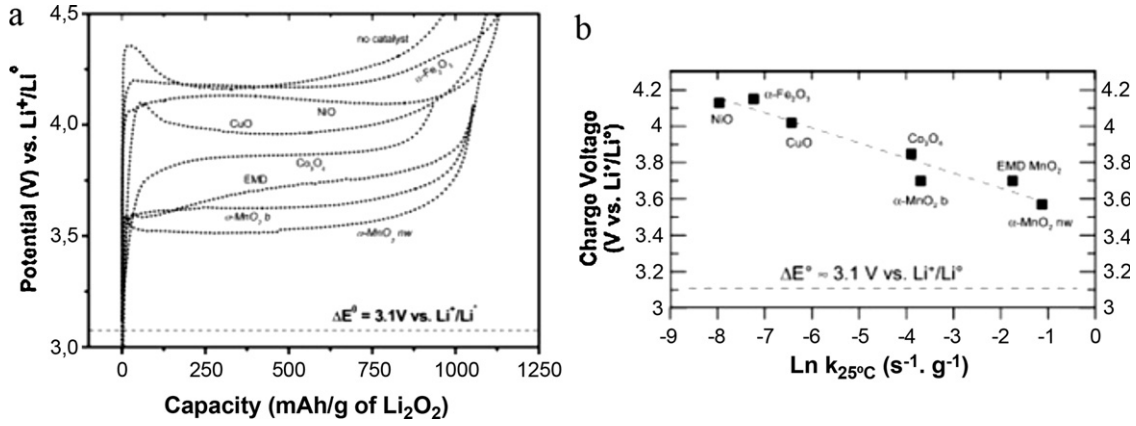

Fig. 32. (a) Effect of catalyst on the Li_2O_2 oxidation potential. (b) H_2O_2 decomposition rate constant correlated with Li_2O_2 decomposition charge voltage [209].

much better catalytic performance than the bulk form, claiming the superior catalytic properties of nanostructures. It was also suggested that overpotential for charging (Li_2O_2 decomposition) would be affected by both kinetics and thermodynamics of reactions between catalysts and Li_2O_2. More fundamental study would be required to investigate the combined effects of size, morphology, and surface composition/structure of catalysts on catalytic activity.

Jin et al. tried to improve the catalytic activity of manganese oxides by synthesizing nanostructured hollow γ-MnO_2 spheres

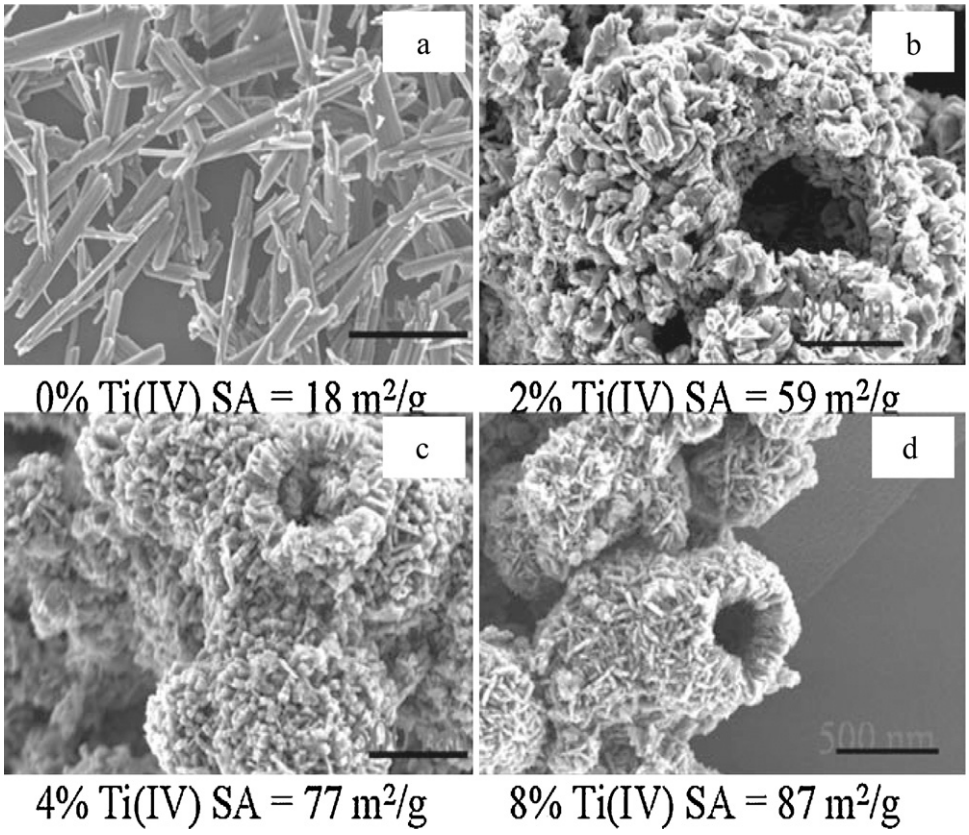

Fig. 33. SEM images of nanostructured hollow γ-MnO_2 spheres containing different amounts of titanium: (a) 0%, (b) 2%, (c) 4%, and (d) 8% [210]. Copyright Wiley-VCH Verlag GmbH & Co. KGaA. Reproduced with permission.

containing Ti (up to 8%) using a co-precipitation method [210]. Titanium ions were used as structure-directing agents to successfully form hollow spherical morphologies with high surface areas as shown in Fig. 33. Although good discharge capacity (~2300 mAh/g) was reported, there was no discussion on the charging behavior nor the effect of Ti incorporation on the electrochemical performance.

5.2.2.2. Noble metal catalysts. Although the use of MnO_2 helps lower the charge voltage and improve cycling performance, the round trip efficiency is still low, about 60%. Thapa et al. found that a mixture of Pd and electrolytic manganese oxide (without using carbon) could reduce the charge voltage to 3.5 V. The difference of charge between discharge voltage was only about 0.3 V, with good cycling performance up to 20 cycles [211]. However, the discharge capacity was relatively low due to the limited surface area of MnO_2. To increase the surface area of electrodes and improve catalytic activities, they also synthesized ordered mesoporous α-MnO_2 as catalyst and reported improved discharge capacity with the addition of small amounts of Pd [212]. This demonstrated the advantages of both nanostructures and noble metal catalysts. As shown in Fig. 34, they demonstrated that the addition of small amounts of Pd into mesoporous α-MnO_2 increased the initial discharge capacity and decreased the charge–discharge voltage difference from 0.8 V to 0.6 V.

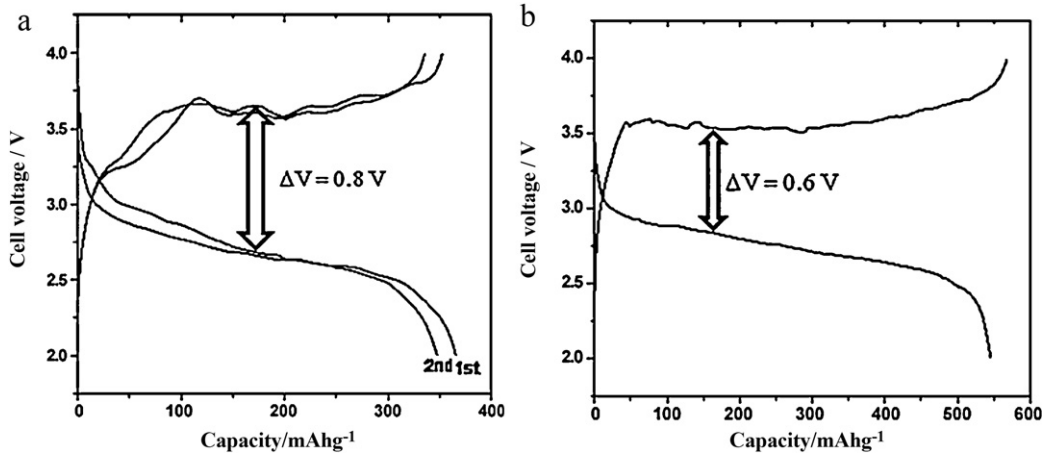

Fig. 34. Charge–discharge curves of air cathodes showing the effect of catalysts: (a) mesoporous α-MnO_2, (b) mesoporous α-MnO_2/Pd [212]. Copyright 2010, with permission from Elsevier.

Shao-Horn's group studied the effects of metal nanoparticles on the charge and discharge potentials of air cathodes [10]. They found that Au/C showed very high activity for ORR and Pt/C exhibited remarkable activity for OER. This trend agreed very well with Li_2O_2 decomposition current with the same catalysts. However, it was also mentioned that different catalysts may yield different reaction products (LiO_2, Li_2O, or Li_2O_2) with different oxidation behavior. Using this preliminary result, they successfully designed highly active bifunctional catalysts by combining Au and Pt on Vulcan carbon to yield 40 wt% PtAu/C. Fine PtAu nanoparticles with average particle size of 7 nm were uniformly distributed on carbon. These novel catalysts showed consistently higher (by 150–360 mV) discharge voltage than that of pure carbon, and much lower (by 900 mV) charge voltage than that of pure carbon. The reported round trip efficiency (73%) is much improved compared to that of bare carbon cathode (57%) [18]. As shown in Fig. 35, the discharge voltage of PtAu/C was comparable to that of Au/C and the charge voltage was comparable to that of Pt/C. This indicates PtAu/C is an effective bifunctional catalyst for oxygen reduction and evolution reactions. When current densities were decreased, the difference between discharge and charge voltage was further reduced.

The enhanced ORR activity of Au was also confirmed by rotating disc electrode (RDE) measurements on the well-defined surface of glassy carbon, polycrystalline Au and Pt in the O_2-saturated aprotic solution with the presence of lithium ions [208]. The onset of the ORR is shifted positively for Au, implying high catalytic activity. Interestingly, it was shown that the intrinsic activity of carbon itself is high enough to dominate ORR kinetics, which can explain nearly identical discharge voltage for different catalysts with high volume carbon. However, the origin of the enhanced OER activity and increased discharge capacity are not yet fully understood.

Although using catalysts with porous carbon electrodes has shown good promise, there are still many challenges. The fundamental understanding on the catalytic reaction mechanism is still lacking and it is very difficult to compare the intrinsic catalytic activities of different catalysts. For instance, different catalysts may change the morphology and composition of lithium oxide deposits, which may also affect the degree of reversibility. With certain structures of air electrodes and choice of catalysts, the deposits may be less dense and porous, causing performance to also be influenced by the microstructure. Comparison of intrinsic catalytic activities should consider the effect of microstructure. The problem of occlusion of the catalysts by formation of Li_2O_2 remains an important challenge. On discharging, the nucleation of solid product on the catalyst particle will block further catalytic reaction and on charging (Li_2O_2 decomposition), the lack of intimate contact of the Li_2O_2 with the catalyst can reduce reactivity. Admittedly, information about morphology and location of deposit is not yet available.

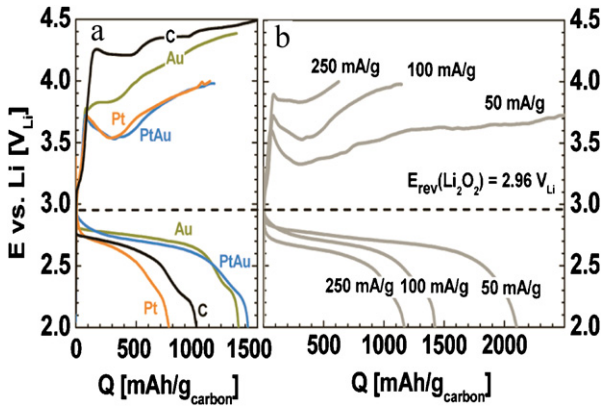

Fig. 35. (a) Charge–discharge curves of Li-O_2 cell employing different catalysts. (b) Charge–discharge curves of Li-O_2 cell employing PtAu/C at different current densities.
Reprinted with permission from [18]. Copyright 2010 American Chemical Society.

There are some problems with using nanostructured catalysts. Recent experiments performed at IBM using differential electrochemical mass spectrometry revealed that while O_2 was evolved during the charging process, significant oxidation products (e.g., CO_2) were also evolved especially in the presence of some catalysts [8]. It was claimed that oxidation of electrolyte and even carbon would be possible at high potentials and could contribute significantly to the charging currents observed. Organic carbonate-based solvents such as propylene carbonate or other mixtures have limited oxidation stability, which could be further decreased in the presence of catalysts or even Li_2O_2 in Li-air batteries [8]. It was also found that the main product formed in discharge was not an ideal compound, Li_2O_2, but was a carbonate species originating from the decomposition of carbonate-based electrolyte solvent [206]. Toyota demonstrated that the charge potential could be significantly lowered just by changing the carbonate-based electrolyte into the ionic liquid with the same cathode [213].

5.3. Electrodes in an aqueous electrolyte

Aqueous metal-air batteries such as Zn-air and Al-air systems have been studied for a long time due to their high theoretical energy density [7,189,214]. Because these systems use aqueous electrolyte, however, their operating voltage is relatively low. When Li replaces Zn or Al anode, it offers significant advantages in terms of high operating voltage and gravimetric energy density (Wh/kg) due to the low potential and light weight of lithium anodes. The first aqueous Li-air batteries were introduced in the late 1970s [215], but due to safety concerns and corrosion issues with Li anodes, this concept was not widely accepted [190]. Later, Visco et al. introduced the concept of protected lithium electrodes [216,217]. They used a water-stable NASICON-type Li-conducting ceramic electrolyte with an interlayer protecting the reaction between lithium anode and solid electrolytes. At this time, relatively small numbers of groups are working on these systems, but much more attention should be given to them. Although these aqueous systems do not possess as high theoretical capacity and energy density as non-aqueous systems, they still offer an attractive alternative approach to current Li-ion batteries. As the discharge reaction product is soluble in H_2O, the cathode clogging issues of the aprotic configurations are eliminated.

In an aqueous electrolyte, the oxygen reduction during discharge and oxygen evolution during charge can be expressed as,

$$\tfrac{1}{2}O_2 + 2e' + H_2O \underset{\text{Charge}}{\overset{\text{Discharge}}{\rightleftarrows}} 2OH^- \quad \text{(Alkaline media)}$$

$$\tfrac{1}{2}O_2 + 2e' + 2H^+ \underset{\text{Charge}}{\overset{\text{Discharge}}{\rightleftarrows}} H_2O \quad \text{(Acidic media)}$$

For both fully aqueous and mixed electrolyte configurations, the cathode reaction is essentially same. These reactions are similar to those occurring on the cathode in a proton exchange membrane fuel cell (oxygen reduction) and on the anode in a water electrolyzer (oxygen evolution). For Li-air batteries involving an aqueous electrolyte, one of the key technical challenges is to find a solid electrolyte that has sufficient Li ion conductivity and adequate stability against the aqueous electrolyte [216–221].

Aqueous Li-air batteries are basically composed of a protected metallic Li anode, aqueous electrolyte and an air cathode which has similar structures to the gas diffusion electrodes of PEM fuel cells. The functions of air electrodes are to provide uniform O_2 gas from

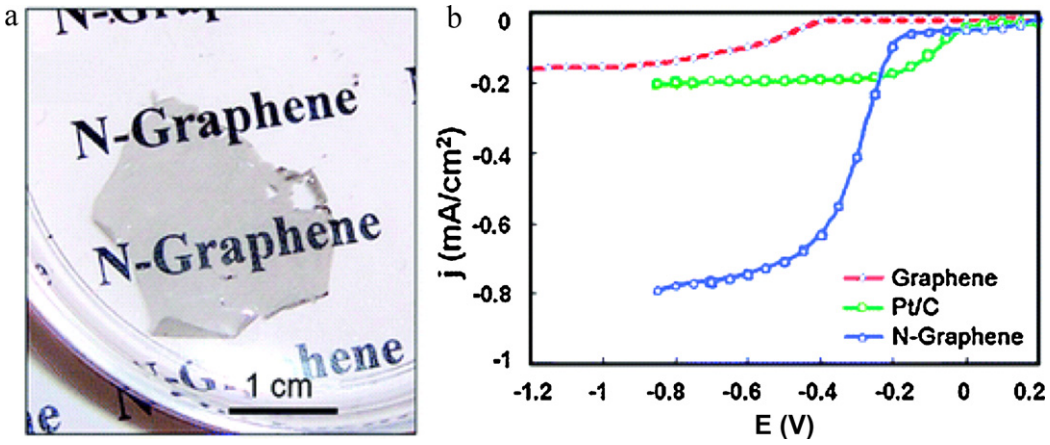

Fig. 36. (a) Image of nitrogen-doped graphene and (b) its oxygen reduction activity. Reprinted with permission from [239]. Copyright 2010 American Chemical Society.

air, and reduce the O_2 dissolved in an aqueous electrolyte on the surface of catalysts loaded on porous carbon supports. The unique features and concerns of electrodes in an aqueous electrolyte are discussed in detail in the following sections.

5.3.1. Porous carbon-based electrodes

There are comprehensive review articles on catalyst supports [222–228] and electrode structures for PEM fuel cells [229] and alkaline fuel cells [230]. The knowledge developed for these technologies is applicable to the catalyst support and electrode structure for aqueous Li-air batteries. Unlike non-aqueous Li-air batteries, the reaction products in an aqueous Li-air battery are soluble in the electrolyte. It is unlikely that performance will be limited by clogging the pores of carbons as seen in organic electrolytes. However, the solubility of LiOH (12.8 g in 100 ml H_2O at room temperature) will limit the discharge capacity for aqueous Li-air system [231,232].

In current PEM fuel cell cathodes, various materials such as carbon [222–225], ceramic [226], polymer [227], and composite [228] materials are being investigated for catalyst supports to increase the surface area of catalysts, thus enhancing catalytic activities. Recently, carbon nanotubes [233–236] and graphenes [237–239] have shown good promise as efficient catalyst supports due to their high surface area and electronic conductivity. Enhanced catalytic activities and improved stability were reported compared to conventional porous carbon black. In particular, Gong et al. demonstrated much better catalytic activity for oxygen reduction and long-term stability (after continuous potential cycling between 0.2 and −−1.2 V vs. Ag/AgCl for 100,000 cycles) of vertically aligned nitrogen-doped carbon nanotubes without catalysts in air-saturated 0.1 M KOH solution [234]. Such materials should be tested for oxygen reduction in Li-ion containing aqueous electrolytes. Similarly, as shown in Fig. 36, the same group reported much better catalytic activities for oxygen reduction and long-term stability (after continuous potential cycling between 0 and −1.0 V vs. Ag/AgCl for 200,000 cycles) of nitrogen-doped Graphene (N-graphene) without metal catalysts than conventional Pt/C catalysts in alkaline conditions [239]. This favorable effect of nitrogen-doping into carbon materials toward higher oxygen reduction activities in an alkaline electrolyte can be applied to develop cost-effective, highly functional cathodes for aqueous Li-air batteries.

The development of carbon-based electrodes showing excellent ORR activities without any metal catalysts is very important as such materials would benefit both fuel cells and Li-air batteries. Liu et al. also fabricated nitrogen-doped mesoporous graphitic arrays, using mesoporous silica SBA-15 as templates as shown in Fig. 37, and demonstrated superior catalytic activity and long-term stability (after a constant voltage operation at −0.26 V vs. Ag/AgCl for 20,000 s) in O_2-saturated 0.1 M KOH solution [240]. Furthermore, their study indicated that graphite-like nitrogen atoms account for the observed excellent catalytic activities toward oxygen reduction. Recently, current status and perspectives of high-performance porous polymeric materials were reviewed [241]. We view highly porous conducting polymeric carbon, if properly modified, to have good promise as catalyst supports or electrodes for aqueous Li-air batteries.

5.3.2. Bifunctional catalysts for oxygen reduction and evolution

As shown in Section 5.2.2, electrocatalysts can significantly reduce overpotentials of charge/discharge reactions, thus increasing round trip efficiency and improving cycling performance. Two types of catalysts have shown good promise with aqueous electrolyte: noble metal catalysts and non-precious catalysts.

5.3.2.1. Noble metal catalysts. As mentioned previously, water-stable three layer lithium anodes were proposed. This could enable the advent of safe aqueous Li-air batteries and even Li-water batteries for submarine applications. Using this configuration, Visco et al. developed Li-water batteries and demonstrated long discharge for a period of nearly 2 months at a current density of 0.5 mA/cm^2 [217]. In this work, they used platinum as cathode to successfully reduce the dissolved oxygen in aqueous 4 M NH_4Cl solution. As shown in Fig. 38, they also fabricated and demonstrated successful operation of aqueous Li-air batteries which showed stable OCV and high performance, even at high current density of 5 mA/cm^2.

The rechargeability of aqueous Li-air batteries was demonstrated by Zhang et al. [221]. In this study, they showed a stable OCV of 3.7 V at 60 °C, and successful charge–discharge performance using 1 M LiCl as electrolyte and Pt as a positive electrode. Later, using an improved interface with a three-layer lithium anode, they showed an improved OCV of 3.8 V at 60 °C and reversible discharge–charge performance at different current density of up to 1 mA/cm^2. A quite flat voltage of 3.5 V and 4.2 V were observed during the discharge and charge process, respectively. However, this Li-air battery could not be operated in a deep discharge state, as the solid ceramic electrolyte was unstable under an alkaline electrolyte.

Later, they used a similar configuration (three-layer lithium anode), substituting acetic acid–water as the electrolyte. The demonstrated high energy density was 779 Wh/kg (including the weight of lithium anode and electrolyte), much higher than that of conventional Li-ion batteries using graphite and $LiCoO_2$ as the

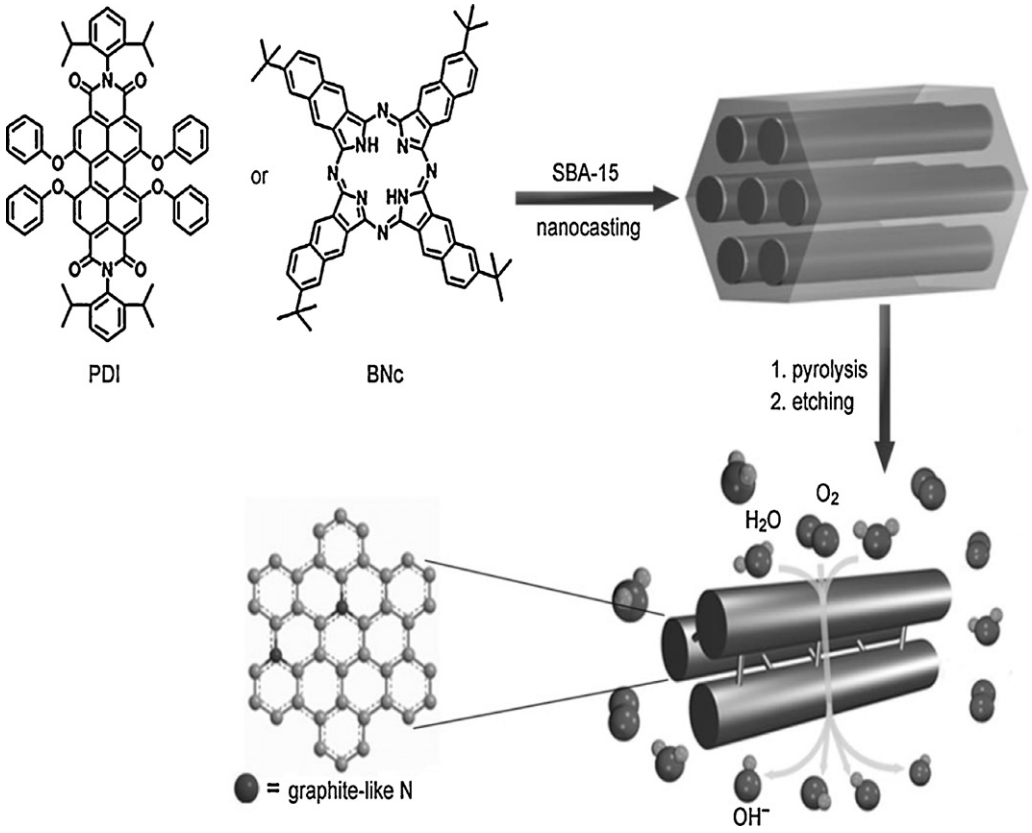

Fig. 37. Preparation of nitrogen-doped mesoporous graphitic arrays as metal-free catalysts for ORR [240].
Copyright Wiley-VCH Verlag GmbH & Co. KGaA. Reproduced with permission.

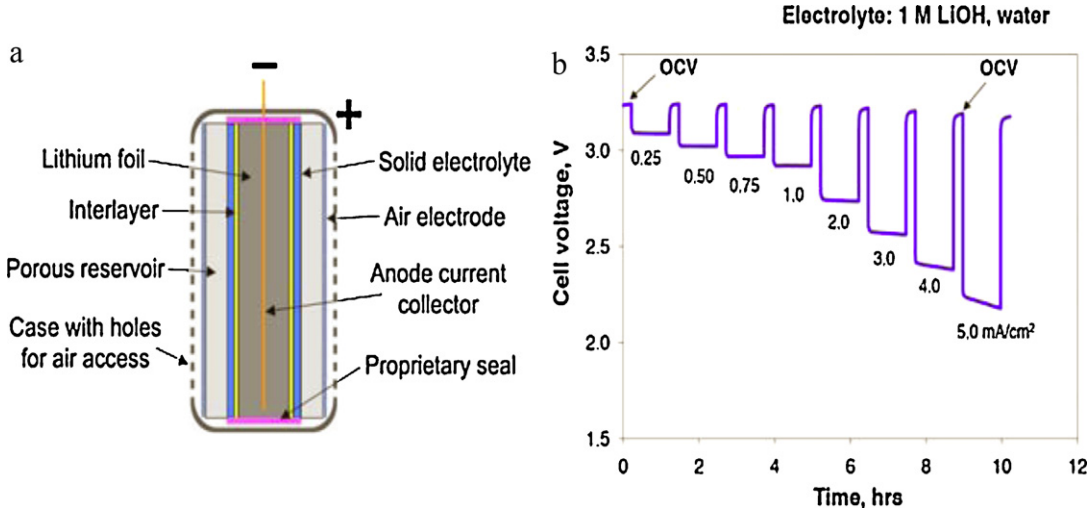

Fig. 38. (a) Schematic diagram of aqueous lithium-air battery developed by Polyplus. (b) Discharge curve of aqueous Li-air battery as a function of discharge current density [217].
Reproduced by permission of The Electrochemical Society.

anode and the cathode, respectively. They used a carbon air cathode employing fine Pt nanoparticles (1–4 nm) as catalysts. The OCV of this cell was 3.69 V at room temperature, and the charge–discharge performance was conducted at a constant current of 0.5 mA/cm^2 at 60 °C under 3 atm of air to suppress evaporation of the electrolyte. As shown in Fig. 39, flat discharge–charge curves were obtained. Good cycling performance up to 15 cycles was also demonstrated. The potential difference between the discharge and charge curve was about 0.75 V. This should be further lowered by use of more active catalysts to develop high-performance aqueous lithium/air batteries.

5.3.2.2. Non-precious catalysts. As described earlier, the O_2 reduction in aqueous Li-air batteries is quite similar to that of fuel cells, which often use expensive platinum or platinum alloy catalysts [243], greatly reducing the economical competitiveness and commercial viability of aqueous Li-air batteries. Extensive efforts have been made to develop non-precious catalysts for PEM fuel

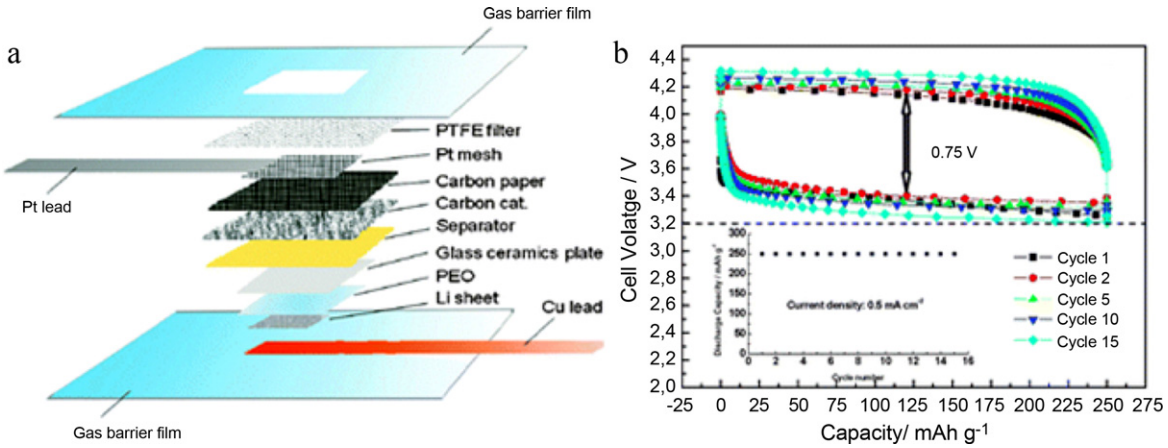

Fig. 39. (a) Schematic diagram of the proposed lithium-air battery using aqueous electrolyte. (b) Charge–discharge profile of air cathodes at 0.5 mA/cm^2 and 60 °C [242]. Reproduced by permission of the Royal Society of Chemistry.

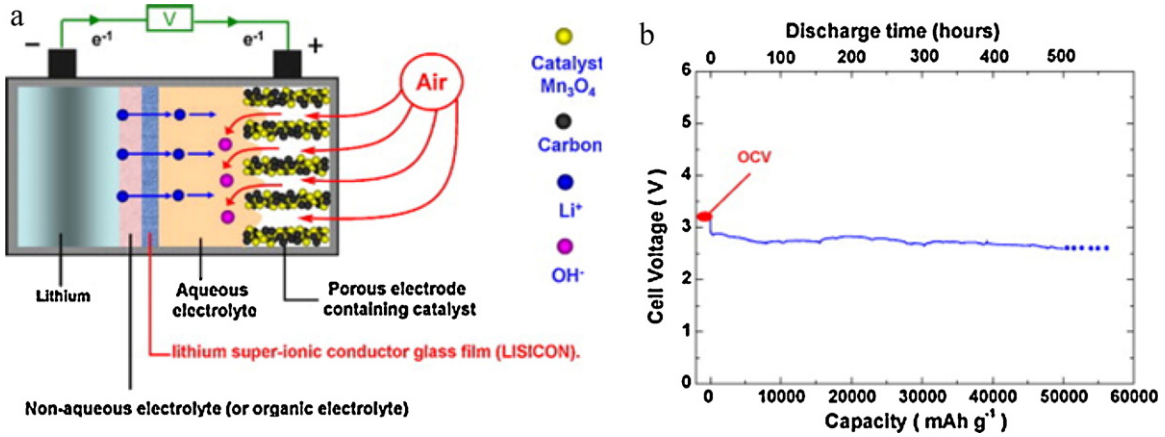

Fig. 40. (a) Schematic diagram of the composite cathode developed for aqueous Li-air batteries, (b) long-time continuous discharge curve at current density of 0.5 mA/cm^2 [231].
Copyright 2010, with permission from Elsevier.

cells, as discussed in several recent reviews [244–247]. This knowledge would also be very useful in developing cost-effective air-cathodes for Li-air batteries.

Wang et al. demonstrated successful operation of aqueous Li-air batteries using non-platinum catalysts [231]. As shown in Fig. 40, a Mn_3O_4 based gas diffusion electrode was used as a positive electrode. A continuous discharge operation of 500 h demonstrated that their cathodes could continuously reduce O_2 from air and deliver over 50,000 mA/g based on total cathode mass (carbon + binder + catalyst). This is much higher than those for non-aqueous Li-air batteries reported to date. The operating voltage was kept flat at about 2.8 V while discharged at 0.5 mA/cm^2; it maintained 2.3 V even at a current density as high as 5 mA/cm^2. During the discharge process, the concentration of LiOH increases and the low solubility of LiOH in H_2O is the limitation of Li-air batteries employing aqueous electrolyte. However, it would be possible to replace the reaction products mechanically with fresh reactants as in fuel cells [231]. This concept holds promise for automotive applications as this type of battery does not need a hydrogen storage tank and the operating voltage is higher than conventional fuel cells. Wang et al. subsequently introduced additional Ti mesh as an O_2 evolution electrode and demonstrated that this type of Li-air battery can also be electrochemically reversible [248].

Wang et al. also proposed that the cyclic conversion reaction between Cu and Cu_2O can catalyze the electrochemical reduction of O_2 in aqueous solution [249]. They demonstrated the successful operation of aqueous Li-air batteries using Cu plate as counter electrode in contact with 1 M $LiNO_3$ solution. As shown in Fig. 41, the OCV was about 3 V and the operating voltage was kept at 2.6 V during discharge. The catalytic activity of metallic copper is still low but it is expected to improve by using nanostructured Cu instead of bulk plate.

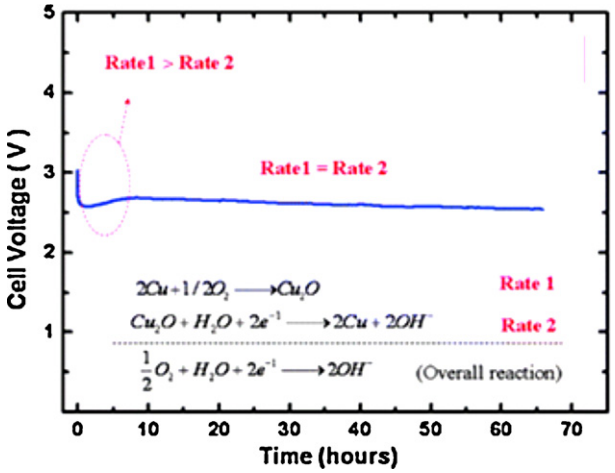

Fig. 41. Discharge curve of air cathodes using Cu catalyst based on Cu/Cu_2O conversion process at constant current of 0.083 mA/cm^2 [249].
Reproduced by permission of the Royal Society of Chemistry.

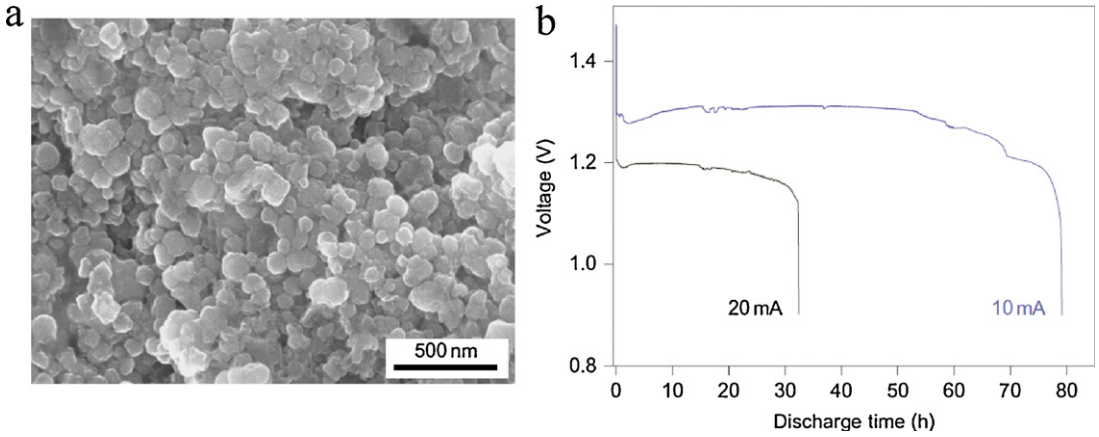

Fig. 42. (a) SEM image of $Co_xMn_{3-x}O_4$ nanoparticles as oxygen reduction and evolution catalysts. (b) Discharge curve of Zn-air batteries made with nanocrystalline spinels. Adapted by permission from Macmillan Publishers Ltd.: Nat. Chem. [250], copyright 2011.

We can also learn from the knowledge developed for cathodes of Zn-air batteries, using similar architectures with Zn metals as anodes and air electrodes as cathodes in aqueous electrolyte. There were recent comprehensive review papers on air cathodes for Zn-air batteries [189,214] and we believe promising materials for Zn-air batteries can be also applied to the development of high-performance aqueous Li-air batteries. Cheng et al. could successfully synthesize nanocrystalline $M_xMn_{3-x}O_4$ (M = divalent metals) spinels at room temperature [250]. They explained their good electrocatalytic activities toward ORR/OER in 0.1 M KOH or KCl solution were due to high surface areas and concentration of defects. Nanoparticulated $Co_xMn_{3-x}O_4$ showed comparable ORR activities to those of Pt/C catalysts and demonstrated considerable specific energy densities when tested as catalysts for Zn-air batteries as shown in Fig. 42. In addition, Winther-Jensen et al. prepared porous polymer (PEDOT) based electrodes as O_2 reduction catalysts and demonstrated successful discharge operation of Zn-air batteries [251]. These non-precious catalysts, if successfully developed, would impact both fuel cells and Li-air batteries and deserve more attentions.

5.4. Summary

Li-air batteries have a great potential to offer energy density much higher than those of current Li-ion batteries. However, many fundamental questions are yet to be addressed to realize the potential of Li-air batteries. Among many oxide-based catalysts developed for non-aqueous Li-air batteries, α-MnO_2 nanowires have shown the best promise by delivering much higher discharge capacity and improved capacity retention than its bulk form, other polymorphs, and other transition metal oxides. When combined with noble metal, its catalytic activities were further improved. Nanoparticles of Au and Pt dispersed on porous carbon (PtAu/C catalysts) showed excellent bifunctional catalytic activities and very high round trip efficiency.

To date, non-aqueous Li-air batteries have attracted much attention because of their higher energy density than that of aqueous Li-air batteries. However, aqueous Li-air batteries based on a water-stable lithium anode (protected by a suitable coating) have demonstrated a superior discharge capacity of ~50,000 mAh/g, since reaction product is soluble in the aqueous electrolyte. This type of battery is very promising for electric vehicles.

Although there were limited numbers of research articles reporting the effect of nanostructures in this filed, we expect that nanostructured materials have an important role to play in achieving higher capacity, faster cycling rates, and longer cycling lifetime of cost-effective, rechargeable Li-air batteries.

5.5. Remaining challenges

While the theoretical energy density of Li-air batteries is very high, the obtainable energy densities for the Li-air systems involving aprotic electrolyte are still relatively low, due primarily to the insolubility of the insulating discharge products (Li_2O_2) in the non-aqueous organic electrolyte. The progress in development of Li-air batteries is hammered by the lack of a fundamental understanding of electrochemistry at electrode surfaces. It is not clear which step is the rate-limiting step of the electrochemical reactions and what kinds of electrode materials would be active for the reactions.

Development of a commercially viable Li-air battery requires both scientific and technological breakthroughs. From a scientific point of view, it is necessary to unravel the mechanisms of the electrochemical processes occurring on the electrode surface: the elementary reaction steps, the reaction sequence, and the rate limiting steps. Also, novel nanostructured air-breathing electrode materials must be created with adequate stability and excellent catalytic activity for oxygen reduction (during discharging) and evolution (during charging). From a technological point of view, porous electrode architectures must be created to accommodate the deposition of discharge products and to maintain fast transport of reactants to active sites and products away from those sites; catalysts must be well dispersed on the surface of air electrodes, and the electrodes can be fabricated cost-effectively. Some of the major challenges are listed below:

(1) The obtainable discharge capacity (or energy density) is relatively low (although the theoretical ones are much greater) and diminishes rapidly with the rate of discharging.
(2) The overpotentials for charge and discharge are relatively high (or the round trip energy efficiency is relatively low), more so at higher charge/discharge rates.
(3) The typical cycling rates (or the power densities) are relatively low, much lower than current lithium-ion batteries.
(4) In addition to oxygen evolution, oxidation of organic electrolyte and carbon electrode were also reported since significant oxidation products (e.g., CO_2) were detected by differential electrochemical mass spectrometry during recharge, especially in the presence of catalysts and Li_2O_2.
(5) The capacity of Li-air batteries fades very fast upon cycling (i.e., low cycle life), compared to current lithium-ion batteries.

(6) The performance (i.e., capacity) of Li-air batteries depends very sensitively on the amount of electrolytes filled in the cathode. Low oxygen solubility and diffusivity in current electrolytes (both aqueous and non-aqueous) also result in low rate capabilities.
(7) The stability of nanostructured catalysts often compromises catalytic activities especially when used in strong acid or alkaline electrolyte.

5.6. Opportunities and new directions

Most problems of O_2-breathing cathodes for Li-air batteries are associated with the deposition of insoluble and insulating discharge products. These deposits accumulate on active electrode surfaces, thus physically blocking the active sites for electrode reactions. Optimization of the pore structures of carbon electrodes may help to minimize this problem. More active, nanostructured catalysts should be developed to reduce the overpotentials (especially lower the charge potential) and enhance the round trip efficiency. Different catalysts may be required for discharging and charging. Better understanding of the origin of large polarization may offer an opportunity to dramatically lower the activation energy, especially for recharging (or decomposition of Li_2O_2), allowing improved rate capability of Li-air batteries.

Many unique concepts developed for the air cathode in a PEM fuel cell may be applicable to the O_2-electrode in a Li-air battery, including enhanced catalytic activities of platinum catalysts by shape-controlled synthesis [252] and improved stability by synthesizing Au–Pt core–shell structure [253]. We may develop functionally graded porous gas diffusion electrodes, where macro-porous carbon fiber paper (or cloth) would act as both current collector and uniform gas diffusion media; a thin micro-porous layer (porous carbon + catalysts) would provide sufficient reaction sites for the formation/decomposition of lithium oxide. Also, the introduction of bipolar flow-field plates and air-manifold systems should be considered to optimize the design of Li-air batteries for large battery systems. Thin Li^+ conducting polymer can be introduced to porous air cathodes to facilitate the transport of both Li^+ and O_2 to the active sites.

Li-air batteries should compete with both current Li-ion batteries and fuel cell technologies for many applications. It should be noted that vehicles powered by fuel cells have already demonstrated ~300 mile range [254]; however, the cost of the Pt-based catalysts is still prohibitive for commercialization. Therefore, more efforts should be given to the investigation of non-precious catalysts to develop cost-effective Li-air batteries. Substantial improvements in rate capability are required for Li-air batteries to be considered practical. The area-specific power capability of 1 W/cm^2 and 30 mW/cm^2 has been demonstrated for fuel cell and Li-ion batteries, respectively [254]. However, the state-of-the-art Li-air batteries (non-aqueous type) demonstrated only ~0.3 mW/cm^2 (~3 mW/cm^2 with reduced capacities). Also, charge and discharge current densities should be improved to larger than 10 mA/cm^2, two orders of magnitude higher than the presentably deliverable current densities of 0.1 mA/cm^2 (1 mA/cm^2 with reduced capacities). These goals should be achieved with air, not O_2.

Theoretical approaches such as DFT calculations may provide useful insights into the energetics, reaction pathways, sequence, and mechanism of electrode processes. Fundamental understanding of these processes will provide useful insights vital to achieving science-based rational design of better electrodes. When corroborated with *in situ* and *ex situ* characterization techniques, modeling and simulations can be useful for optimization of electrode structures and performance. In particular, the information on morphology and location of insoluble and insulating product formations would be very useful in the design of ideal pore structures for high-performance air electrodes.

6. *In situ* characterization of electrode materials

This section reviews the current state of the science for *in situ* characterization tools available for fundamental study of nanostructured materials for Li batteries, including X-ray absorption spectroscopy (XAS), nuclear magnetic resonance (NMR), and Raman spectroscopy. These methodologies, with differing and unique advantages, will be presented from the point of view of acquiring information vital to gaining insights into rational design of nanostructured electrodes. In particular, XAS is a very powerful tool since it provides (in principle) both atomic and electronic structure local to all active species in Li batteries. Synchrotron-enabled XAS will be discussed in the context of other complementary X-ray based techniques available at a synchrotron light source: X-ray diffraction (providing crystallographic, grain/particle size and strain information) and X-ray photoelectron spectroscopy (providing near-surface electronic structure).

6.1. Synchrotron-based X-ray techniques

The performance and durability of Li-ion batteries are intimately determined by the ability of the cathode and anode materials to accommodate and release Li with pre-designed predictability and fidelity. A cross-cutting challenge in developing a profound understanding of energy storage and conversion processes in Li batteries rests in the direct measurement of the atomistic processes involved during battery operation. The required characterization tool needs to provide element-specific information and should do so with high resolution spatially, temporally, and in information-space. Such information would provide an element-specific electrochemical roadmap that allows us to have a much more knowledge-driven approach to the design of the next generation of Li-ion batteries.

Structural information local to each atomic species can only come from local scattering events due to species-specific resonances, whether through a core electron excitation or a bond vibration. X-ray absorption spectroscopy (XAS) is unique among local-scattering-based techniques in that it simultaneously provides the local electronic structure (the nature of the chemical bond) and the local atomic structure (bond distance and coordination). Furthermore, XAS can be carried out with the specicity of nearly every element in the periodic table (with H and He typically too low in energy for the X-ray optics of beamlines) and depends on the low and high cutoff energies of particular synchrotron beamlines; it should be noted that information on H can be obtained indirectly from its chemically bonded near-neighbors. At a dual ring synchrotron such as the National Synchrotron Light Source (NSLS), where one ring is optimized for soft X-rays and the other for hard X-rays, XAS study of nearly every element is possible. These factors make XAS a very powerful technique for fundamental characterization of battery materials by routine and expert users, when combined with some general properties of the synchrotron beam: high brightness, short photon pulse trains (down to sub-picoseconds), polarization of the synchrotron beam, and future high spatial resolution (currently in the 100 nm scale in best cases, but projected to be ~ few nm range in the next generation instruments). We will examine XAS studies of Li batteries in more detail in Section 6.2.

6.1.1. X-ray diffraction (XRD)

X-ray diffraction (XRD) using synchrotron radiation provides structural information from coherence between repeated structural

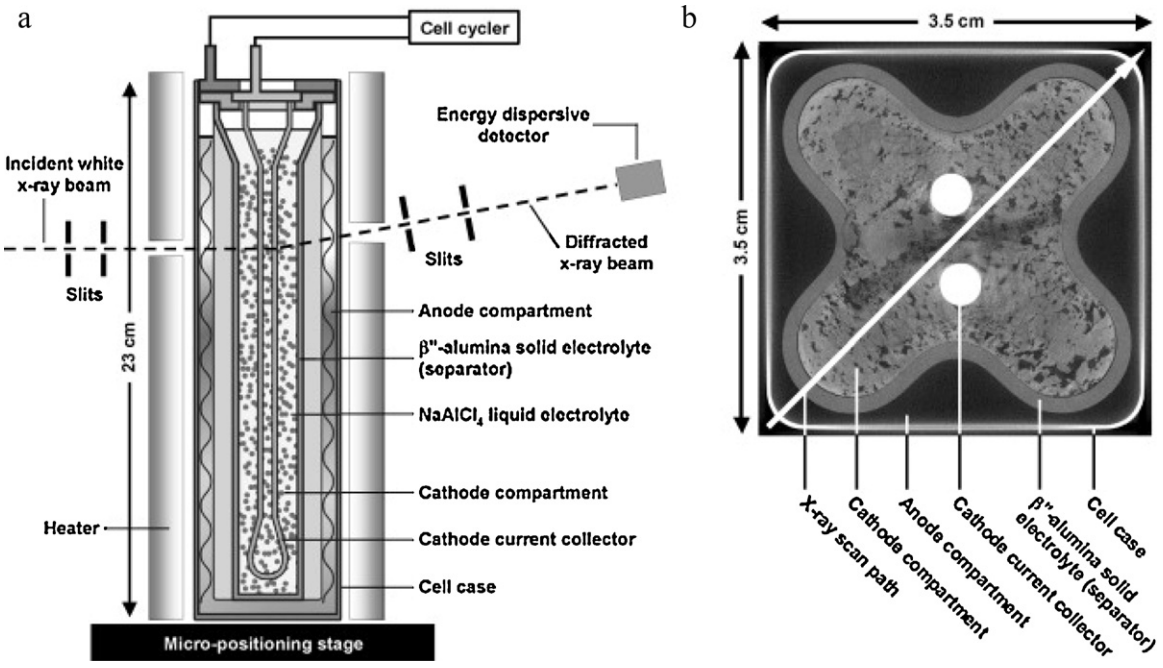

Fig. 43. (a) Schematic of experimental cell design, and (b) the computed tomography image of a sodium metal halide battery for *in situ* synchrotron EDXRD study [261]. Copyright 2011, with permission from Elsevier.

units in the materials but not necessarily on the subtleties within the units. If there is limited long-range structural repetition, the coherence of the scattered X-rays is diminished, as is the structural signal. This dependence on long-range order is a fundamental weakness of XRD in studying nanostructures. With decreasing dimensions of nanostructures, the coherence-dependant signal intensity diminishes accordingly to the vanishingly small limit of the Debye–Sherrer equation (even in the case of crystallographic order within the nanostructures). This is all the more true if there is inherent disorder within the nanostructures themselves. Still, crystal phase identification is a very worthwhile exercise when one is following the chemical reactions within a battery and, thus, XRD should be carried out to complement XAS whenever possible.

An early example of the creative use of *in situ* XRD was demonstrated by Amatucci et al. In their highly cited work (currently more than 330 citations), they showed the end member compound in the full delithiation of prototypical $LiCoO_2$ to CoO_2 [255] using their *in situ* cell [256]. The work of Amatucci and co-workers follows that of earlier work on Li_xTiS_2 by Dahn and Haering [257], and was succeeded by a host of other *in situ* diffraction studies by other researchers. Some of the highly cited early work done using *in situ* XRD include: the analysis of the structure of synthesized amorphous vanadates by Denis et al. [258], the study of the Li intercalation reaction into nanostructured anatase TiO_2 by van de Krol and Meulenkamp [259], and the structure of $Li_xMn_2O_4$ by Mukerjee et al. [260].

The penetrative power of hard X-rays can be used to great effect to produce tomographical diffraction slices through a real battery. Collecting this data during battery operation allows for the construction of an electrochemical landscape over intra-battery space and reaction time [261]. Rijssenbeek and co-workers have elegantly demonstrated the use of synchrotron "white" beam (full bandwidth of X-rays) to conduct *in situ* energy dispersive X-ray diffraction (EDXRD) (Fig. 43). With the highly penetrative hard X-rays, the experimental cell design is very forgiving and similar *in situ* experiments can be conducted on fully assembled Li-ion and Li-air cells during cycling.

6.1.2. X-ray photoelectron spectroscopy (XPS)

As a near-surface sensitive technique, XPS has strong promise for chemical analysis in nanostructures since these structures have significant fraction of their volume occupied by the surface atoms. It should be emphasized that an XPS analyzer (energy discriminating detector) is sensitive predominantly to the signal electrons emanating from within about one inelastic mean free path (IMFP) below the surface. With typical setups using Al or Mg Kα as a fixed energy source, the technique is rendered sensitive only to the near-surface atomic layers. However, since the degree of surface sensitivity depends on the kinetic energy of those emanating electrons, a synchrotron source allows XPS to have variable depth sensitivity. By varying the photon energy, one can change the kinetic energy and, therefore, the IMFP of a specific photo-emitted core electron, allowing the degree of surface sensitivity to be tuned.

The strength of XPS, that it is electron-emission based, is also its shortcoming when designing *in situ* experiments. The short IMFP of the photoelectrons mandates that the sample face be open to the energy discriminating detector. Materials within sealed cells (to trap liquid electrolytes, for example) cannot be accessed by XPS. One of the main problems in determining the true surface (top one-two atomic layers) composition of real nanostructures is that real nanostructures have curved surfaces. When their "surface" composition is measured directly, e.g., by using X-ray photoelectron spectroscopy (XPS), the result is averaged over multiple sampling depths of the particles. This is because the length of the path that any given photoelectron travels through the sample differs depending on the latitudinal position of the particle, which provides the "compositional signal" (see Fig. 44). Hence, flat model samples should be synthesized and characterized under realistic conditions whenever possible. It is true that using low energy probes, such as in low-energy ion scattering (LEIS) [262], enables us to obtain a compositional signal that does indeed come from the surface, but even in this case the signal intensity is improved by working with flat surfaces. Also, unlike LEIS, which confines us to the surface, variable kinetic energy XPS allows for non-destructive depth profiling, as described above. Furthermore, XPS provides

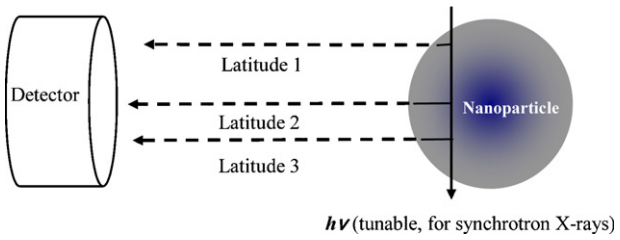

Fig. 44. XPS photoelectrons created by the source X-rays at different latitudes (1, 2 and 3) emanate from, and, therefore, carry signal from different depths of the particle.

information about chemical shifts which can then be used to measure any phase segregation between the core and the surface.

While there is a body of literature on the *ex situ* XPS study of Li battery electrodes, no *in situ* XPS study of Li batteries has yet been reported. However, following the recent development of ambient/high-pressure XPS successfully applied to *in situ* catalysis studies, it is only a matter of time before open electrochemical cells containing liquid electrolytes will be used to study the surfaces of Li-battery electrodes under *in situ* conditions.

6.2. In situ XAS experiments for the study of Li batteries

In situ XAS using hard X-rays has been conducted by several groups around the world [263–266]. Before looking into *in situ* possibilities with XAS, it may be instructive to first describe the information content of XAS in a bit more detail. An X-ray absorption spectrum is delineated into two distinct energy regions (Fig. 45). The region within about 30 eV or so above the edge is called the X-ray absorption near-edge structure (XANES). This region is strongly influenced by unoccupied valence and conduction band structure and, therefore, is sensitive to chemical bonds. The region beyond that is called extended X-ray absorption fine structure, or EXAFS. This region is strongly influenced by the type and geometric position of the nearest neighbor atoms. This delineation mostly helps in the standardized treatment of XAS data.

Since XAS requires an energy-tunable X-ray source, it is carried out at synchrotron beamlines that are maintained by on-site scientists. The experimental "users" bring their samples and peripheral equipment and set up their experiment in the beamline end station, which primarily contains the sample stage and the detectors. Thus, the design of an XAS experiment is often relatively simple from the point of view of the user-end experimentalist. Fig. 46 shows the outlay of a typical hard X-ray XAS beamline.

The physics between the XANES and EXAFS regions is, of course, continuous, but it is instructive to separately visualize the behavior of the photoelectron in these two regions. Above its ionization energy an electron, emerging from its initial state of a specific

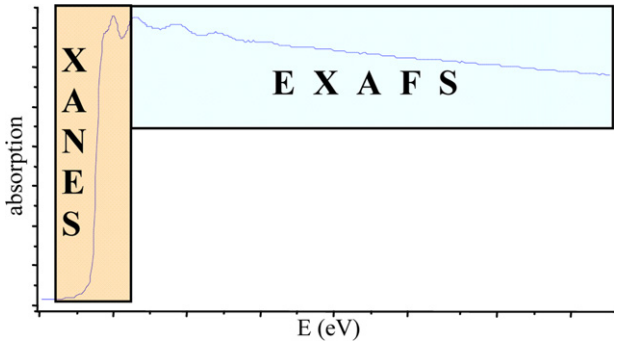

Fig. 45. A typical XAS spectrum showing the delineation between the XANES and EXAFS regions.

orbital of a specific element in the sample, can be in resonance with various empty final states. The final states are the local mixed orbitals representing the chemical bonds, such as molecular orbitals (MOs), and the electron transitions to these states produce the XANES spectrum. The X-ray absorption is proportional to the transition probability between the initial atomic state and the final states:

$$\mu \propto \left| \int \psi_f^* \hat{\varepsilon} \cdot \vec{r} e^{i\vec{k}\cdot\vec{r}} \psi_i \, d^3 r \right|^2$$

where μ is absorption, ψ_i and ψ_f are the initial and final states, and $\hat{\varepsilon}$ is the electric field vector of the incident synchrotron photon.

With higher kinetic energy, the photoelectron can be treated as a plane wave that scatters from the neighboring atoms. The interference between the outgoing and backscattering electron waves in this region set up a standing wave. As the photoelectron kinetic energy increases, its wavelength decreases. Consequently, the phase shift between the outgoing and returning waves changes at the location of the absorber atom. This phase shift, in turn, affects the probability for X-ray absorption by the absorber atom, with no phase shift (constructive interference between the outgoing and backscattered wave) causing a maximum in X-ray absorption, and a phase shift of $\lambda/2$ (destructive interference) causing a minimum in X-ray absorption. Because the average distance between the absorber and the neighboring atoms does not change, the waves will progressively go in and out of phase, as the kinetic energy increases. Therefore, the EXAFS region, which scans across the increasing kinetic energy of the photoelectron, shows oscillations with energy as can be seen in Figs. 45 and 47.

Both the XANES and EXAFS data should be collected whenever possible since the information obtained from each region is somewhat different. Energy shifts in the XANES region point to oxidation or reduction of the absorbing atom (and, in some cases, concurrent changes in absorber-nearest-neighbor bond length) while the changes in the XANES intensity are caused by changes in the density of final state. Oscillations in the EXAFS region can be converted from energy-space to k-space (momentum space) and Fourier transformed to real space to obtain a function that is proportional to the radial distribution function. The step-by-step process for this conversion is shown in Fig. 47.

The EXAFS oscillations in k-space, $\chi(k)$, can be represented by the sum of contributions from all the scattering paths of the photoelectrons:

$$\chi(k) = \sum_j \frac{N_j}{r_j^3} S_0^2 * \frac{F_j}{k} \exp\left(\frac{-2r_j}{\lambda}\right) \exp(-2\sigma_j^2 k^2) \sin[2k * r_j + \phi(k)]$$

where N_j is the coordination number of atoms at a distance r_j and N_j/r_j is the approximation of the partial radial distribution function (PRDF), S_0^2 is the many-electron overlap factor, F_j is the backscattering amplitude, and $\exp(-2(_j^2 k^2)$ is the Debye–Waller factor representing the Gaussian distribution of atomic neighbor positions due to static and thermal disorder in the material. Finally, the $\sin[2k^* r_j + \varphi(k)]$ represents oscillations with $[2k^* r_j + \varphi(k)]$ being the phase of the electron. The $\chi(k)$ function and the corresponding Fourier transform $\chi(r)$ can be calculated for a model cluster using several freely available codes. The program most commonly used and best documented for this calculation is FEFF [267]. It is self-evident that the EXAFS oscillations are rich with local structural information that can be gleaned by fitting experimentally measured $\chi(k)$ with that simulated from a model.

6.2.1. Soft X-ray XAS

In X-ray parlance, "soft" X-rays are typically those with <2 keV energy, whereas "hard" X-rays typically imply >4 keV energy. This leaves the often-overlooked 2–4 keV region belonging to the so-

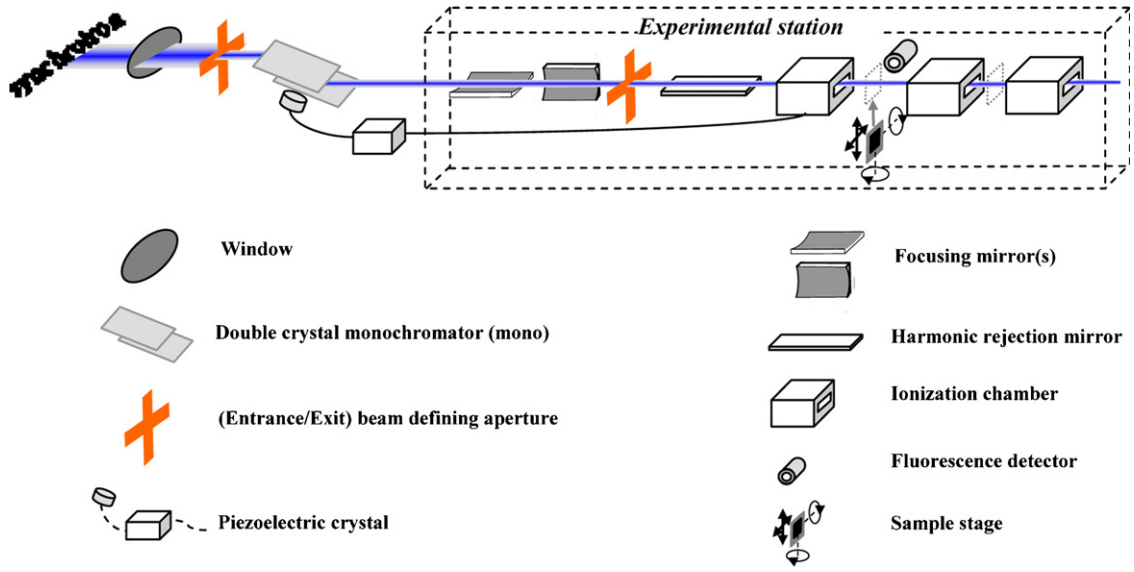

Fig. 46. The outlay of an XAS experimental setup showing the typical components in the beamline and in the experimental station.

called "tender" X-rays. Soft X-rays are very useful for the study of materials in general, and battery materials in particular. As an example of how XAS provides intimate details of the electronic structure of active materials in Li batteries, we will consider the prototypical layered cathode compound $LiCoO_2$. Oxygen *K*-edge XAS spectra of $LiCoO_2$ will show a pre-edge corresponding to t_{2g}, and empty e_g states followed by empty states that also appear in metal *K*-edge spectra (Fig. 48). At a slightly higher soft X-ray energy using the same synchrotron beamline, the complementary metal *L*-edge provides *d* orbital information. Therefore, soft X-ray XAS is a unique combined probe of multiple relevant orbitals. In Li batteries, the most common non-lithium metals found are the 3d transition metals (3d-TM, henceforth). The *K*-edge XAS of 3d-TMs probes their fully empty 4sp orbitals (Fig. 48).

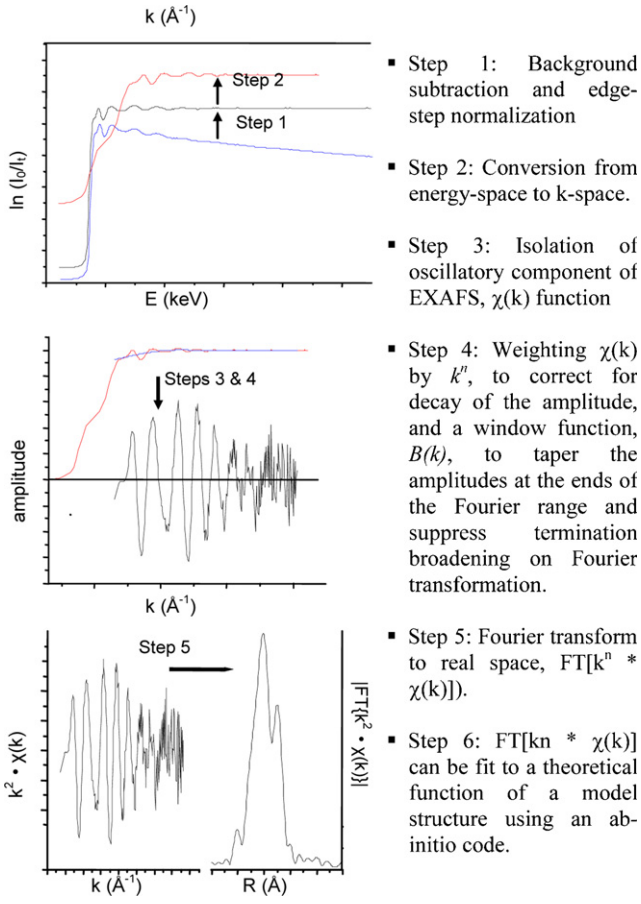

- Step 1: Background subtraction and edge-step normalization
- Step 2: Conversion from energy-space to k-space.
- Step 3: Isolation of oscillatory component of EXAFS, χ(k) function
- Step 4: Weighting χ(k) by k^n, to correct for decay of the amplitude, and a window function, *B(k)*, to taper the amplitudes at the ends of the Fourier range and suppress termination broadening on Fourier transformation.
- Step 5: Fourier transform to real space, FT[k^n * χ(k)]).
- Step 6: FT[kn * χ(k)] can be fit to a theoretical function of a model structure using an ab-initio code.

Fig. 47. The data manipulation steps to convert energy-space XAS data to k- and R-space data.

Since these orbitals are highly sensitive to the oxidation state of the TM ions, we can observe the shifts in the edge to follow *in situ* the changes in their local electronic structure as shown in Fig. 49(a) and (b). Also, the extended X-ray absorption fine structure (EXAFS) can be Fourier transformed to provide the partial radial distribution function, i.e., the probability distribution of atomic neighbors around the TM atoms.

These are three specific advantages of soft X-rays for XAS of Li battery materials:

Capability to probe meaningful final states: At these energies the transitions allowed by dipole selection rule to empty 2p and 3d states of O 3d transition metals (M) are in within measurement range. By probing those states directly, one can identify changes in the M–O chemical bond (Fig. 48).

More surface sensitive: When reviewing characterization tools for nanostructured electrode materials, particular attention should be paid to the relative surface sensitivities of various options. For XAS measured in electron yield mode, the IMFP of the Auger electrons is low compared to that for higher energy transitions, if available. For example, in $LiCoO_2$, one has the option of conducting a higher energy *K*-edge XAS (Co 1s → 4p) using hard X-rays, or a lower energy Co L-edge (Co 2p → 3d) using soft X-rays (Fig. 48). In the former, the IMFP of the Auger electrons is ~20 Å, while in the latter, the IMFP is ~4.5 Å. Choosing the soft X-ray option ensures the information is coming mainly from the top unit cell, as opposed to the top five unit cells that would be reported using the hard X-rays.

Higher energy resolution: The core hole lifetime (Δt) for an electron transition is inversely proportional to the uncertainty in the transition energy (ΔE) due to Heisenberg uncertainly principle. Since the core-hole lifetime is inversely related to the transition energy, the soft X-ray transitions will have narrower ΔE. In other words, soft X-ray spectra naturally have better energy resolution than corresponding hard X-ray spectra.

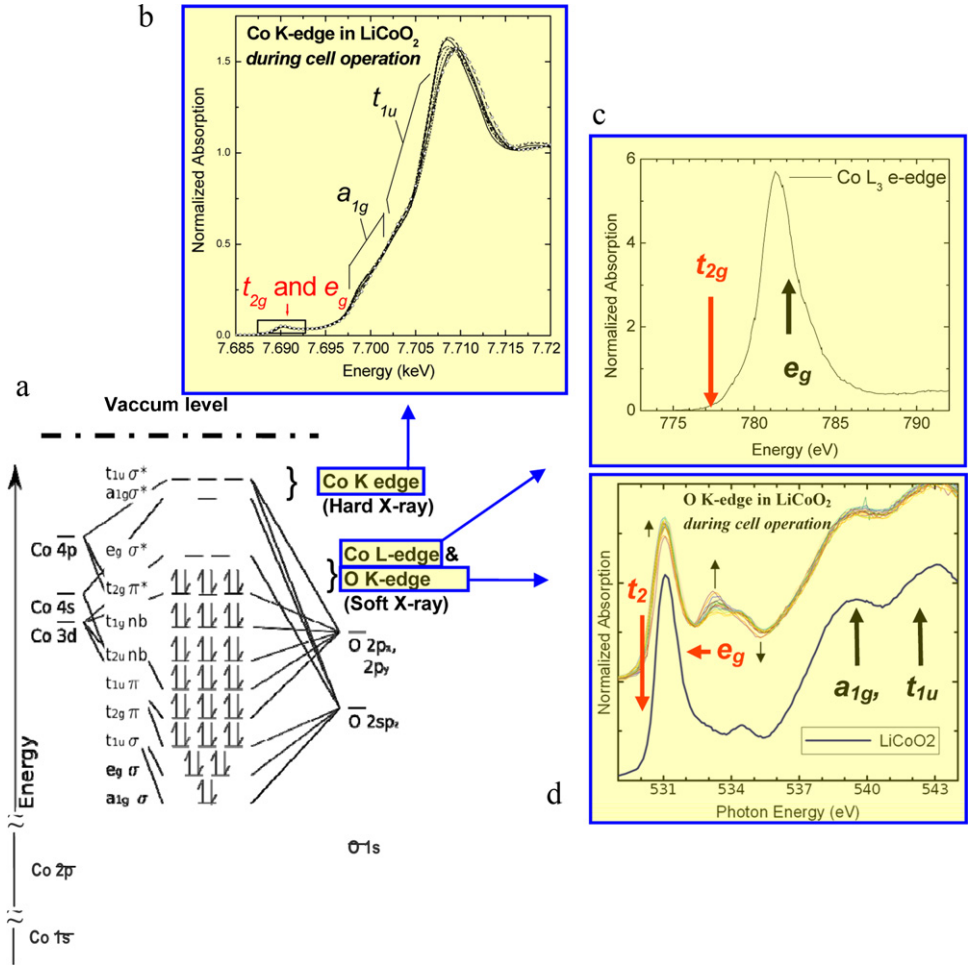

Fig. 48. Relationship between (a) the molecular orbital diagram for $LiCoO_2$ and the specific MOs that are probed by (b) Co K-edge, (c) Co L-edge and (d) O K-edge.

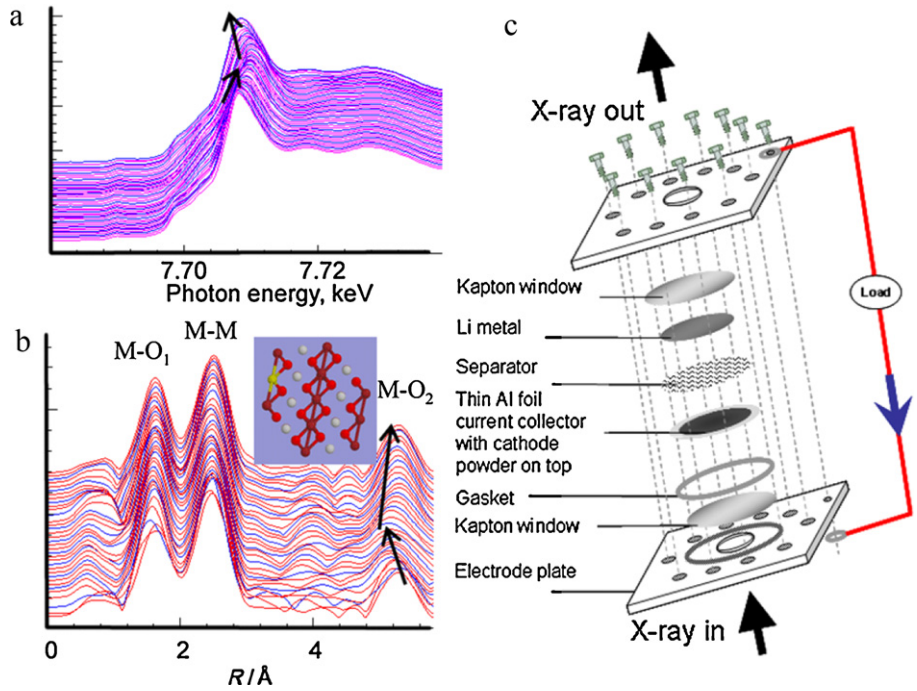

Fig. 49. *In situ* measurements of (a) XANES (showing oxidation and reduction behavior) and (b) EXAFS (providing the local atomic structure around Co atoms in $LiCoO_2$) during the charge (lower arrow in a, b) a discharge (upper arrow in a, b) of $LiCoO_2$-based batteries. (c) A schematic of a transmission *in situ* XAS cell. Rather than nylon screws, standard crimped coin cells or pouch cells can also be used.

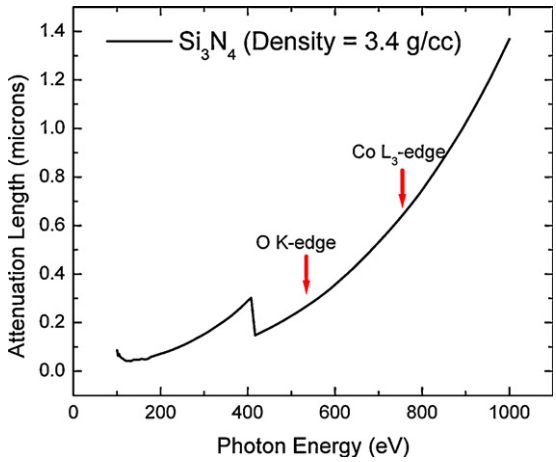

Fig. 50. The attenuation length of photons through Si_3N_4, a candidate window material for a soft X-ray *in situ* cell. An effective window material should be limited to a thickness of only a few hundred nanometers. The plot was calculated using the well-known Henke tables [268].

An *in situ* cell for soft-X-ray studies needs to meet some critical design challenges. Using a liquid electrolyte requires an X-ray window that can mechanically maintain a hermetic seal barrier against a pressure differential between the liquid (electrolyte) inside and vacuum (soft X-ray XAS chamber) outside. Because of the low attenuation length of soft X-ray photons through solid-state materials, the window to a soft X-ray cell has to be sufficiently thin. At soft X-ray energies, even Be, the potential metal window/current-collector material with the lowest absorption, has an absorption length of less than a micron. At this thickness, Be would have difficulty in meeting the pressure differential challenge. Harder materials such as Si_3N_4 are even more X-ray absorptive (Fig. 50).

Due to these challenges, no research group has been able to perform *in situ* XAS of active materials in Li batteries using soft X-rays until a recent breakthrough by Alamgir and co-workers [269]. The solution they devised was to replace the liquid electrolyte with a fast Li conducting solid electrolyte. The resulting "naked battery" (Fig. 51) is free of packaging and window materials. Accordingly, the interfaces can be investigated through direct XAS spectroscopy on either electrode face or potentially across the profile of the battery.

6.2.2. Hard X-ray XAS

There are two inherent advantages of using hard X-rays for XAS studies.

Higher energy resolution: As shown in Section 6.1.1 for the EDXRD cell, hard X-rays are penetrative and, thus, *in situ* cells can be designed even for the soft end of the hard X-ray range. This allows one probe even early transition metals such as vanadium in a transmission cell similar to the one shown in Fig. 49.

Access to wide bandwidth EXAFS: In the hard X-ray regime, the electron transitions are well-separated in energy, which generally translates to a wide bandwidth of EXAFS information. While Co L-edge EXAFS is not easily obtained since the EXAFS from L3 and L2 transitions overlap, except for the narrow energy range between the two transitions, Co *K*-edge in $LiCoO_2$ does not have interference from other higher energy transitions. In a $Li[Co,Ni]O_2$ cathode, the Ni *K*-edge is sufficiently removed from the Co *K*-edge so that neither one interferes with the other.

As an example of the rich local structural information obtainable from XAS using hard X-rays, Fig. 49(a) and (b) shows the changes in the XANES and the EXAFS, respectively, during the charge/discharge of a $LiCoO_2$-based cell [263]. Fig. 49(c) shows a schematic *in situ* cell design that will work for hard X-ray XAS. Each component of the cell needs to be designed to provide sufficient transmission through the cell. As a practical guide, this design constraint can be achieved by ensuring that each component, that the X-rays penetrate through, is not thicker than a single absorption length $\mu(E)$ for the respective XAS energy range. The XANES in Fig. 49(a) shows the Co K-edge position shift to higher binding energy during charging, since Co gets oxidized to compensate for the excess local negative charge remaining as Li is removed and consequently greater energy is required to photoionize a higher-valency Co. Meanwhile, the R-space data obtained from the EXAFS region, Fig. 49(b), shows the first two peaks corresponding to the M–O and the M–M bonds, respectively. The 3rd peak, $M\text{-}O_2$ corresponds to the oxygen atoms from the next plane. The fact that $M\text{–}O_1$ and M–M are very stable while $M\text{–}O_2$ exhibits contraction and expansion during charge and discharge, respectively, points to the in-plane rigidity and the interplanar "breathing" during the cycling of $Li_{(1-x)}CoO_2$. One can see from this example that *in situ* XAS is a powerful tool for examining atomistic mechanisms in Li and Li-air batteries.

6.2.3. Reaction dynamics

The reaction at a battery electrode, in the first-order approximation, is the equilibration of the electrode atomic environment to

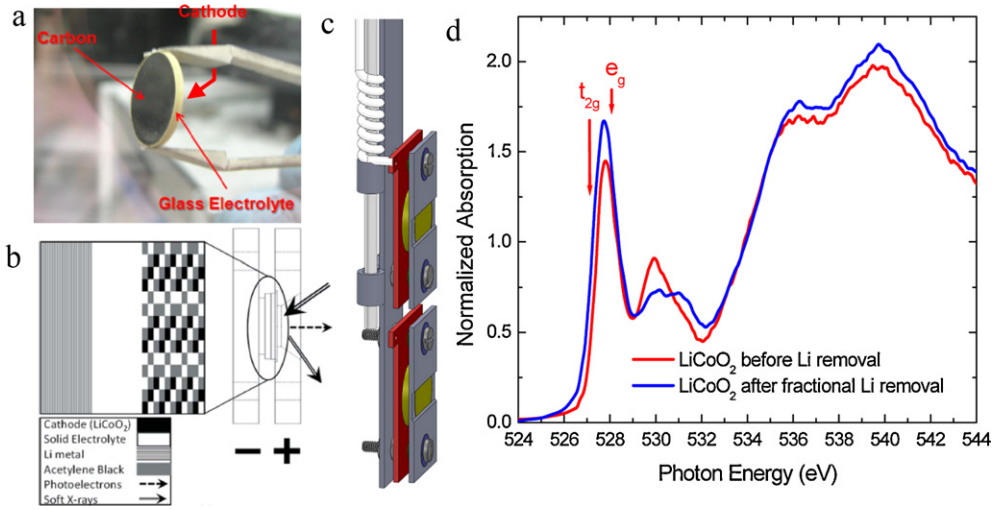

Fig. 51. (a) All solid-state "naked battery" designed by the Alamgir's group for *in situ* studies, (b) the schematic of its composite structure, reproduced with permission from [269], (c) the spectroscopic cell assembly and (d) spectra acquired *in situ* from O K-edge (right) using this cell.

the Nernst potential in the presence or absence of an external bias. The equilibrium reactions are diffusion limited and take place in the 10^2 ms to 10^2 s timescale, depending on the diffusing species and the diffusion length. Measurement of near-equilibrium atomic and electronic structure in electrochemical devices such as Li batteries, therefore, does not require a time resolution higher than a millisecond.

Kinetics of Li titration and reverse titration experiments can be monitored by speciation at high time resolution using XAS. If only the XANES portion of the XAS spectra is scanned, unique spectra can be obtained at a rate of one scan per minute routinely, and as rapidly as in 10 s of milliseconds at quick-XAFS beamlines (e.g., at X18B of the NSLS). Spectra from such experiments must be deconstructed to reveal the significant common components between them and the relative weights of each component. Reaction kinetics can then be obtained by following the rate of change of the weights of the deconstructed components.

6.2.3.1. Linear combination analysis. When a set of spectra represents a single reaction pathway, that is, only one mechanism is present for converting the reactants to products, as is the case on a voltage "plateau" in the charge/discharge curves of Li batteries, then each XAS spectrum can be represented as a linear combination of the two end spectra of the dataset. Identification of the electronic structure (such as oxidation state) and the atomic structure (local symmetry and coordination) of the end structure can be done by "fingerprinting" spectral signatures with those of reference compounds; it should be noted that since XANES spectra are simultaneously sensitive to oxidation state, bond length and local symmetry, care must be taken to distinguish between these effects. Grant Bunker Simon Bare provide good online references on this issue. Linear component analysis (LCA) is an analytical tool that can be used to investigate the kinetics of intercalation or conversion reactions in Li batteries.

LCA should be carried out on the XANES region as well as the EXAFS region (post Fourier transformed to R-space) to obtain complementary information on chemical bonding and the atomic structure changes during the reaction. Leifer et al. shows very convincingly the conversion reaction during the lithiation of $Ag_2V_4O_{11}$ (SVO) to $Li_xAg_2V_4O_{11}$ [270]. It can be clearly seen in Fig. 52 that the introduction of Li into SVO begins to convert it to face center cubic (FCC) Ag, with the conversion partly completed by 0.72Li/SVO and fully completed by 2.13Li/SVO. The relatively lower amplitudes at the nearest Ag–Ag peak for both he $Li_{2.13}Ag_2V_4O_{11}$ and $Li_{5.59}Ag_2V_4O_{11}$ compounds, compared to that

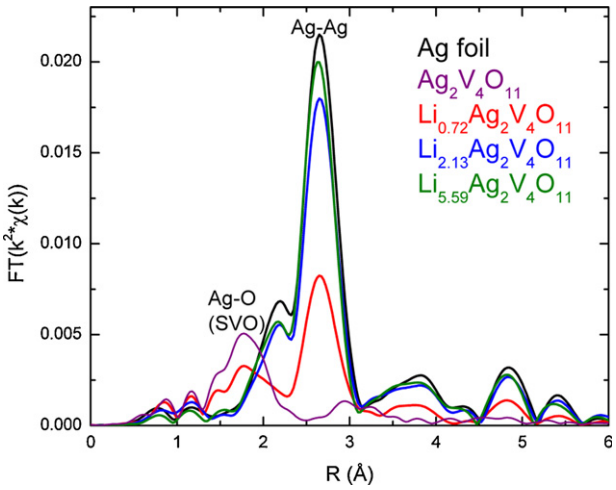

Fig. 52. All The change in the Ag nearest neighbor environment as a function of Li intercalation [270].
Reproduced by permission of The Electrochemical Society.

of bulk Ag (Ag foil), is due to the nanoscale size of the phase segregated FCC Ag.

6.2.3.2. Isosbestic points. An *in situ* XAS dataset for a single reaction pathway is marked by isosbestic or crossover points in the X-ray absorption function. Conversely, the presence of isosbestic points is a quick indication of the fact that the reaction involving the particular element being probed by XAS has proceeded through a single reaction path. Isosbestic points result from the fact that if the reactants and the products have equal light absorption coefficient at a specific energy (i.e. $\alpha_{E1}A = \alpha_{E1}B = \alpha_{E1}$), and the analytical concentration of reactants plus products remains constant, then the absorption coefficient remains the same at any stage of the reaction. As a corollary, it should be mentioned that a true single reaction would mean that every intersection point in the dataset should be isosbestic. The simultaneous presence of isosbestic and non-isosbestic intersections means that the spectra are dominated by a single reaction pathway, but are still affected by the presence of a minor side reaction. Fig. 53 illustrates this phenomena very well with the Ni XAS data during the delithiation of $Li[NiMn]O_2$ cathodes. Fig. 53(a) shows the spectra during the first charge where there is an irreversible side reaction present, while Fig. 53(b) shows isosbestic points since the irreversible reaction is now absent.

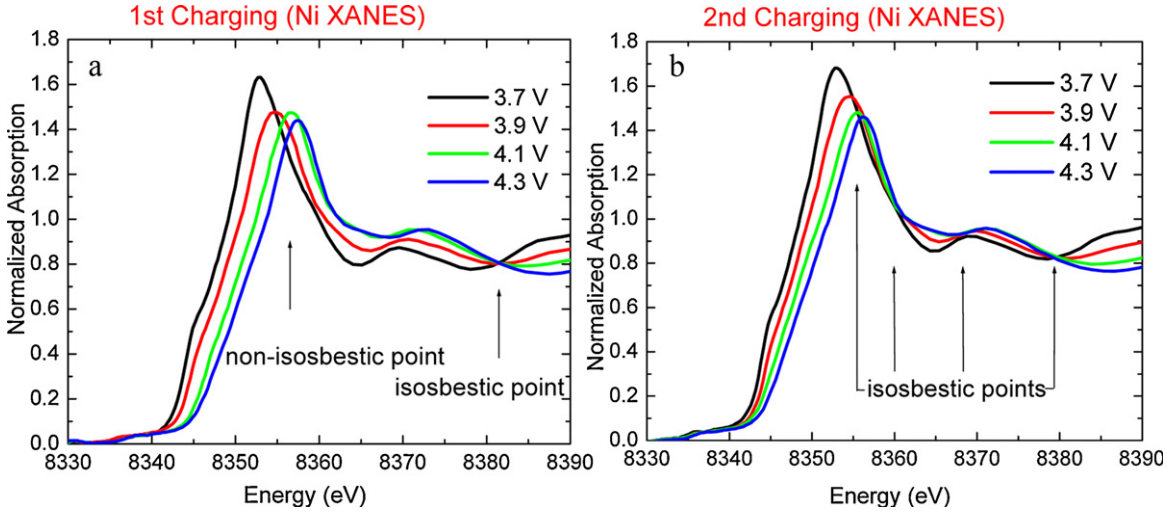

Fig. 53. Ni K-edge XANES during charging in the (a) first, and (b) second cycles.

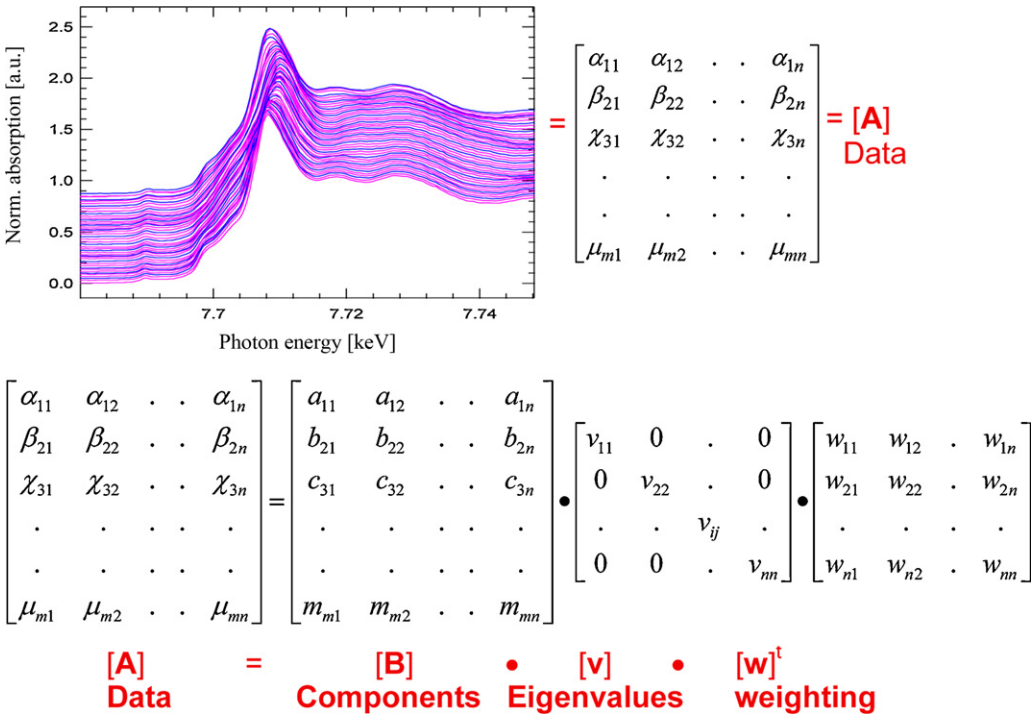

Fig. 54. PCA formulation for the deconstruction of a set of XAS data.

6.2.3.3. Principal component analysis. For *in situ* XAS datasets during charge/discharge reactions in Li batteries where single reaction paths are not self-evident (no isosbestic points in the XANES region, for example) principal component analysis (PCA) can be used as a fully objective analytical tool. PCA provides an answer to the question of how many minimum spectral components are necessary to reconstruct any spectrum in the dataset. PCA, therefore, indicates how many independent chemical species (with unique chemical signatures) are contained in the overall reaction.

PCA is based on the singular value decomposition (SVD) algorithm in linear algebra. SVD is based on the theorem that any $m \times n$ matrix A, with m rows and n columns, can be represented as a product of $m \times n$ column-orthogonal matrix B, an $n \times n$ diagonal matrix V with elements that are positive or zero, and the transpose of an n x n orthogonal matrix w. as shown in Fig. 54. For further details readers are referred to the work of Ressler [271] and references therein. PCA can be applied to a set of XAS spectra since such a dataset can be expressed as an m x n matrix. In the analysis of a set of XANES spectra, the column vector (α_{1j}, β_{2j}, χ_{3j}, ..., μ_{mj}), where $1 \leq j \geq n$, represents one XANES spectrum out of the total set of n spectra. The output matrix B has n columns, but the ones that are important are those for which $v_{ij} \neq 0$.

While PCA has been applied to the analysis of XAS datasets, specifically in the area of catalysis, it is an analytical technique that can be applied to any spectroscopic technique. In the study of Li batteries, however, PCA is currently underutilized, with only a single infrared [272] and two XAS [263,273] studies evidenced by a literature survey.

In the first of the two XAS works cited, Alamgir and others show a very effective use of PCA in an *in situ* study of the delithiation of a thin-film $LiCoO_2$-based Li battery. They infer that two separate reactions occur during delithiation, which allows them to rule out Co oxidation as the only charge compensation reaction occurring during the charging of the battery. Combining the PCA results with the analysis of the real-space data allowed them to pinpoint the reactions to be associated with electron hole formation at Co and O sites. Fig. 55(a) shows the $|FT\{\chi'(k)|$ functions from the hard X-ray induced Co K-edge spectra, which are proportional to the radial distribution function around Co atoms, for $Li_{(1-x)}CoO_2$ with $0.12 \leq x \leq 0.7$. One can clearly see changes occurring at the Co–O and Co–Co coordination shells as represented by their respective distances in Fig. 55(b), but Alamgir et al. were the first to indicate the presence of oxygen holes (responsible for the oxygen neighbor 2 in Fig. 55(b)) from *in situ* data. Future XAS work on reactions in Li and Li-air batteries look very promising using traditional (edge shifts, fingerprinting, R-space fitting) as well as non-traditional (LCA, isosbesticity, and PCA) analytical schemes.

6.3. Nuclear magnetic resonance (NMR)

Nuclear magnetic resonance (NMR) is a powerful tool to discriminate between the different chemical states of lithium and carbon species in batteries. Since most synchrotron beamlines are not designed to access Li core electron emissions, making Li K-edge XAS a difficult experiment to conduct. ^{7}Li NMR, in particular, is a powerful complementary chemical probe to XAS. When placed in a magnetic field, NMR active nuclei (such as ^{1}H, ^{13}C or ^{7}Li) absorb at their respective characteristic electromagnetic frequencies. The resonant frequency, absorption energy, and signal intensity are proportional to the strength of the magnetic field. If the frequency of the line of interest is ν (in Hz), and the frequency of the line from the reference compound is ν_{REF}, then the chemical shift, δ, is defined as:

$$\frac{(\nu - \nu_{REF})}{\nu_{REF}}$$

For H, C and Si NMR, an accepted reference is tetramethylsilane, and for Li NMR, LiCl is often used. Because the frequency shifts are small relative to the resonance frequencies, chemical shifts are reported in parts per million: $\delta_{PPM} = \delta \times 10^6$.

Due to the high natural abundance of ^{7}Li isotopes (more than 90% in natural sources), isotopic substitution is not required to

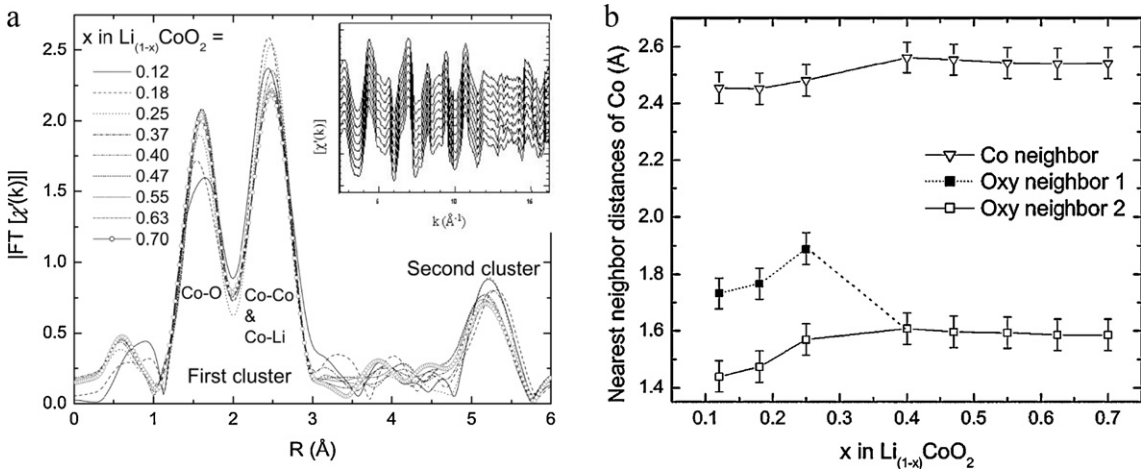

Fig. 55. (a) Changes in the local atomic structure with *x*. Two clusters of interatomic distances are apparent, at 1–3 Å and above 4.75 Å. The inset shows the $\chi(k)k^2$ functions prior to Fourier transformation. (b) Peak positions of the Gaussians used to fit the peaks in the first cluster of the $|FT\{\chi'(k)|$ function [263]. Reproduced by permission of The Electrochemical Society.

increase signal strength. The ^{6}Li isotopes do not suffer from the same quadropolar interaction as ^{7}Li, resulting in narrow peak-shapes and better resolution. However, this comes at the cost of lower signal due to its low abundance. In the case of carbon, the abundant isotope ^{12}C has zero net spin and is consequently NMR inactive, whereas the active ^{13}C isotope is only present in about 1.1% natural abundance. Adequate information using ^{13}C NMR is attained by signal averaging over longer detection time or by isotopic substitution into the active materials.

The sensitivity of NMR to the local chemical bond comes from electron-nuclear coupling. When the coupling is with closed shells the term "chemical shift" is often used, whereas, when the interaction is with conduction electrons, as in metals, the term "Knight shift" is used. Lineshifts in Li NMR are, therefore, often referred to as Knight shifts.

The lateral spatial resolution in standard NMR is in the range of millimeters. It is therefore not well-suited for interface study by rastering the anode-to-cathode cross section of conventional or 3D Li batteries. In special cases, NMR can be done in a magnetic resonance imaging (MRI) mode where the spatial resolution can drop to about 10 s of microns. The depth resolution is determined by the so-called skin depth, which measures the extent of penetration of the radio frequency electromagnetic probe into the sample:

$$d = \frac{1}{\sqrt{\mu_0 \pi}} \sqrt{\frac{\rho}{\mu_r f}}$$

where μ_0 is the permeability of vacuum, μ_r is the relative permeability of the sample, ρ is the resistivity of the metal for Li and f is the frequency of the applied radio frequency field [269]. For Li, the calculated skin depth is about 15 μm. For nanostructured materials in Li batteries, lateral and depth resolution of more than 10 μm can be inadequate. However, when sample homogeneity is expected at the 10 μm scale, the spatial resolution offered by NMR becomes useful.

NMR spectroscopy can also be used to measure the coefficient of self-diffusion, for the NMR active nuclei. Diffusion rates are measured by NMR using gradient pulses and the technique works at mM concentration. This measurement is of particular relevance to Li transport in active components of Li batteries. Other causes of transport such as convection are typically present; so care must be taken to avoid the sources of convection, such as temperature gradients.

Multiple researchers have used *ex situ* NMR to study Li battery components, usually in conjunction with other characterization techniques [274–279]. However, following the original work of Gerald and co-workers [280], who appear to be first to use *in situ* ^{7}Li NMR to study Li insertion in anode materials for Li batteries in 2000 (Fig. 56), there are only a handful of examples of *in situ* NMR used to non-invasively characterize internal reactions in Li batteries [281–285].

Since the acquisition time for the ^{7}Li signal can be much faster than the time for a typical charge–discharge cycle, due to the high sensitivity of ^{7}Li NMR, spectral snapshots at suitable time intervals can be used to analyze the structural changes of the active material at various states-of-charge. When carried out *in situ* during electrochemical cycling, Li NMR spectroscopy is a non-invasive method for investigating the structural changes occurring in electrode materials, like XAS and Raman as we will see in the next section. Vital information that can be obtained from NMR for Li batteries is summarized in Table 4.

6.4. Raman spectroscopy

Among the local probes, Raman spectroscopy is one of the most versatile. Like XAS, speciation is possible because the Raman signal originates from the characteristic vibrational frequencies of materials. The vibrational frequencies are determined by bond distance, bond strength and coordination of the nearest atomic neighbors. Raman, therefore, provides a very sensitive tool to detect structural variations at the atomic level. Unlike XAS, however, the Raman signal does not originate from internal emissions of atoms and consequently does not contain unique signatures of the atoms involved. Furthermore, structural properties such as bond distance, bond angle, and coordination are not directly available from the Raman signatures, but they can be elicited through careful fitting to model structures and sound elimination of alternative models. Still, Raman spectroscopy has become a standard method for characterizing bulk materials, molecules, thin films, and surfaces [286,287]. Of the relatively few surface analysis methods available for *in situ* measurements, Raman spectroscopy is one of the most flexible, as it has a large window of operating conditions and a wide range of surface species that can be probed and mapped, including oxygen [288,289], sulfur [290], carbon [291], and hydrocarbons [292]. A significant number of Raman studies can be found in the literature applied to Li batteries, including studies on changes in bond lengths, bond angles, coordination, Li dynamics, and ordering. For an excellent review of Raman studies applied to Li batteries, the readers are directed to the paper by Baddour-Hadjean and Pereira-Ramos [293].

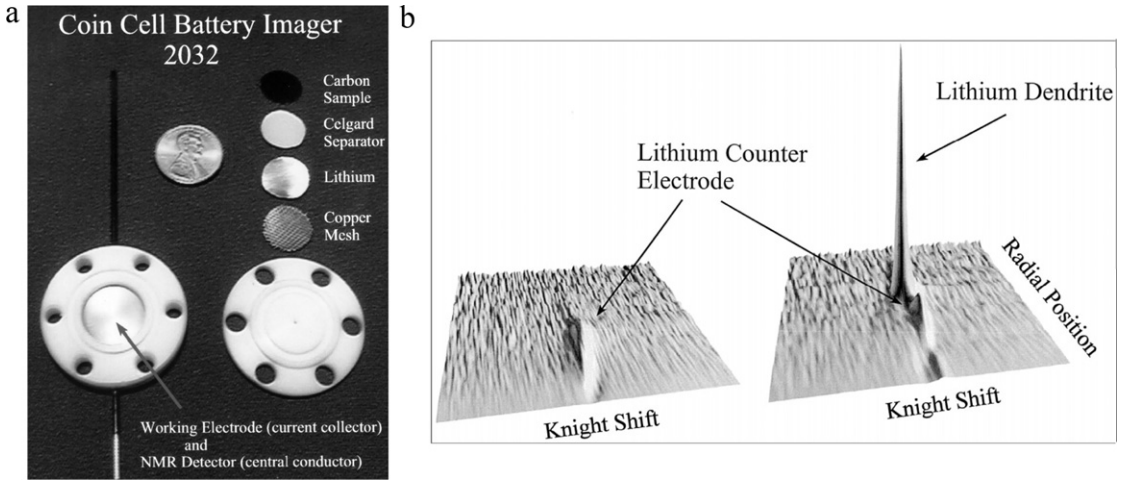

Fig. 56. (a) Photograph of the coin cell battery imager. (b) ^{7}Li NMR images of the counter electrode and the lithium dendrites that were formed on a hard carbon electrode in the presence of a lithium counter electrode before (b, left) and after (b, right) passing current through the cell [280].
Copyright 2000, with permission from Elsevier.

Table 4
Vital information that can be obtained from NMR for Li batteries.

Chemical structure	Li and C sensitivity	Diffusion of active nuclei	Spatial resolution
In NMR, the measured chemical shift is related to the local chemical structure around the atoms with the resonant nuclei. Species can be identified by proper referencing and direct fingerprinting.	Lithium and carbon sensitivity makes NMR an important technique for the study of Li battery anodes. While carbon-specific information can be easily obtained from XAS, the same is not true for lithium. NMR and XAS are, therefore, very complementary.	The self-diffusion component to Li transport, especially in electrolytes, is an important property in Li batteries. This self-diffusion coefficient can be measured with NMR. Care must be taken to avoid misleading data from convection transport through temperature gradients.	In a typical setup, the lateral spatial resolution of NMR is poor. In imaging mode setup, akin to an MRI, lateral resolution of 10 s of μm can be obtained. Depth resolution is determined by the "skin depth" and is in the order of 10 μm.

The Raman process: Raman spectroscopy is currently a standard research technique; however, a quick review of the Raman process would be useful for subsequent discussions. A photon of light from the near-visible region of the spectrum can induce vibrations in a molecule through either absorption or scattering of the photon. The former case occurs when the energy of the incident photon is equal to that of the energy difference between two oscillatory states of the molecule, and when the transition between the states involves a change in the molecule's dipole moment. This is the case for infrared absorption. Alternatively, photons can excite the molecule to a virtual state lower in energy than a real electronic transition (Fig. 57).

The process could be elastic, or Rayleigh scattering, when the photon is scattered without any change in the atomic coordinates of the molecule and in the frequency of the incident photon. For a very small fraction of light, however, for about one in every 10 million, energy is transferred between the molecule and the incident photon. The energy of the inelastically scattered photons can either be shifted slightly higher or slightly lower than that of the incident photons. This inelastic scattering is called the Raman effect, with the Raman shift described as:

$$\upsilon_{\text{Raman}} = \upsilon_0 - \upsilon_{\text{vib}}$$

that is, frequency of the original photon shifted by the frequency of molecular vibration.

The red-shifted scattered photon is called the Stokes Raman while the blue-shifted photon is called the anti-Stokes Raman. Since the anti-Stokes scattering has the low-probability starting condition of a molecule in a vibrationally excited state at the time of the photon scattering, it is always a weaker signal than the Stokes scattering where the molecule starts at the highly populated ground state.

Advantages of Raman spectroscopy: The Raman technique has several characteristics very well suited to the study of electrode materials. First, the analysis is nondestructive under typical experimental conditions. A Raman microscope can focus the laser

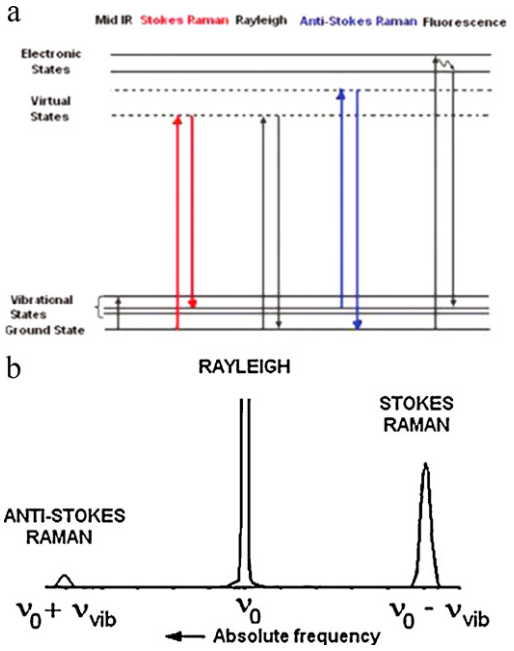

Fig. 57. (a) Energy level diagram for different processes. (b) Raman and Rayleigh scattering of excitation at a frequency ν_0. The molecular vibration in the sample is of a frequency ν_{vib}.
Reprinted with permission from [293]. Copyright 2010 American Chemical Society.

Table 5
Vital information that can be obtained from Raman for Li batteries.

Species specificity	Bond strength	Local information	Spatial resolution
While overlaps do exist between unrelated cases, the vibrational frequency of a Raman excitation is often unique to a particular molecular unit. Species can be identified by proper referencing and direct fingerprinting.	Since Raman proves the vibrational states of molecular units, its signal directly relates to the force constants of the bonds involved. Raman, therefore, provides vital information on the strength of these bonds.	Raman is a local probe since the Raman excitations are due to local vibrational states. Therefore, information on bond length, coordination, bond angle are all imbedded in the Raman signal and can be elicited with proper modeling	The ability to move a micron sized focal spot through different focal planes within the material allows Raman to be a highly versatile technique with micron-range lateral as well as depth resolution.

beam source down to a volume of 1 μm^3 in air. It can be operated in a confocal mode by using an aperture at its back focal plane, thereby improving its lateral and axial spatial resolution. By acquiring spectra as the laser focus is moved incrementally deeper into a transparent sample, nondestructive depth profiling can be carried out.

Second, the samples can be studied under *in situ* conditions through optically transparent windows, even in the presence of strong IR absorbers such as H_2O, CO_2, and SiO_2. Focusing of the probe size allows the technique to characterize the heterogeneity of the electrode materials in batteries at the micron scale. Therefore, this property is very useful for the study of Li batteries, since each functional component is typically a composite of Li storage material mixed with binder and conductive carbon materials. Micro-Raman has been effectively used for studying the structural properties of carbonaceous materials [294].

Third, like XAS, Raman spectroscopy can distinguish between the various forms of carbon due to the influence of bonding on the vibrational frequencies. Carbon with sp^3-type bonding, exhibited in diamond, has a distinct Raman signature compared to graphitic carbon with sp^2-type bonding [295]. Taking a closer look at graphite, for example, we note that the hexagonal structure is in the D_h space group, with its vibrational modes represented by the following irreducible representation: $A_{2u} + 2B_{2g} + E_{1u} + 2E_{2g}$. Here the E_{2g} mode is the only one that is Raman active and corresponds to the in-plane vibrations of the carbon atoms. Following this E_{2g} band, lithium intercalation into graphite was investigated *in situ* (Fig. 58) by Huang and Frech in their highly cited work in 1998 [296].

There is a plethora of literature on *ex situ* and *in situ* Raman studies of cathode compounds. As examples, one finds work on lithium–cobalt–nickel [297–299], $LiMn_2O_4$ [300], polycrystalline V_2O_5 films [301–306], and titanium oxide spinels [307–312]. Here the authors direct the readers to the review by Baddour-Hadjean and Pereira-Ramos and the references therein for further examples [293].

Raman spectroscopy provides a set of information vital to the study of Li batteries. Table 5 summarizes its specific advantages:

The frontier of *in situ* measurements for Li batteries is not only to measure the reaction and chemical evolution of species within the active materials during voltage cycling, but also to measure these in extreme gas and temperature environments. Using the solid-state battery design shown in Section 6.2.1, an open cell could be placed in an electrochemical enviro-chamber as shown in Fig. 59, where the cell could be exposed to heat (to below the T_g of the glass electrolyte) and to various gas environments. In the case of Li-air battery studies, the air electrodes could be examined under practical operating conditions to study the effect of contaminations from air or other gas impurities. When performed simultaneously alongside with other electrochemical measurements, *in situ* Raman spectroscopy allows direct correlation between the electrochemical performance of the cell and the electrode surface structure and composition, providing

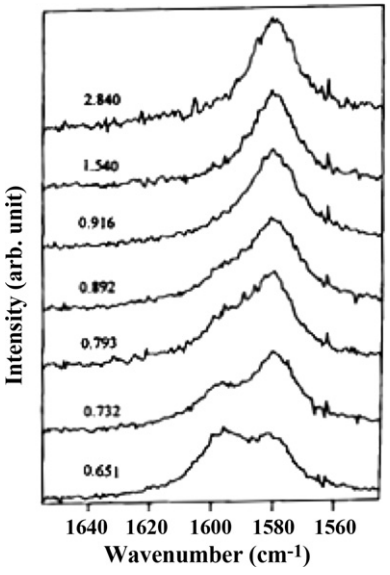

Fig. 58. *In situ* Raman of graphite in a $LiClO_4$ EC/DMC solution during the first intercalation between 0.586 and 0.089 V [296].
Reproduced by permission of The Electrochemical Society.

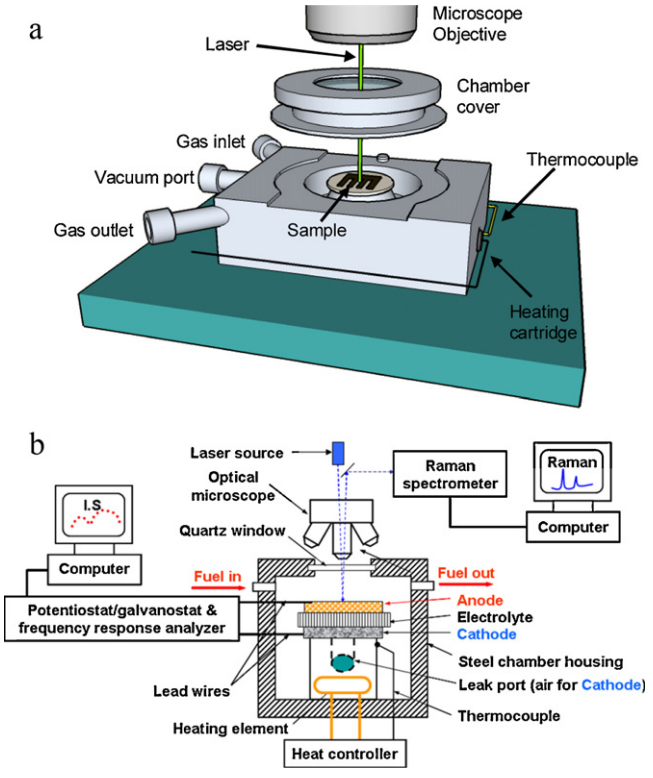

Fig. 59. (a) 3D drawing and (b) 2D schematic of the electrochemical enviro-chamber with the optical microscope and X–Y–Z motorized stage designed by Liu's group for *in situ* Raman studies [313]. The stage moves in 0.02 mm increments and spectra can be collected from 1 μm diameter spot.

information vital to gaining insight into the mechanism of electrode processes.

6.5. Comparison of information depths for different measurements

The "information depth" refers to the typical depth within the material where structural and chemical information can be obtained from an experimental measurement. The concept of an average information depth is critical to designing characterization experiments. Here we discuss the principal criteria that determine the information depth for XAS, NMR, and Raman in the context of Li battery materials.

XAS: In transmission mode XAS, the X-ray penetrates through the thickness of the active materials as well as the remainder of the cell stack. In such a case, the thickness of the sample is the information depth of the technique. On the other hand, using fluorescence yield mode, the information depth is restricted to about two to four absorption lengths. For a typical cathode material, such as $LiMO_2$ (M = Mn, Co, and Ni), is in the order of 10–25 μm at the K-edge of M. Much shorter information depth can be obtained if one measures XAS using electron yield, where this depth is restricted to the IMFP of the electrons. Using electron yield mode of detection, the information depth for $LiMO_2$ is restricted to tens of nm at the M K-edge and to a few nanometers at the O K-edge.

NMR: Information depth in NMR is determined by the so-called skin depth δ, which is conceptually similar to the information depth. Skin depth in NMR is given by $\delta = (1/\pi\mu_0)^{1/2}(\rho/\mu_x f)^{1/2}$ where μ_0 and μ_x are the permitivities of vacuum and the material, respectively, ρ is the resistivity and f is the Larmor frequency, the frequency of the applied radiofrequency wave [281–285]. For Li, the skin depth is estimated, therefore, to be in the order of 10 μm.

Raman: In opaque materials, the information depth for Raman is determined by the electrical conductivity, σ, the magnetic permeability, μ, and the wavelength, λ, of the source. The skin-depth δ, has a form very similar to that of NMR (which is not surprising since they both involve the penetration of EM waves) and is given by the relationship $\delta = (2\lambda/\sigma\mu)^{1/2}$ [293]. Typically, δ ranges from approximately 30–300 nm.

6.6. Future directions of in situ characterization of Li batteries

We have explored the rich information available from *in situ* measurements especially when using techniques with species-specificity. While each of the techniques described here has specific advantages, it is XAS that provides the most detailed structural information. The XANES region probes the element-specific electronic structure of the active materials in Li batteries just above the Fermi level, which provides direct information about subtle changes in chemical bonding. At the same time, local atomic structure, in the form of a partial radial distribution function, is available from the EXAFS region. With the high brightness of a synchrotron source and a creative *in situ* cell design, XAS is a powerful technique for fundamental investigations into materials for Li batteries. Further, significant improvements in the usefulness of XAS are expected in the near future. For example, NSLS II, the replacement for the current NSLS is under construction and is projected to have XAS capable beamlines with a spot size of a few nanometers. Thus, a true synchrotron nanoscope can be envisioned that competes with scanning electron microscopes in terms of spatial resolution but has all the added benefits of a synchrotron.

Recent advances in high-pressure XPS are expected to translate to creative ways in which the near-surface (within a few nanometers) of a Li battery's functional parts will be studied under operating conditions. With higher flux X-ray sources, from new synchrotrons, this transition is all the more likely.

The future will hold more studies using the inelastic scattering of hard X-rays, compensating for the small cross section for these events with the advent of much brighter synchrotron sources. Core level emissions in low Z elements can occur through the inelastic scattering of hard X-rays and, thus, the chemistry of C and O species, for example, can be followed by passing hard X-rays in an out of a working Li battery. This is a process analogous to the core electron emissions from low-Z elements that occur through inelastic losses of fast electrons in an electron microscope, the basis for electron energy loss spectroscopy (EELS).

The spatial resolution and sensitivity of Raman spectroscopy are expected to be enhanced significantly in the future. In particular, the use of plasmonic coupling will become routine and allow the surface-enhanced Raman spectroscopy (SERS) technique to considerably increase the sensitivities needed for battery research. Further, tip-enhanced Raman spectroscopy (TERS) becomes possible when a Raman spectrometer is integrated with a scanning probe microscope (e.g., an AFM or a STM), dramatically enhancing the sensitivity and spatial resolution of Raman measurements and ideally suited for fundamental investigations of nanostructured electrode materials for future-generation lithium batteries.

7. Conclusions and outlook

The performance characteristics of the existing electrical energy storage devices greatly influence the energy efficiency, reliability, and commercial viability of several emerging technologies such as electric vehicles and smart grids. They also impact the portability and reliability of many portable electronics such as hand-held communication devices, computer, and cordless tools. Batteries are the most promising and accessible options for electric energy storage. Yet, the performances of the existing batteries are still far short of meeting the needs of these applications. The main scientific challenges are to achieve rational design of materials with desired properties, especially electrode materials with multi-functionality for enhanced rate capability (power density), high energy density, excellent dimensional stability and long cycling life, and dramatically reduced cost.

The preceding sections have provided ample examples of recent developments in Li-containing anodes, insertion compounds for Li-ion cathodes, and carbon-based oxygen-breathing cathodes for Li-air batteries. A wide variety of unique nanostructures and nano-architectures have been developed to dramatically accelerate the charge and mass transfer processes relevant to battery operation while improving the mechanical robustness and tolerance to stresses and strains induced by volume change. Further, surface modification using a nanometer-thick thin-film coating of proper materials is proven to be effective in further enhancing the catalytic and transport properties as well as stability against electrolyte and durability of electrode materials. Indeed, nano-structured electrode materials have demonstrated significantly improved performance (energy and power capability and cycling life) due mainly to high surface area, short diffusion length, a large number of active sites, and improved mechanical robustness. We believe that nanostructured materials will play an even more important role in redefining a new generation of batteries with dramatically better performance (higher energy and power density and longer cycling lifetime) than the existing ones to meet the increasingly stringent needs of emerging applications such as electric vehicles and smart grids.

While nano-structured electrodes have demonstrated enhanced performance in many specific aspects, it is still not clear how to best design or optimize a specific electrode structure to achieve optimal performance. The main difficulty is the lack of fundamental understanding of the mechanistic details about the

chemical and energy transformation processes associated with the operation of a battery. Often it involves a series of elementary charge and mass transfer processes along the surfaces, across the interfaces, and through bulk of some phases in a complex electrode. It has been very difficult to determine exactly which specific step is the rate-limiting step of the overall process. To date, for example, little is known about the mechanism and sequence of elementary steps associated with charge and mass transport processes, especially in the confined pores and channels of nanostructured electrodes. More fundamental studies are needed to correlate the electrochemical performance with the microscopic features (such as critical dimension, morphology, pore size and distribution) of nanostructured electrodes. Further, the functioning of these electrodes is often influenced by many opposing factors. For example, one nano-structure may greatly enhance the rate capability, but suffers from limited volumetric energy density due to high surface area and low packing density.

To unreal the detailed mechanism and the rate determining step of battery operation, it is necessary to follow the detailed changes in crystal structure, composition, and morphology of each phase as well as in electronic structure, charge and mass transport characteristics, and catalytic properties. The use of *in situ* characterization techniques, guided by multi-scale modeling and simulations, is vital to unraveling these detailed microscopic processes associated with the functioning of electrodes. These understanding are vital to achieving rational design of optimized nanostructures and nano-architectures for a new generation of batteries.

More exploration of novel architectures of electrode materials can be very rewarding. For example, arrays of vertically aligned nanowires or nanotubes are likely to be very promising when integrated with other high-capacity electrode materials. Another strategy is to create 3D, nano-architectured structures with interdigitated, pillared anodes and cathodes. Properly designed composite electrodes of desired architectures may maximize the advantages while minimize the shortcomings of each component, thus offering higher energy and power densities and longer cycling lifetime.

Among many approaches developed to create nanostructures, bio-inspired processes may offer some unique advantages. Materials found in nature, evolved over time in structure and functionality in response to a variety of demands from environments, often exhibit remarkable properties. Another notable feature of biological systems is their ability to assemble sophisticated, hierarchical structures with high precision at different length scales (ranging from nanometers to millimeters) and complexity far exceeding those of artificial architectures created by human. The use of a bio-inspired approach to design nanostructures and nano-architectures could create electrodes with properties that have never before been imagined. Major advances in design of new electrode structures hinge on breakthroughs in creation of unique nanostructures.

Proper surface modification of nanostructured electrodes is essential to effectively accelerating charge and mass transfer processes. Better insights into the electrochemical reactions and the roles of point defects in the nanoscale regime are required in order to achieve rational design of more effective surface modifications (or coatings) for high capacity and rate capability.

In addition, explorations of new materials and new strategies are needed to dramatically enhance the energy densities of existing systems. Recently, nanostructured sulfur and mesoporous carbon have emerged as promising cathode materials. A lithium–sulfur battery has theoretical energy density of 2500 Wh/kg and 2800 Wh/L, which are far greater than those of conventional lithium batteries. Yet, transforming the potential of these materials into a reality remains a grand challenge; unique nanostructures and nano-architectures are vital to overcoming these challenges.

While Li-ion batteries still offer the best performance among all existing battery systems, it is unlikely that they will be able to meet the increasingly stringent demands of emerging technologies, due primarily to their limited energy densities of the cathode materials. To dramatically increase the energy density, we must move away from these heavy cathode materials and figure out how to make use of oxygen from air through a Li-air battery, which has the potential to match the practical energy density of gasoline in transportation – sufficient for electric vehicle applications. The future of batteries depends on the creation of multifunctional electrode materials with unique nano-structures or nano-architecture for efficient use of oxygen in a reversible manner. There are a range of scientific and technical challenges that we must overcome to make Li-air batteries a reality.

In addition, Li-ion and Li-air batteries have to compete with other energy conversion and storage technologies such as fuel cells. It should be noted that fuel cell vehicles have already performed well in the over-300 mile range, but the cost of precious Pt-based catalysts is a critical bottleneck for commercialization. Therefore, more investigation should be conducted on non-precious electrodes and catalysts to develop cost-effective Li-ion and Li-air batteries. Substantial improvements in energy density and rate capability are required, respectively, for Li-ion and Li-air batteries to compete with fuel cells.

Finally, the availability and cost of materials, improved safety, and minimal environmental impacts are equally important as performance. The development of large-scale, low-cost fabrication strategies for nanomaterials with desirable performance is an important challenge in fabrication of battery materials for commercial applications.

Acknowledgements

This work was supported by the WCU program (R32-2008-000-20054-0) and the Converging Research Center Program (2010K000984) through the South Korean Ministry of Education, Science and Technology and by the HetroFoaM Center, an Energy Frontier Research Center funded by the U.S. Department of Energy (DOE), Office of Science, Office of Basic Energy Sciences (BES) under Award Number DE-SC0001061.

References

[1] G.-A. Nazri, G. Pistoia, Lithium Batteries Science and Technology, 1st ed., Springer, 2003.
[2] W.A.v. Schalkwijk, B. Scrosati, Advances in Lithium-Ion Batteries, 1st ed., Kluwer Academic/Plenum Publishers, 2002.
[3] R.A. Huggins, Advanced Batteries Materials Science Aspects, Springer, 2008.
[4] J.M. Tarascon, M. Armand, Nature 414 (2001) 359–367.
[5] M. Armand, J.M. Tarascon, Nature 451 (2008) 652–657.
[6] M.S. Whittingham, Chem. Rev. 104 (2004) 4271–4301.
[7] D. Linden, T.B. Reddy, Handbook of Batteries, 3rd ed., McGraw-Hill, 2002.
[8] G. Girishkumar, B. McCloskey, A.C. Luntz, S. Swanson, W. Wilcke, J. Phys. Chem. Lett. 1 (2010) 2193–2203.
[9] S.W. Lee, N. Yabuuchi, B.M. Gallant, S. Chen, B.S. Kim, P.T. Hammond, Y. Shao-Horn, Nat. Nanotechnol. 5 (2010) 531–537.
[10] Y.C. Lu, H.A. Gasteiger, M.C. Parent, V. Chiloyan, Y. Shao-Horn, Electrochem. Solid State Lett. 13 (2010) A69–A72.
[11] A. Debart, A.J. Paterson, J. Bao, P.G. Bruce, Angew. Chem. Int. Edit. 47 (2008) 4521–4524.
[12] A.S. Arico, P. Bruce, B. Scrosati, J.M. Tarascon, W. Van Schalkwijk, Nat. Mater. 4 (2005) 366–377.
[13] Basic Research Needs for Electrical Energy Storage Office of Basic Energy Sciences, U.S. Department of Energy, Washington, DC, 2007.
[14] S.Y. Chung, J.T. Bloking, Y.M. Chiang, Nat. Mater. 1 (2002) 123–128.
[15] C.K. Chan, H.L. Peng, G. Liu, K. McIlwrath, X.F. Zhang, R.A. Huggins, Y. Cui, Nat. Nanotechnol. 3 (2008) 31–35.
[16] H.W. Lee, P. Muralidharan, R. Ruffo, C.M. Mari, Y. Cui, D.K. Kim, Nano Lett. 10 (2010) 3852–3856.
[17] X.L. Ji, L.F. Nazar, J. Mater. Chem. 20 (2010) 9821–9826.

[18] Y.C. Lu, Z.C. Xu, H.A. Gasteiger, S. Chen, K. Hamad-Schifferli, Y. Shao-Horn, J. Am. Chem. Soc. 132 (2010) 12170–12171.
[19] J. Baxter, Z.X. Bian, G. Chen, D. Danielson, M.S. Dresselhaus, A.G. Fedorov, T.S. Fisher, C.W. Jones, E. Maginn, U. Kortshagen, A. Manthiram, A. Nozik, D.R. Rolison, T. Sands, L. Shi, D. Sholl, Y.Y. Wu, Energy Environ. Sci. 2 (2009) 559–588.
[20] M. Fernandez-Garcia, A. Martinez-Arias, J.C. Hanson, J.A. Rodriguez, Chem. Rev. 104 (2004) 4063–4104.
[21] N. Millot, D. Aymes, F. Bernard, J.C. Niepce, A. Traverse, F. Bouree, B.L. Cheng, P. Perriat, J. Phys. Chem. B 107 (2003) 5740–5750.
[22] H.Z. Zhang, J.F. Banfield, J. Mater. Chem. 8 (1998) 2073–2076.
[23] J.M. McHale, A. Auroux, A.J. Perrotta, A. Navrotsky, Science 277 (1997) 788–791.
[24] P. Ayyub, M. Multani, M. Barma, V.R. Palkar, R. Vijayaraghavan, J. Phys. C: Solid State Phys. 21 (1988) 2229–2245.
[25] M.D. Hernandez-Alonso, A.B. Hungria, A. Martinez-Arias, J.M. Coronado, J.C. Conesa, J. Soria, M. Fernandez-Garcia, Phys. Chem. Chem. Phys. 6 (2004) 3524–3529.
[26] H. Gleiter, Prog. Mater. Sci. 33 (1989) 223–315.
[27] K.S. Kumar, H. Van Swygenhoven, S. Suresh, Acta Mater. 51 (2003) 5743–5774.
[28] M.A. Meyers, A. Mishra, D.J. Benson, Prog. Mater. Sci. 51 (2006) 427–556.
[29] G. He, J. Eckert, W. Loser, L. Schultz, Nat. Mater. 2 (2003) 33–37.
[30] J. Schiotz, F.D. Di Tolla, K.W. Jacobsen, Nature 391 (1998) 561–563.
[31] K.S. Kumar, S. Suresh, M.F. Chisholm, J.A. Horton, P. Wang, Acta Mater. 51 (2003) 387–405.
[32] M.W. Chen, E. Ma, K.J. Hemker, H.W. Sheng, Y.M. Wang, X.M. Cheng, Science 300 (2003) 1275–1277.
[33] Z. Budrovic, H. Van Swygenhoven, P.M. Derlet, S. Van Petegem, B. Schmitt, Science 304 (2004) 273–276.
[34] Y. Champion, C. Langlois, S. Guerin-Mailly, P. Langlois, J.L. Bonnentien, M.J. Hytch, Science 300 (2003) 310–311.
[35] C.E. Hamm, R. Merkel, O. Springer, P. Jurkojc, C. Maier, K. Prechtel, V. Smetacek, Nature 421 (2003) 841–843.
[36] A.P. Garcia, M.J. Buehler, Comput. Mater. Sci. 48 (2010) 303–309.
[37] C.E. Hamm, J. Nanosci. Nanotechnol. 5 (2005) 108–119.
[38] X.L. Ji, K.T. Lee, L.F. Nazar, Nat. Mater. 8 (2009) 500–506.
[39] J. Maier, Nat. Mater. 4 (2005) 805–815.
[40] H. Kim, B. Han, J. Choo, J. Cho, Angew. Chem. Int. Edit. 47 (2008) 10151–10154.
[41] A.D. Robertson, A.R. Armstrong, P.G. Bruce, Chem. Mater. 13 (2001) 2380–2386.
[42] Y.G. Guo, J.S. Hu, L.J. Wan, Adv. Mater. 20 (2008) 4384–14384.
[43] Y.S. Hu, L. Kienle, Y.G. Guo, J. Maier, Adv. Mater. 18 (2006) 1421–1426.
[44] J. Jamnik, J. Maier, Phys. Chem. Chem. Phys. 5 (2003) 5215–5220.
[45] P. Balaya, Energy Environ. Sci. 1 (2008) 645–654.
[46] Q. Wang, H. Li, L.Q. Chen, X.J. Huang, Carbon 39 (2001) 2211–2214.
[47] N.A. Kaskhedikar, J. Maier, Adv. Mater. 21 (2009) 2664–2680.
[48] G.G. Amatucci, N. Pereira, J. Fluorine Chem. 128 (2007) 243–262.
[49] P. Balaya, A.J. Bhattacharyya, J. Jamnik, Y.F. Zhukovskii, E.A. Kotomin, J. Maier, J. Power Sources 159 (2006) 171–178.
[50] O. Delmer, P. Balaya, L. Kienle, J. Maier, Adv. Mater. 20 (2008) 501–505.
[51] R. Borup, J. Meyers, B. Pivovar, Y.S. Kim, R. Mukundan, N. Garland, D. Myers, M. Wilson, F. Garzon, D. Wood, P. Zelenay, K. More, K. Stroh, T. Zawodzinski, J. Boncella, J.E. McGrath, M. Inaba, K. Miyatake, M. Hori, K. Ota, Z. Ogumi, S. Miyata, A. Nishikata, Z. Siroma, Y. Uchimoto, K. Yasuda, K.-i. Kimijima, N. Iwashita, Chem. Rev. 107 (2007) 3904–3951.
[52] N. Kroger, K.H. Sandhage, MRS Bull. 35 (2010) 122–126.
[53] C. Sanchez, H. Arribart, M.M.G. Guille, Nat. Mater. 4 (2005) 277–288.
[54] M. Sarikaya, C. Tamerler, A.K.Y. Jen, K. Schulten, F. Baneyx, Nat. Mater. 2 (2003) 577–585.
[55] K.H. Sandhage, M.B. Dickerson, P.M. Huseman, M.A. Caranna, J.D. Clifton, T.A. Bull, T.J. Heibel, W.R. Overton, M.E.A. Schoenwaelder, Adv. Mater. 14 (2002) 429–433.
[56] Z.H. Bao, M.R. Weatherspoon, S. Shian, Y. Cai, P.D. Graham, S.M. Allan, G. Ahmad, M.B. Dickerson, B.C. Church, Z.T. Kang, H.W. Abernathy, C.J. Summers, M.L. Liu, K.H. Sandhage, Nature 446 (2007) 172–175.
[57] M.R. Weatherspoon, M.B. Dickerson, G. Wang, Y. Cai, S. Shian, S.C. Jones, S.R. Marder, K.H. Sandhage, Angew. Chem. Int. Edit. 46 (2007) 5724–5727.
[58] G. Pistoia, Lithium Batteries, Elsevier, New York, 1994.
[59] J. Yamaura, Y. Ozaki, A. Morita, A. Ohta, J. Power Sources 43 (1993) 233–239.
[60] J.L. Tirado, Mater. Sci. Eng.: R: Rep. 40 (2003) 103–136.
[61] Y. Idota, T. Kubota, A. Matsufuji, Y. Maekawa, T. Miyasaka, Science 276 (1997) 1395–1397.
[62] M. Winter, J.O. Besenhard, Electrochim. Acta 45 (1999) 31–50.
[63] H.C. Shin, M.L. Liu, Adv. Funct. Mater. 15 (2005) 582–586.
[64] C.S. Johnson, J.T. Vaughey, M.M. Thackeray, T. Sarakonsri, S.A. Hackney, L. Fransson, K. Edstrom, J.O. Thomas, Electrochem. Commun. 2 (2000) 595–600.
[65] L.M.L. Fransson, J.T. Vaughey, R. Benedek, K. Edstrom, J.O. Thomas, M.M. Thackeray, Electrochem. Commun. 3 (2001) 317–323.
[66] P. Poizot, S. Laruelle, S. Grugeon, L. Dupont, J.M. Tarascon, Nature 407 (2000) 496–499.
[67] F. Leroux, G.R. Goward, W.P. Power, L.F. Nazar, Electrochem. Solid State Lett. 1 (1998) 255–258.
[68] R. Malini, U. Uma, T. Sheela, M. Ganesan, N.G. Renganathan, Ionics 15 (2009) 301–307.
[69] S. Sodergren, H. Siegbahn, H. Rensmo, H. Lindstrom, A. Hagfeldt, S.E. Lindquist, J. Phys. Chem. B 101 (1997) 3087–3090.
[70] D.W. Murphy, R.J. Cava, S.M. Zahurak, A. Santoro, Solid State Ionics 9–10 (1983) 413–417.
[71] T. Ohzuku, A. Ueda, N. Yamamoto, J. Electrochem. Soc. 142 (1995) 1431–1435.
[72] K. Amine, I. Belharouak, Z.H. Chen, T. Tran, H. Yumoto, N. Ota, S.T. Myung, Y.K. Sun, Adv. Mater. 22 (2010) 3052–3057.
[73] J.H. Ryu, J.W. Kim, Y.E. Sung, S.M. Oh, Electrochem. Solid State Lett. 7 (2004) A306–A309.
[74] M.H. Park, M.G. Kim, J. Joo, K. Kim, J. Kim, S. Ahn, Y. Cui, J. Cho, Nano Lett. 9 (2009) 3844–3847.
[75] L.F. Cui, L.B. Hu, J.W. Choi, Y. Cui, ACS Nano 4 (2010) 3671–3678.
[76] Y.G. Li, B. Tan, Y.Y. Wu, Nano Lett. 8 (2008) 265–270.
[77] K.M. Shaju, F. Jiao, A. Debart, P.G. Bruce, Phys. Chem. Chem. Phys. 9 (2007) 1837–1842.
[78] S. Grugeon, S. Laruelle, R. Herrera-Urbina, L. Dupont, P. Poizot, J.M. Tarascon, J. Electrochem. Soc. 148 (2001) A285–A292.
[79] J.C. Park, J. Kim, H. Kwon, H. Song, Adv. Mater. 21 (2009) 803–807.
[80] H. Mukaibo, A. Yoshizawa, T. Momma, T. Osaka, J. Power Sources 119–121 (2003) 60–63.
[81] J.W. Seo, J.T. Jang, S.W. Park, C.J. Kim, B.W. Park, J.W. Cheon, Adv. Mater. 20 (2008) 4269–4273.
[82] S.A. Liu, X.M. Yin, L.B. Chen, Q.H. Li, T.H. Wang, Solid State Sci. 12 (2010) 712–718.
[83] J. Cho, J. Mater. Chem. 20 (2010) 4009–4014.
[84] S. Lee, J. Cho, Chem. Commun. 46 (2010) 2444–2446.
[85] W.J. Lee, M.H. Park, Y. Wang, J.Y. Lee, J. Cho, Chem. Commun. 46 (2010) 622–624.
[86] G.W. Zhou, H. Li, H.P. Sun, D.P. Yu, Y.Q. Wang, X.J. Huang, L.Q. Chen, Z. Zhang, Appl. Phys. Lett. 75 (1999) 2447–2449.
[87] H. Li, X.J. Huang, L.Q. Chen, Electrochem. Solid State Lett. 1 (1998) 241–243.
[88] U. Kasavajjula, C. Wang, A.J. Appleby, J. Power Sources 163 (2007) 1003–1039.
[89] M.G. Kim, J. Cho, Adv. Funct. Mater. 19 (2009) 1497–1514.
[90] C.K. Chan, X.F. Zhang, Y. Cui, Nano Lett. 8 (2008) 307–309.
[91] H. Liu, G. Wang, J. Park, J. Wang, H. Liu, C. Zhang, Electrochim. Acta 54 (2009) 1733–1736.
[92] Y. Yu, C.H. Chen, Y. Shi, Adv. Mater. 19 (2007) 993–997.
[93] H.L. Zhang, Y. Zhang, X.G. Zhang, F. Li, C. Liu, J. Tan, H.M. Cheng, Carbon 44 (2006) 2778–2784.
[94] H. Uchlyama, E. Hosono, I. Honma, H. Zhou, H. Imai, Electrochem. Commun. 10 (2008) 52–55.
[95] X.L. Gou, J. Chen, P.W. Shen, Mater. Chem. Phys. 93 (2005) 557–566.
[96] C. Wang, Y. Zhou, M.Y. Ge, X.B. Xu, Z.L. Zhang, J.Z. Jiang, J. Am. Chem. Soc. 132 (2010) 46–47.
[97] Y.S. Hu, P. Adelhelm, B.M. Smarsly, J. Maier, ChemSusChem 3 (2010) 231–235.
[98] C.K. Chan, R.N. Patel, M.J. O'Connell, B.A. Korgel, Y. Cui, ACS Nano 4 (2010) 1443–1450.
[99] S.H. Ng, J.Z. Wang, D. Wexler, K. Konstantinov, Z.P. Guo, H.K. Liu, Angew. Chem. Int. Edit. 45 (2006) 6896–6899.
[100] B.K. Guo, J. Shu, K. Tang, Y. Bai, Z.X. Wang, L.Q. Chen, J. Power Sources 177 (2008) 205–210.
[101] G. Derrien, J. Hassoun, S. Panero, B. Scrosati, Adv. Mater. 19 (2007) 2336–2340.
[102] J.R. Dahn, T. Zheng, Y.H. Liu, J.S. Xue, Science 270 (1995) 590–593.
[103] V.A. Nalimova, D.E. Sklovsky, G.N. Bondarenko, H. AlvergnatGaucher, S. Bonnamy, F. Beguin, Synth. Met. 88 (1997) 89–93.
[104] T.P. Kumar, R. Ramesh, Y.Y. Lin, G.T.K. Fey, Electrochem. Commun. 6 (2004) 520–525.
[105] G.F. Ortiz, I. Hanzu, P. Lavela, P. Knauth, J.L. Tirado, T. Djenizian, Chem. Mater. 22 (2010) 1926–1932.
[106] Y. Wang, F.B. Su, J.Y. Lee, X.S. Zhao, Chem. Mater. 18 (2006) 1347–1353.
[107] G.M. An, N. Na, X.R. Zhang, Z.J. Miao, S.D. Miao, K.L. Ding, Z.M. Liu, Nanotechnology 18 (2007).
[108] X.W. Lou, D. Deng, J.Y. Lee, L.A. Archer, Chem. Mater. 20 (2008) 6562–6566.
[109] N. Du, H. Zhang, B.D. Chen, X.Y. Ma, X.H. Huang, J.P. Tu, D.R. Yang, Mater. Res. Bull. 44 (2009) 211–215.
[110] J. Fan, T. Wang, C.Z. Yu, B. Tu, Z.Y. Jiang, D.Y. Zhao, Adv. Mater. 16 (2004) 1432–1436.
[111] D.H. Wang, D.W. Choi, J. Li, Z.G. Yang, Z.M. Nie, R. Kou, D.H. Hu, C.M. Wang, L.V. Saraf, J.G. Zhang, I.A. Aksay, J. Liu, ACS Nano 3 (2009) 907–914.
[112] D.W. Kim, Y.D. Ko, J.G. Park, B.K. Kim, Angew. Chem. Int. Edit. 46 (2007) 6654–6657.
[113] S. Sakamoto, M. Yoshinaka, K. Hirota, O. Yamaguchi, J. Am. Ceram. Soc. 80 (1997) 267–268.
[114] Q.M. Pan, H.B. Wang, Y.H. Jiang, Electrochem. Commun. 9 (2007) 754–760.
[115] S.N. Yang, Q.M. Pan, J. Liu, Electrochem. Commun. 12 (2010) 479–482.
[116] J.K. Lee, M.C. Kung, L. Trahey, M.N. Missaghi, H.H. Kung, Chem. Mater. 21 (2009) 6–8.
[117] L.F. Cui, R. Ruffo, C.K. Chan, H.L. Peng, Y. Cui, Nano Lett. 9 (2009) 491–495.
[118] Y.S. Hu, R. Demir-Cakan, M.M. Titirici, J.O. Muller, R. Schlogl, M. Antonietti, J. Maier, Angew. Chem. Int. Edit. 47 (2008) 1645–1649.
[119] P. Meduri, C. Pendyala, V. Kumar, G.U. Sumanasekera, M.K. Sunkara, Nano Lett. 9 (2009) 612–616.
[120] Y. Wang, H.C. Zeng, J.Y. Lee, Adv. Mater. 18 (2006) 645–649.
[121] D. Deng, J.Y. Lee, Chem. Mater. 20 (2008) 1841–1846.
[122] K.S. Park, A. Benayad, D.J. Kang, S.G. Doo, J. Am. Chem. Soc. 130 (2008) 14930–14931.
[123] J. Jamnik, R. Dominko, B. Erjavec, M. Remskar, A. Pintar, M. Gaberscek, Adv. Mater. 21 (2009) 2715–2719.
[124] Y.G. Guo, Y.S. Hu, W. Sigle, J. Maier, Adv. Mater. 19 (2007) 2087–2091.
[125] M. Green, E. Fielder, B. Scrosati, M. Wachtler, J.S. Moreno, Electrochem. Solid State Lett. 6 (2003) A75–A79.
[126] L. Taberna, S. Mitra, P. Poizot, P. Simon, J.M. Tarascon, Nat. Mater. 5 (2006) 567–573.

[127] J. Hassoun, S. Panero, P. Simon, P.L. Taberna, B. Scrosati, Adv. Mater. 19 (2007) 1632–1635.
[128] S. Grugeon, S. Laruelle, L. Dupont, F. Chevallier, P.L. Taberna, P. Simon, L. Gireaud, S. Lascaud, E. Vidal, B. Yrieix, J.M. Tarascon, Chem. Mater. 17 (2005) 5041–5047.
[129] F.R. Gamble, A.H. Thompson, Solid State Commun. 27 (1978) 379–382.
[130] B.M.L. Rao, R.W. Francis, H.A. Christopher, J. Electrochem. Soc. 124 (1977) 1490–1492.
[131] K. Mizushima, P.C. Jones, P.J. Wiseman, J.B. Goodenough, Mater. Res. Bull. 15 (1980) 783–789.
[132] M.M. Thackeray, Prog. Solid State Chem. 25 (1997) 1–71.
[133] M. Yonemura, A. Yamada, H. Kobayashi, M. Tabuchi, T. Kamiyama, Y. Kawamoto, R. Kanno, J. Mater. Chem. 14 (2004) 1948–1958.
[134] J. Cho, J. Mater. Chem. 18 (2008) 2257–2261.
[135] J. Cho, M.M. Thackeray, J. Electrochem. Soc. 146 (1999) 3577–3581.
[136] K.S. Nanjundaswamy, A.K. Padhi, J.B. Goodenough, S. Okada, H. Ohtsuka, H. Arai, J. Yamaki, Solid State Ionics 92 (1996) 1–10.
[137] A.K. Padhi, K.S. Nanjundaswamy, C. Masquelier, S. Okada, J.B. Goodenough, J. Electrochem. Soc. 144 (1997) 1609–1613.
[138] J.L. Pizarrosanz, J.M. Dance, G. Villeneuve, M.I. Arriortuamarcaida, Mater. Lett. 18 (1994) 327–330.
[139] L.A. Groat, M. Raudsepp, F.C. Hawthorne, T.S. Ercit, B.L. Sherriff, J.S. Hartman, Am. Mineral. 75 (1990) 992–1008.
[140] J. Barker, M.Y. Saidi, J.L. Swoyer, J. Electrochem. Soc. 150 (2003) A1394–A1398.
[141] J. Barker, R.K.B. Gover, P. Burns, A. Bryan, M.Y. Saidi, J.L. Swoyer, J. Power Sources 146 (2005) 516–520.
[142] H.L. Chen, C.P. Grey, Adv. Mater. 20 (2008) 2206–2210.
[143] X.X. Li, F.Y. Cheng, B. Guo, J. Chen, J. Phys. Chem. B 109 (2005) 14017–14024.
[144] F. Jiao, K.M. Shaju, P.G. Bruce, Angew. Chem. Int. Edit. 44 (2005) 6550–6553.
[145] E. Hosono, T. Kudo, I. Honma, H. Matsuda, H.S. Zhou, Nano Lett. 9 (2009) 1045–1051.
[146] D.K. Kim, P. Muralidharan, H.W. Lee, R. Ruffo, Y. Yang, C.K. Chan, H. Peng, R.A. Huggins, Y. Cui, Nano Lett. 8 (2008) 3948–3952.
[147] F. Jiao, J.L. Bao, A.H. Hill, P.G. Bruce, Angew. Chem. Int. Edit. 47 (2008) 9711–9716.
[148] C.Z. Wu, Y. Xie, L.Y. Lei, S.Q. Hu, C.Z. OuYang, Adv. Mater. 18 (2006) 1727–1732.
[149] B. Jin, E.M. Jin, K.H. Park, H.B. Gu, Electrochem. Commun. 10 (2008) 1537–1540.
[150] Y.G. Wang, Y.R. Wang, E.J. Hosono, K.X. Wang, H.S. Zhou, Angew. Chem. Int. Edit. 47 (2008) 7461–7465.
[151] H.M. Xie, R.S. Wang, J.R. Ying, L.Y. Zhang, A.F. Jalbout, H.Y. Yu, G.L. Yang, X.M. Pan, Z.M. Su, Adv. Mater. 18 (2006) 2609–2613.
[152] A.V. Murugan, T. Muraliganth, A. Manthiram, Electrochem. Commun. 10 (2008) 903–906.
[153] C.H. Jiang, S.X. Dou, H.K. Liu, M. Ichihara, H.S. Zhou, J. Power Sources 172 (2007) 410–415.
[154] F. Jiao, P.G. Bruce, Adv. Mater. 19 (2007) 657–660.
[155] B.L. Ellis, K.T. Lee, L.F. Nazar, Chem. Mater. 22 (2010) 691–714.
[156] A. Manthiram, A.V. Murugan, A. Sarkar, T. Muraliganth, Energy Environ. Sci. 1 (2008) 621–638.
[157] A.M. Cao, J.S. Hu, H.P. Liang, L.J. Wan, Angew. Chem. Int. Edit. 44 (2005) 4391–4395.
[158] D. Sun, C.W. Kwon, G. Baure, E. Richman, J. MacLean, B. Dunn, S.H. Tolbert, Adv. Funct. Mater. 14 (2004) 1197–1204.
[159] J.S. Sakamoto, B. Dunn, J. Electrochem. Soc. 149 (2002) A26–A30.
[160] A. Kuwahara, S. Suzuki, M. Miyayama, Solid State Ionics 179 (2008) 1890–1896.
[161] K. Takahashi, Y. Wang, G.Z. Cao, J. Phys. Chem. B 109 (2005) 48–51.
[162] Y. Wang, K. Lee, H. Shang, B. Wiley, Y.N. Xia, G.Z. Cao, Phys. Status Solidi A: Appl. Mater. Sci. 202 (2005) R79–R81.
[163] P. Ghosh, S. Mahanty, R.N. Basu, Mater. Chem. Phys. 110 (2008) 406–410.
[164] R. Guo, P.F. Shi, X.Q. Cheng, Y.L. Ma, Z. Tan, J. Power Sources 189 (2009) 2–8.
[165] W.J. Zhou, B.L. He, H.L. Li, Mater. Res. Bull. 43 (2008) 2285–2294.
[166] M. Ferreira, V. Zucolotto, F. Huguenin, R.M. Torresi, O.N. Oliveira, J. Nanosci. Nanotechnol. 2 (2002) 29–32.
[167] F. Huguenin, D.S. dos Santos, A. Bassi, F.C. Nart, O.N. Oliveira, Adv. Funct. Mater. 14 (2004) 985–991.
[168] E.A. Ponzio, T.M. Benedetti, R.M. Torresi, Electrochim. Acta 52 (2007) 4419–4427.
[169] H. Huang, S.C. Yin, T. Kerr, N. Taylor, L.F. Nazar, Adv. Mater. 14 (2002) 1525–1528.
[170] T. Nakamura, Y. Miwa, M. Tabuchi, Y. Yamada, J. Electrochem. Soc. 153 (2006) A1108–A1114.
[171] H. Nakano, K. Dokko, S. Koizumi, H. Tannai, K. Kanamura, J. Electrochem. Soc. 155 (2008) A909–A914.
[172] J.K. Kim, G. Cheruvally, J.H. Ahn, G.C. Hwang, J.B. Choi, J. Phys. Chem. Solids 69 (2008) 2371–2377.
[173] M. Konarova, I. Taniguchi, Powder Technol. 191 (2009) 111–116.
[174] Q. Cao, H.P. Zhang, G.J. Wang, Q. Xia, Y.P. Wu, H.Q. Wu, Electrochem. Commun. 9 (2007) 1228–1232.
[175] J. Kim, M. Noh, J. Cho, H. Kim, K.B. Kim, J. Electrochem. Soc. 152 (2005) A1142–A1148.
[176] Y.J. Kim, J.P. Cho, T.J. Kim, B. Park, J. Electrochem. Soc. 150 (2003) A1723–A1725.
[177] L.J. Liu, Z.X. Wang, H. Li, L.Q. Chen, X.J. Huang, Solid State Ionics 152 (2002) 341–346.
[178] J. Cho, C.S. Kim, S.I. Yoo, Electrochem. Solid State Lett. 3 (2000) 362–365.
[179] Z.X. Wang, X.J. Huang, L.Q. Chen, J. Electrochem. Soc. 150 (2003) A199–A208.
[180] T. Fang, J.G. Duh, S.R. Sheen, J. Electrochem. Soc. 152 (2005) A1701–A1706.
[181] C.Z. Lu, J.M. Chen, Y.D. Cho, W.H. Hsu, P. Muralidharan, G.T.K. Fey, J. Power Sources 184 (2008) 392–401.
[182] Y.K. Sun, K.J. Hong, J. Prakash, J. Electrochem. Soc. 150 (2003) A970–A972.
[183] J.M. Han, S.T. Myung, Y.K. Sun, J. Electrochem. Soc. 153 (2006) A1290–A1295.
[184] S. Takai, M. Kamata, S. Fujine, K. Yoneda, K. Kanda, T. Esaka, Solid State Ionics 123 (1999) 165–172.
[185] D.Q. Liu, X.Q. Liu, Z.Z. He, Mater. Chem. Phys. 105 (2007) 362–366.
[186] Y.H. Rho, L.F. Nazar, L. Perry, D. Ryan, J. Electrochem. Soc. 154 (2007) A283–A289.
[187] Y.S. Hu, Y.G. Guo, R. Dominko, M. Gaberscek, J. Jamnik, J. Maier, Adv. Mater. 19 (2007) 1963–1966.
[188] A.L.M. Reddy, M.M. Shaijumon, S.R. Gowda, P.M. Ajayan, Nano Lett. 9 (2009) 1002–1006.
[189] J.-S. Lee, S. Tai Kim, R. Cao, N.-S. Choi, M. Liu, K.T. Lee, J. Cho, Adv. Energy Mater. 1 (2011) 34–50.
[190] I. Kowaluk, J. Read, M. Salomon, Pure Appl. Chem. 79 (2007) 851–860.
[191] J. Read, J. Electrochem. Soc. 149 (2002) A1190–A1195.
[192] S.S. Zhang, D. Foster, J. Read, J. Power Sources 195 (2010) 1235–1240.
[193] X.H. Yang, P. He, Y.Y. Xia, Electrochem. Commun. 11 (2009) 1127–1130.
[194] J. Read, K. Mutolo, M. Ervin, W. Behl, J. Wolfenstine, A. Driedger, D. Foster, J. Electrochem. Soc. 150 (2003) A1351–A1356.
[195] G.Q. Zhang, J.P. Zheng, R. Liang, C. Zhang, B. Wang, M. Hendrickson, E.J. Plichta, J. Electrochem. Soc. 157 (2010) A953–A956.
[196] M. Hayashi, H. Minowa, M. Takahashi, T. Shodai, Electrochemistry 78 (2010) 325–328.
[197] C. Tran, X.Q. Yang, D.Y. Qu, J. Power Sources 195 (2010) 2057–2063.
[198] M. Mirzaeian, P.J. Hall, Electrochim. Acta 54 (2009) 7444–7451.
[199] R.E. Williford, J.G. Zhang, J. Power Sources 194 (2009) 1164–1170.
[200] S.D. Beattie, D.M. Manolescu, S.L. Blair, J. Electrochem. Soc. 156 (2009) A44–A47.
[201] J.S. Hummelshoj, J. Blomqvist, S. Datta, T. Vegge, J. Rossmeisl, K.S. Thygesen, A.C. Luntz, K.W. Jacobsen, J.K. Norskov, J. Chem. Phys. 132 (2010).
[202] N. Seriani, Nanotechnology 20 (2009).
[203] K.M. Abraham, Z. Jiang, J. Electrochem. Soc. 143 (1996) 1–5.
[204] T. Ogasawara, A. Debart, M. Holzapfel, P. Novak, P.G. Bruce, J. Am. Chem. Soc. 128 (2006) 1390–1393.
[205] A. Debart, J. Bao, G. Armstrong, P.G. Bruce, J. Power Sources 174 (2007) 1177–1182.
[206] F. Mizuno, S. Nakanishi, Y. Kotani, S. Yokoishi, H. Iba, Electrochemistry 78 (2010) 403–405.
[207] H. Minowa, M. Hayashi, M. Takahashi, T. Shodai, Electrochemistry 78 (2010) 353–356.
[208] Y.C. Lu, H.A. Gasteiger, E. Crumlin, R. McGuire, Y. Shao-Horn, J. Electrochem. Soc. 157 (2010) A1016–A1025.
[209] V. Giordani, S.A. Freunberger, P.G. Bruce, J.M. Tarascon, D. Larcher, Electrochem. Solid State Lett. 13 (2010) A180–A183.
[210] L. Jin, L.P. Xu, C. Morein, C.H. Chen, M. Lai, S. Dharmarathna, A. Dobley, S.L. Suib, Adv. Funct. Mater. 20 (2010) 3373–3382.
[211] A.K. Thapa, K. Saimen, T. Ishihara, Electrochem. Solid State Lett. 13 (2010) A165–A167.
[212] A.K. Thapa, T. Ishihara, J. Power Sources 196 (2011) 7016–7020.
[213] F. Mizuno, https://www.ornl.gov/ccsd_registrations/battery/presentations/Session4-430-Mizuno.pdf from Symposium: Scalable Energy Storage Beyond Li-Ion – Materials perspectives, at Oak Ridge National Laboratory (accessed on January 6, 2011).
[214] V. Neburchilov, H. Wang, J.J. Martin, W. Qu, J. Power Sources 195 (2010) 1271–1291.
[215] W.R. Momyer, E.L. Littauer, in: Proceedings of 15th Intersociety Energy Conversion Engineering Conference, vol. 2, 1980, pp. 1480–1486.
[216] S.J. Visco, E. Nimon, B. Katz, L.D. Jonghe, M.Y. Chu, The International Meeting on Lithium Batteries, Nara, Japan, 2004.
[217] S.J. Visco, E. Nimon, B. Katz, L.D. Jonghe, M.Y. Chu, The 210th Electrochemical Society Meeting, Cancun, Mexico, 2006.
[218] T. Zhang, N. Imanishi, S. Hasegawa, A. Hirano, J. Xie, Y. Takeda, O. Yamamoto, N. Sammes, Electrochem. Solid State Lett. 12 (2009) A132–A135.
[219] S. Hasegawa, N. Imanishi, T. Zhang, J. Xie, A. Hirano, Y. Takeda, O. Yamamoto, J. Power Sources 189 (2009) 371–377.
[220] N. Imanishi, S. Hasegawa, T. Zhang, A. Hirano, Y. Takeda, O. Yamamoto, J. Power Sources 185 (2008) 1392–1397.
[221] T. Zhang, N. Imanishi, S. Hasegawa, A. Hirano, J. Xie, Y. Takeda, O. Yamamoto, N. Sammes, J. Electrochem. Soc. 155 (2008) A965–A969.
[222] E. Antolini, Appl. Catal. B: Environ. 88 (2009) 1–24.
[223] A.L. Dicks, J. Power Sources 156 (2006) 128–141.
[224] W.M. Zhang, P. Sherrell, A.I. Minett, J.M. Razal, J. Chen, Energy Environ. Sci. 3 (2010) 1286–1293.
[225] Y.Y. Shao, J. Liu, Y. Wang, Y.H. Lin, J. Mater. Chem. 19 (2009) 46–59.
[226] E. Antolini, E.R. Gonzalez, Solid State Ionics 180 (2009) 746–763.
[227] E. Antolini, E.R. Gonzalez, Appl. Catal. A: Gen. 365 (2009) 1–19.
[228] E. Antolini, Appl. Catal. B: Environ. 100 (2010) 413–426.
[229] S. Litster, G. McLean, J. Power Sources 130 (2004) 61–76.
[230] F. Bidault, D.J.L. Brett, P.H. Middleton, N.P. Brandon, J. Power Sources 187 (2009) 39–48.
[231] Y.G. Wang, H.S. Zhou, J. Power Sources 195 (2010) 358–361.
[232] P. He, Y. Wang, H. Zhou, Electrochem. Commun. 12 (2010) 1686–1689.
[233] H. Tang, J.H. Chen, Z.P. Huang, D.Z. Wang, Z.F. Ren, L.H. Nie, Y.F. Kuang, S.Z. Yao, Carbon 42 (2004) 191–197.
[234] K.P. Gong, F. Du, Z.H. Xia, M. Durstock, L.M. Dai, Science 323 (2009) 760–764.

[235] C. Wang, M. Waje, X. Wang, J.M. Tang, R.C. Haddon, Y.S. Yan, Nano Lett. 4 (2004) 345–348.
[236] W. Xiong, F. Du, Y. Liu, A. Perez, M. Supp, T.S. Ramakrishnan, L.M. Dai, L. Jiang, J. Am. Chem. Soc. 132 (2010) 15839–15841.
[237] B. Seger, P.V. Kamat, J. Phys. Chem. C 113 (2009) 7990–7995.
[238] R. Kou, Y.Y. Shao, D.H. Wang, M.H. Engelhard, J.H. Kwak, J. Wang, V.V. Viswanathan, C.M. Wang, Y.H. Lin, Y. Wang, I.A. Aksay, J. Liu, Electrochem. Commun. 11 (2009) 954–957.
[239] L.T. Qu, Y. Liu, J.B. Baek, L.M. Dai, ACS Nano 4 (2010) 1321–1326.
[240] R. Liu, D. Wu, X. Feng, K. Müllen, Angew. Chem. Int. Ed. 49 (2010) 2565–2569.
[241] A. Thomas, P. Kuhn, J. Weber, M.M. Titirici, M. Antonietti, Macromol. Rapid Commun. 30 (2009) 221–236.
[242] T. Zhang, N. Imanishi, Y. Shimonishi, A. Hirano, Y. Takeda, O. Yamamoto, N. Sammes, Chem. Commun. 46 (2010) 1661–1663.
[243] H.A. Gasteiger, S.S. Kocha, B. Sompalli, F.T. Wagner, Appl. Catal. B: Environ. 56 (2005) 9–35.
[244] B. Wang, J. Power Sources 152 (2005) 1–15.
[245] A. Ishihara, Y. Ohgi, K. Matsuzawa, S. Mitsushima, K. Ota, Electrochim. Acta 55 (2010) 8005–8012.
[246] C.W.B. Bezerra, L. Zhang, K.C. Lee, H.S. Liu, A.L.B. Marques, E.P. Marques, H.J. Wang, J.J. Zhang, Electrochim. Acta 53 (2008) 4937–4951.
[247] L. Zhang, J.J. Zhang, D.P. Wilkinson, H.J. Wang, J. Power Sources 156 (2006) 171–182.
[248] H.S. Zhou, Y.G. Wang, H.Q. Li, P. He, ChemSusChem 3 (2010) 1009–1019.
[249] Y.G. Wang, H.S. Zhou, Chem. Commun. 46 (2010) 6305–6307.
[250] F. Cheng, J. Shen, B. Peng, Y. Pan, Z. Tao, J. Chen, Nat. Chem. 3 (2011) 79–84.
[251] B. Winther-Jensen, O. Winther-Jensen, M. Forsyth, D.R. MacFarlane, Science 321 (2008) 671–674.
[252] B. Lim, M. Jiang, P.H.C. Camargo, E.C. Cho, J. Tao, X. Lu, Y. Zhu, Y. Xia, Science 324 (2009) 1302–1305.
[253] J. Zhang, K. Sasaki, E. Sutter, R.R. Adzic, Science 315 (2007) 220–222.
[254] F.T. Wagner, B. Lakshmanan, M.F. Mathias, J. Phys. Chem. Lett. 1 (2010) 2204–2219.
[255] G.G. Amatucci, J.M. Tarascon, L.C. Klein, J. Electrochem. Soc. 143 (1996).
[256] M. Morcrette, Y. Chabre, G. Vaughan, G. Amatucci, J.B. Leriche, S. Patoux, C. Masquelier, J.M. Tarascon, Electrochim. Acta 47 (2002) 3137–3149.
[257] J.R. Dahn, R.R. Haering, Solid State Commun. 40 (1981) 245–248.
[258] S. Denis, E. Baudrin, M. Touboul, J.M. Tarascon, J. Electrochem. Soc. 144 (1997) 4099–4109.
[259] R. van de Krol, A. Goossens, E.A. Meulenkamp, J. Electrochem. Soc. 146 (1999) 3150–3154.
[260] S. Mukerjee, T.R. Thurston, N.M. Jisrawi, X.Q. Yang, J. Mcbreen, M.L. Daroux, X.K. Xing, J. Electrochem. Soc. 145 (1998) 466–472.
[261] J. Rijssenbeek, Y. Gao, Z. Zhong, M. Croft, N. Jisrawi, A. Ignatov, T. Tsakalakos, J. Power Sources 196 (2011) 2332–2339.
[262] V.R. Stamenkovic, B.S. Mun, K.J.J. Mayrhofer, P.N. Ross, N.M. Markovic, J. Am. Chem. Soc. 128 (2006) 8813–8819.
[263] F.M. Alamgir, E. Strauss, M. denBoer, S. Greenbaum, J.F. Whitacre, C.-C. Kao, S. Neih, J. Electrochem. Soc. 152 (2005) A845–A849.
[264] A. Mansour, X.Q. Yang, X. Sun, J. McBreen, L. Croguennec, C. Delmas, J. Electrochem. Soc. 147 (2000) 2104–2109.
[265] I. Nakai, K. Takahashi, Y. Shiraishi, T. Nakagome, F. Nishikawa, J. Solid State Chem. 140 (1998) 145–148.
[266] W. Yoon, C.P. Grey, M. Balasubramanian, X.Q. Yang, J. McBreen, Chem. Mater. 15 (2003) 3161–3169.
[267] J.J. Rehr, R.C. Albers, Rev. Mod. Phys. 72 (2000) 621.
[268] B.L. Henke, E.M. Gullikson, J.C. Davis, Atom. Data Nucl. Data Tables 54 (1993) 181–342.
[269] C.F. Petersburg, R.C. Daniel, C. Jaye, D.A. Fischer, F.M. Alamgir, J. Synchrot. Radiat. 16 (2009) 610–615.
[270] N. Leifer, A. Colon, K. Martocci, F.M. Alamgir, T. Reddy, E. Takeuchi, S. Greenbaum, J. Electrochem. Soc. 154 (2007) A500–A506.
[271] T. Ressler, Environ. Sci. Technol. 34 (2000).
[272] H.S. Park, S.R. Kwon, Y.M. Jung, H.S. Kim, H.J. Lee, W.H. Hong, Chem. Commun. 42 (2009) 6388–6390.
[273] W. Yoon, K. Chung, J. McBreen, K. Zaghib, X. Yang, Electrochem. Solid-State Lett. 9 (2006) A415.
[274] Y. Dai, Y. Wang, V. Eshkenazi, E. Peled, S.G. Greenbaum, J. Electrochem. Soc. 145 (1998) 1179–1183.
[275] N.D. Leifer, V.S. Johnson, R. Ben-Ari, H. Gan, J.M. Lehnes, R. Guo, W. Lu, B.C. Muffoletto, T. Reddy, P.E. Stallworth, S.G. Greenbaum, J. Electrochem. Soc. 157 (2010) A148–A154.
[276] F. Ronci, P.E. Stallworth, F. Alamgir, T. Schiros, J. Van Sluytman, G. Xiaodong, P. Reale, S. Greenbaum, M. denBoer, B. Scrosati, J. Power Sources 119–121 (2003) 631–636.
[277] P.E Stallworth, F.S. Johnson, S.G. Greenbaum, S. Passerini, J. Flowers, W. Smyrl, J. Appl. Phys. 92 (2002) 3839–3852.
[278] Y. Wang, J. Sakamoto, S. Kostov, A.N. Mansour, M.L. denBoer, S.G. Greenbaum, C.-K. Huang, S. Surampudi, J. Power Sources 89 (2000) 232–236.
[279] Y. Wang, V. Yufit, X. Guo, E. Peled, S. Greenbaum, J. Power Sources 94 (2001) 230–237.
[280] R.E. Gerald Ii, C.S. Johnson, J.W. Rathke, R.J. Klingler, G. SandI, L.G. Scanlon, J. Power Sources 89 (2000) 237–243.
[281] R. Bhattacharyya, B. Key, H. Chen, A.S. Best, A.F. Hollenkamp, C.P. Grey, Nat. Mater. 9 (2010) 504–510.
[282] F.e.a. Chevallier, Electrochem. Solid State Lett. 6 (2003) A225–A228.
[283] B.e.a. Key, J. Am. Chem. Soc. 131 (2009) 9239–9249.
[284] M. Letellier, F. Chevallier, C. Clinard, E. Frackowiak, J.N. Rouzaud, F. Beguin, M. Morcrette, J.M. Tarascon, J. Chem. Phys. 118 (2003) 6038.
[285] M. Letellier, F. Chevallier, M. Morcrette, Carbon 45 (2007) 1025–1034.
[286] M.A. Banares, in: B.M. Weckhuysen (Ed.), In Situ Spectroscopy of Catalysts, American Scientific Publishers, USA, 2004, p. 332.
[287] G. Mestl, J. Mol. Catal. A: Chem. 158 (2000) 45–65.
[288] Y.M. Choi, H. Abernathy, H.-T. Chen, M.C. Lin, M. Liu, ChemPhysChem 7 (2006) 1957–1963.
[289] V.V. Pushkarev, V.I. Kovalchuk, J.L. d'Itri, J. Phys. Chem. B 108 (2004) 5341–5348.
[290] Z. Cheng, M. Liu, Solid State Ionics 178 (2007) 925–935.
[291] M.B. Pomfret, J.C. Owrutsky, R.A. Walker, Anal. Chem. 79 (2007) 2367–2372.
[292] H.Z. Yang, Y.Q. Yang, S.Z. Zou, J. Phys. Chem. B 110 (2006) 17296–17301.
[293] R. Baddour-Hadjean, J.-P. Pereira-Ramos, Chem. Rev. 110 (2010) 1278–1319.
[294] P. Lespade, A. Marchand, M. Couzi, F. Cruege, Carbon 22 (1984) 375.
[295] D.S. Knight, W.B. White, J. Mater. Res. 4 (1989) 385.
[296] W. Huang, R. Frech, J. Electrochem. Soc. 145 (1998) 765–770.
[297] T. Itoh, H. Sato, T. Nishina, T. Matue, I. Uchida, J. Power Sources 68 (1997) 333–337.
[298] C. Julien, Solid State Ionics 136–137 (2000) 887.
[299] W. Huang, R. Frech, Solid State Ionics 86–88 (1996) 395.
[300] W. Huang, R. Frech, J. Power Sources 81–82 (1999) 616–620.
[301] R. Baddour-Hadjean, C. Navone, J.P. Pereira-Ramos, Electrochim. Acta 54 (2009) 6674.
[302] R. Baddour-Hadjean, V. Golabkan, J.P. Pereira-Ramos, A. Mantoux, D. Lincot, J. Raman Spectrosc. 33 (2002) 631–638.
[303] E.M. Cazzanelli, S. Passerini, F. Decker, Solid State Ionics 70–71 (1994) 412.
[304] C. Julien, I. Ivanov, A. Gorenstein, Mater. Sci. Eng. B33 (1995) 168.
[305] J.M. McGraw, J.D. Perkins, J.G. Zhang, P. Liu, P.A. Parilla, J. Turner, D.L. Schulz, C.J. Curtis, D.S. Ginley, Solid State Ionics 113–115 (1998) 407.
[306] C.V. Ramana, R.J. Smith, O.M. Hussain, M. Massot, C.M. Julien, Surf. Interface Anal. 37 (2005) 406.
[307] L. Aldon, P. Kubiak, M. Womes, J.C. Jumas, J. Olivier-Fourcade, J.L. Tirado, J.I. Corredor, C. Perez Vicente, Chem. Mater. 16 (2004) 5721–5725.
[308] C.M. Julien, M. Massot, K. Zaghib, J. Power Sources 136 (2004) 72.
[309] I.A. Leonidov, O.N. Leonidova, L.A. Perelyaeva, R.F. Samigullina, S.A. Kovyazina, M.V. Patrakeev, Phys. Solid State 45 (2003) 2183.
[310] D.Z. Liu, W. Hayes, M. Kurmoo, M. Dalton, C. Chen, Physica C 235 (1994) 1203.
[311] B. O'Regan, M. Gratzel, Nature 353 (1991) 737.
[312] E.V. Proskuryakova, O.I. Kondratov, N.V. Porotnikov, K.I. Petrov, Zh. Neorg. Khim. 28 (1983) 1402.
[313] Z. Cheng, J.H. Wang, Y.M. Choi, L. Yang, M.C. Lin, M. Liu, Energy Environ. Sci., doi:10.1039/C1EE01758F.